Delft University of Technology

Freestanding Complex Oxide Membranes

Blah, P.J.

DOI
10.4233/uuid:1ae6a8e4-152a-420f-ba5d-672678fef469

Publication date
2025

Document Version
Final published version

Citation (APA)
Blah, P. J. (2025). *Freestanding Complex Oxide Membranes*. [Dissertation (TU Delft), Delft University of Technology]. https://doi.org/10.4233/uuid:1ae6a8e4-152a-420f-ba5d-672678fef469

Freestanding Complex Oxide Membranes

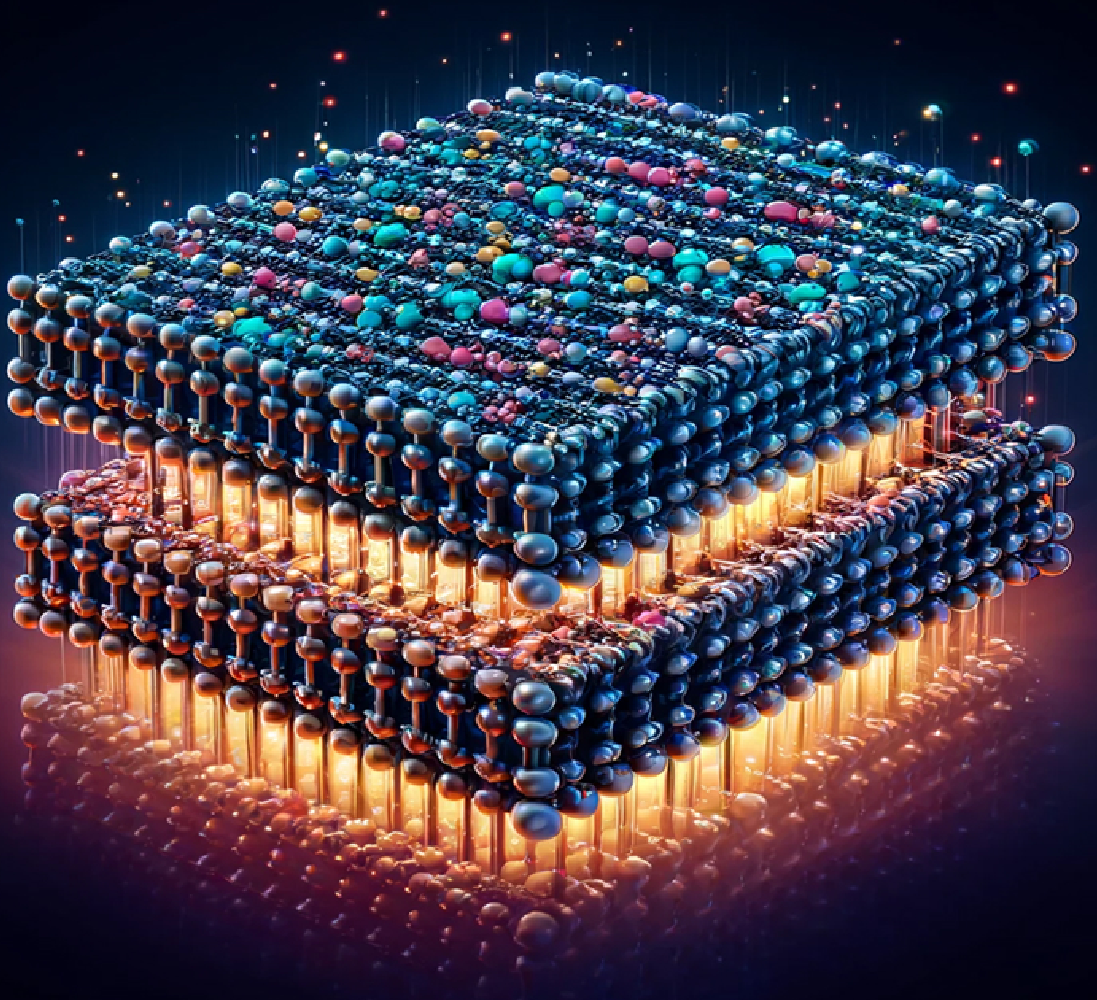

Patrick Blah

FREESTANDING COMPLEX OXIDE MEMBRANES

FREESTANDING COMPLEX OXIDE MEMBRANES

Dissertation

for the purpose of obtaining the degree of doctor
at Delft University of Technology
by the authority of the Rector Magnificus Prof.dr.ir. T.H.J.J. van der Hagen,
Chair of the Board for Doctorates,
to be defended publicly on October 1st, 2025

by

Patrick Jarlath BLAH

Master of Science in Physics,
University of Groningen, Groningen, The Netherlands,
born in Teddington, United Kingdom.

This dissertation has been approved by

Promotor: Prof. Dr. A. D. Caviglia
Copromotor: Prof. Dr. Y. M. Blanter

Composition of the doctoral committee:

Rector Magnificus,	Chairperson
Prof. Dr. A. D. Caviglia,	TU Delft/ U. of Geneva, Switzerland
Prof. Dr. Y. M. Blanter,	Technische Universiteit Delft
Independent members:	
Dr. K. Lahabi,	Universiteit Leiden, The Netherlands
Dr. I. Lindfors-Vrejoiu,	University of Cologne, Germany
Prof. Dr. B. Noheda,	University of Groningen, The Netherlands
Prof. Dr. ir. T. van der Sar	Technische Universiteit Delft
Prof. Dr. P. G. Steeneken	Technische Universiteit Delft

Printed by: Gildeprint, Enschede

Front & Back: Render of a a perovskite layer being exfoliated.

ISBN 978-94-6518-114-1

An electronic version of this dissertation is available at
`http://repository.tudelft.nl/`.

All research data and code supporting the findings described in this thesis are available in 4TU.Centre for Research Data at
`10.4121/2fd3bf6f-36d7-49a9-af4a-096edef5f46d`.

CONTENTS

ACKNOWLEDGEMENTS

I would first of all like to thank my professor and promoter **Andrea**. I wish you the best of luck with your research group in Geneva, you have a great group of students and colleagues who I know will perform excellent scientific research. **Mattias** and **Ulderico**, your support and camaraderie helped me through tough measurements and fabrication hurdles. It's been a pleasure to work with you both. Ulderico I wish you the best of luck with the rest of your PhD, with your never-ending drive and scientific ability I am confident you will make a great impact in the field of complex oxides. Mattias I expect you to be the scientific and technological head of Bergen next time I see you. **Graham** it was wonderful to have you in the Caviglia group and an absolute pleasure to work with you, I'm sure you'll continue as an excellent researcher in Zurich. **Edouard**, I would like to thank you for your mentorship and support during my first year, without it I simply wouldn't be the person I am today. I would also like to thank all of the **Cleanroom Staff**, your utmost professionalism and approachable nature was genuinely a highlight of my PhD. I can't think of a better group of people to manage and grow the Kavli NanoLab. Outside of academia, I would like to thank **The Leiden Crew** for all the wonderful times we've had. It's been genuinely heartwarming to be welcomed as one of your own, I hope to have many more spelletjesavonds with you in the future! **Brían** and **Nicolas**, you showing me the ways of Navan and Leiden has changed my life forever. Lastly I would like to thank my family for all the support during the trials and tribulations that one naturally encounters during a PhD.

LIST OF ABBREVIATIONS

AFM	Atomic Force Microscopy
AHE	Anomalous Hall Effect
Ca-SAO	Calcium doped Strontium Aluminate
DI	De-ionized water
IV	Current vs Voltage
MIT	Metal to Insulator Transition
MR	Magnetoresistance
NNO	Neodynium Nickelate
PDMS	Polydimethylsiloxane
PLD	Pulsed Laser Deposition
PMMA	polymethyl methacrylate
PPC	polypropylene carbonate
r.l.u	Reciprocal Lattice Units
RHEED	Reflection High Energy Electron Diffraction
RT	Resistance vs Temperature
SAO	Strontium Aluminate
SQUID	Superconducting Quantum Interference Device
SRO	Strontium Ruthenate
STO	Strontium Titanate
TEM	Transmission Electron Microscopy
u.c	Unit Cells
XRD	X-Ray Diffraction

SUMMARY

This thesis explores the growth, fabrication and measurement of freestanding complex oxide membranes. Complex oxides such as $SrRuO_3$ and $NdNiO_3$ are fabricated into a freestanding membrane form, with their numerous intrinsic properties and phenomena characterised and investigated. New techniques describing solutions to the current fabrication hurdles of freestanding complex oxide membranes is discussed, along with the comparison of $SrRuO_3$ and $NdNiO_3$ freestanding membranes and their epitaxial counterparts.

Chapter 1 provides an introduction to the background concepts, materials, and measurement techniques described during this work. Topics include the definition of freestanding membranes and perovskites, topological and electronic phenomenon such as Berry curvature and the anomalous Hall effect, and experimental processes such as pulsed laser deposition and x-ray diffraction.

Chapter 2 provides detailed insights into the structural, electronic, topological and magnetic properties of freestanding $SrRuO_3$ membranes. The sample growth and device fabrication processes are described following which measurements involving diffraction, microscopy, and electron transport were performed. Phenomena such as epitaxial strain, electrical resitivity and the anomalous Hall effect are observed and analysed.

Chapter 3 describes a robust fabrication method to create arrays of custom-shaped complex oxide membranes. It tackles problems such as lattice mismatch, exfoliation times and polymer residues.

Chapter 4 explores the structural and electronic phenomena of freestanding $NdNiO_3$ membranes. $NdNiO_3$'s characteristic metal-to-insulator transition is observed and analysed in freestanding membrane form. Additional details on the hurdles to fabricate freestanding $NdNiO_3$ membranes are discussed.

Chapter 5 explores the type of bonding that occurs between freestanding $SrRuO_3$ membranes and an $SrTiO_3$ substrate they are stamped on. Temperature-dependant X-Ray diffraction measurements are performed along with extensive acoustical phonon measurements via pump-probe spectroscopy. Additionally, reciprocal space mapping of freestanding $SrRuO_3$ is described.

SAMENVATTING

Deze scriptie onderzoekt de groei, fabricage en metingen van vrijstaande complexoxide-membranen. Complexe oxiden zoals $SrRuO_3$ en $NdNiO_3$ worden vervaardigd in de vorm van vrijstaande membranen, waarbij hun talrijke intrinsieke eigenschappen en bijbehorende fenomenen worden gekarakteriseerd en bestudeerd. Er worden nieuwe technieken besproken die oplossingen bieden voor de huidige fabricage-uitdagingen van vrijstaande complexoxide-membranen, evenals een vergelijking tussen vrijstaande membranen van $SrRuO_3$ en $NdNiO_3$ en hun epitaxiale tegenhangers.

Hoofdstuk 1 geeft een inleiding tot de achtergrondconcepten, materialen en meetmethoden die in dit werk worden beschreven. Onderwerpen omvatten de definitie van vrijstaande membranen en perovskieten, topologische en elektronische fenomenen zoals Berry-kromming en het anomalous Hall-effect, en experimentele processen zoals gepulste laserdepositie en röntgendiffractie.

Hoofdstuk 2 biedt gedetailleerd inzicht in de structurele, elektronische, topologische en magnetische eigenschappen van vrijstaande $SrRuO_3$-membranen. Het groeiproces van de monsters en de fabricage van de apparaten worden beschreven, gevolgd door metingen op basis van diffractie, microscopie en elektronentransport. Fenomenen zoals epitaxiale spanningen, elektrische resistiviteit en het anomalous Hall-effect worden waargenomen en geanalyseerd.

Hoofdstuk 3 beschrijft een robuuste fabricagemethode om arrays van complexoxide-membranen in op maat gemaakte vormen te creëren. Hierbij worden problemen zoals rooster-mismatch, exfoliatietijden en polymeerresiduen aangepakt.

Hoofdstuk 4 onderzoekt de structurele en elektronische fenomenen van vrijstaande $NdNiO_3$-membranen. De karakteristieke metaal-naar-isolator-overgang van $NdNiO_3$ wordt waargenomen en geanalyseerd in vrijstaande membraanvorm. Daarnaast worden de uitdagingen bij het vervaardigen van deze membranen besproken.

Hoofdstuk 5 onderzoekt het type binding dat optreedt tussen vrijstaande $SrRuO_3$-membranen en een $SrTiO_3$-substraat waarop ze worden geplaatst. Temperatuurafhankelijke röntgendiffractiemetingen worden uitgevoerd, evenals uitgebreide metingen van akoestische fononen via pump-probe spectroscopie. Ook wordt reciprocale-ruimtekartering van vrijstaande $SrRuO_3$ besproken.

1

INTRODUCTION

The theory, materials, concepts, and measurements are introduced along with a description of freestanding membranes and their usefulness to scientific advancement.

1.1. INTRODUCTION

1.1.1. WHAT ARE 'FREESTANDING' MEMBRANES?

The word '*freestanding*' is perhaps a misnomer. While it implies that the membrane is somehow not attached to any surface, this is not true in most cases. The meaning is more subtle in that its roots stem from the different types of atomic bonds that occur. While complex oxides can be large single crystals, most complex oxides are grown in the form of **heterostructures** which are thin layers of complex oxides grown on top of one another one layer at a time. To grow a heterostructure, a thin, flat, complex oxide crystal (usually in the shape of a cuboid) is designated as the surface to grow other complex oxides on top of. This crystal is called the substrate. Complex oxide thin films can be grown on many types of substrates by a number of different methods (Figure 1.8), but one important similarity between them is that these complex oxide thin films are **epitaxially** bound to one another. These epitaxial bonds generally take place in the form of strong covalent bonding. Complex oxide thin films are very sensitive to this epitaxial bonding, where the characteristics of the substrate alone can greatly influence the properties of the thin films grown on top via this epitaxial bonding. The method to produce freestanding membranes in this work involves dissolving one of these heterostructure layers so that the layers above are no longer epitaxially bound to the substrate. This method is called exfoliation. But, these membranes are very small and thin thus one needs a method to somehow 'hold' on to these membranes once the exfoliation has occurred. Also, it's not enough to simply hold these membranes. Naturally one needs to place them onto some surface in order to perform measurements on them. In this work this was performed by a method called 'dry stamping' which simply involves placing a sticky film on top of the heterostructure before exfoliation. After exfoliation has occurred the membranes will still be attached to the sticky film while the substrate will have fallen away. One can then 'stamp' these membranes onto any desired surface and remove the sticky film. If performed correctly, the membranes will be securely attached to the surface ready to have measurements performed on them. But one might ask how is this situation different from when you simply grow these complex oxide layers on the substrate and just perform measurements on them as is, no exfoliation needed. The difference lies in the atomic bonds. The membranes that have been exfoliated and dry-stamped onto a surface are attached to the surface via Van der Waals forces. These forces are much weaker than covalent epitaxial bonds [1]. Thus when comparing to the film epitaxially bound in a heterostructure, the membrane is 'freestanding' in that it is **no longer epitaxially bound to the substrate it was grown on**.

1.1.2. WHY FREESTANDING MEMBRANES?

As mentioned previously, there are a number of additional steps that one has to perform in order to create complex oxides that are in a freestanding membrane form. So what advantages do these freestanding membranes have over their epitaxial counterparts? One key aspect lies in their flexibility. Having a material that naturally is a bulky, brittle crystal but is now in the form of a thin, flexible membrane drastically changes things. Their material properties can be tuned and measured in ways that would be difficult or otherwise inaccessible in an epitaxial form. For example freestanding complex oxide membranes can be subjected to strains much larger than can be achieved epitaxially[2]. Also strong uniaxial strains can be induced and controlled, something which is difficult to perform epitaxially yet alone controllable. They can also be stamped onto any surface one desires while controlling the angle between the membrane and the surface. This opens up complex oxides to the field of twisted stacking where the angle between the membrane and the surface can greatly influence the membrane's properties[3] via a number of different coupling mechanisms. The membranes can be suspended in the form of a bridge or a drum, allowing acoustic and optical measurements to be performed with large signal-to-noise ratios[4]. Curvature can also be induced to varying degrees, ranging from being stamped on curved surfaces[5] to being rolled up in the form of 'nanoscrolls'[6].

Intuitively one would imagine that producing a crystal in the form of a freestanding membrane will drastically alter its intrinsic properties even before any measurements are performed on it. But surprisingly this is not the case. Even though these membranes can be only a few nanometers thick, they still retain many of their properties that are observed in bulk, single crystals. This is observed multiple times in this work. This is crucial as these freestanding membranes thus provide a reliable platform to probe the material's intrinsic properties seen in its bulk form.

1.2. THEORY

1.2.1. PEROVSKITE STRUCTURE

TOLERANCE FACTOR

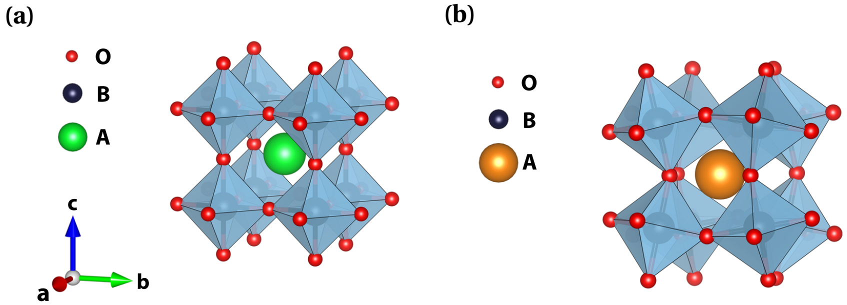

Figure 1.1: (a) Unit cell of a cubic pervoskite. Green represents the larger cation while black is the smaller anion. The anions are surrounded by oxygen atoms (red) resulting in B-O octahedra. Strontium Titanate ($SrTiO_3$) is an example of this structure, with a large central Sr atom and Ti-O oxygen octahedra. (b) Cubic perovskite structure similar to (a) but the central cation is even larger, resulting in the B-O octahedra having to tilt and rotate to accommodate this change in Coulomb repulsion. $CaTiO_3$ is an example of this, with Ca being the larger central atom.

Complex oxides can broadly be defined as a class of inorganic materials that contain oxygen and at least two other elements, usually in the form of cations and anions. They exhibit a number of uniquecrystallographic structures, such as spinel and brownmillerite for example, but the complex oxides of particular interest in this work are also known as perovskites. Complex oxide perovskites have the general chemical formula ABO_3, where A and B are cations and anions respectively and O represents oxygen. These complex oxides exhibit a perovskite crystallographic structure, where the B atom is surrounded by oxygen atoms in an octahedral network, as shown in Figure 1.1. This octahedral network is vital to producing the variety of phenomena that complex oxide perovskites exhibit. This octahedral network can be distorted due to size differences between the A and B atoms. This distortion leads to many complex oxide perovskites having a structure different from the ideal cubic perovskite configuration (Figure 1.1 (b)). This distortion is quantified by a parameter known as the *tolerance factor* t:

$$t = \frac{r_A + r_O}{\sqrt{2}(r_B + r_O)} \tag{1.1}$$

Where r_A, r_B, r_O are the atomic radii of the A,B, and oxygen atoms respectively. When $0.9 < t < 1$ the perovskite structure is usually cubic, meanwhile perovskite structures with $0.7 < t < 0.9$ are usually orthorhombic. Lastly, perovskite structures with $t > 1$ are tetragonal or hexagonal.

STRAIN

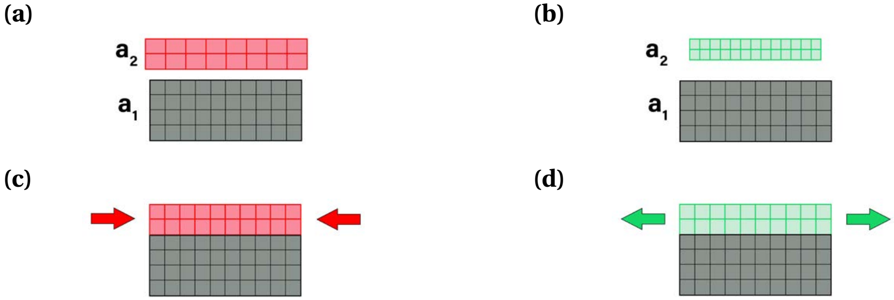

Figure 1.2: Representation of epitaxial strain (a) & (c) Schematic of compressive strain. The red material has a larger cubic lattice parameter than the substrate it is grown on, $a_2 > a_1$. (b) & (d) Schematic of tensile strain. The green material has a smaller cubic lattice parameter than the substrate it is grown on, $a_2 < a_1$. Note the expansion/compression of the material in the z direction due to the strain in the xy plane is not shown here.

The octahedral network can also be distorted by a phenomenon called *strain*, which is most commonly described in terms of epitaxially-grown thin films. Epitaxially-grown thin films are thin layers of materials that are covalently bonded together in an ordered fashion. Stacks of these separate, epitaxially-bound material layers are called *heterostructures*. Strain enables complex oxides of differing atomic spacings and tolerance factors to be epitaxially grown on one another. Strain can be quantified by the parameter a, which is the material's *lattice parameter*. a is the distance between the B atoms in a perovskite unit cell. Consider the heterostructure in Figure 1.2, where a perovskite substrate (denoted index **1**) and a perovskite thin film (denoted index **2**) are epitaxially bound together. In Figure 1.2 (a) $a_2 > a_1$ hence the perovskite thin film has to 'squeeze' in order to conform and fit onto the substrate that it is grown on. The perovskite thin film is said to experience *compressive* strain. Meanwhile in Figure 1.2 (b) $a_2 < a_1$ hence the perovskite thin film has to 'stretch' in order to epitaxially grow on the substrate, hence the perovskite thin film is said to experience *tensile* strain. Additionally, these films compress or expand in a direction (usually) orthogonal to the strain vector (eg. vertically in Figure 1.2) where this compression/expansion depends both on the strain and the material's Poisson vector. Many exotic phenomena found in complex oxides are incredibly sensitive to strain, thus strain can be a powerful tool to investigate these intrinsic properties.

1.2.2. TOPOLOGICAL PHENOMENA

Topological phenomena have been utilised many times to describe and explain multiple exotic phenomena in material physics[7], including physical effects observed in this work. Hence a rudimentary introduction to the background of certain topological topics is required. One can start with the concept of Berry phase which, in the context of this work, is an additional geometrical phase acquired by an electron as it adiabatically traverses a closed loop. In more detail[8, 9]:

Consider a time-dependant Hamiltonian H(t) that depends on a set of parameters $\alpha(t)$. The eigenvalues ϵ and eigenvectors n of this Hamiltonian in an instantaneous orthonormal basis can be written as:

$$H(\alpha(t))|n(\alpha(t))\rangle = \epsilon(\alpha(t))|n(\alpha(t))\rangle \tag{1.2}$$

Also consider the time-dependent Schrodinger equation of a system with a Hamiltonian H and a state function $\Psi(t)$ with time variable t:

$$i\hbar\frac{\delta}{\delta t}|\Psi(t)\rangle = H|\Psi(t)\rangle \tag{1.3}$$

The general solution to this equation, with the Hamiltonian in Equation 1.2 and complete orthonormal eigenvectors and eigenvalues, can be written as:

$$|\Psi(t)\rangle = \sum_n c_n(t)e^{i\theta_n t}|n(\alpha(t))\rangle \tag{1.4}$$

Where $\theta \equiv -\frac{1}{\hbar}\int_0^t \epsilon(\alpha(t))dt$ is a phase factor picked up by the wavefunction as it traverses the wavefunction's parameter space. θ is known as the dynamical phase factor. Using the adiabatic approximation[10], Equation 1.4 can be rewritten as:

$$|\Psi(t)\rangle = e^{i\gamma(t)}e^{i\theta_n t}|n(\alpha(t))\rangle \tag{1.5}$$

Where $e^{i\gamma(t)}$ describes an additional phase picked up by the wavefunction. This phase is determined by the path integral of the wavefunction over the parameter space. This path integral phase is important and can be extracted by plugging Equation 1.5 into Equation 1.3 and multiplying the left-hand side by $\langle n(\alpha(t))|$. This produces the following:

$$\gamma = \int_C d\alpha \cdot A(\alpha) \tag{1.6}$$

Where $A = i\langle n(\alpha(t)|\frac{\delta}{\delta\alpha}|\alpha(t)\rangle$ and is known as the Berry vector potential. The Berry vector potential is gauge dependant hence, for example, if one decides to perform a gauge transformation $|n(\alpha\rangle \rightarrow e^{i\xi(\alpha}|n(\alpha\rangle$, where $\xi(\alpha)$ is some arbitrary function, the Berry vector potential will be changed by $A(\alpha) \rightarrow A(\alpha) - \frac{\delta}{\delta\alpha}\xi(\alpha)$. This highlights that the path integral phase only depends on the initial and final points and not how the path was taken. This gauge transformation requires that $e^{i\xi(\alpha}$ be single valued but historically this was not deemed important as one could always choose a path that caused the path integral phase to be cancelled out[11], leaving the single value of 0. But it was discovered that when the path is a closed loop, the path integral phase can be $2\pi\times$ integer. This path integral phase, created by adiabatically traversing a closed loop, is known as the Berry phase:

$$\gamma = \oint_C d\alpha \cdot A(\alpha) \tag{1.7}$$

While the Berry phase can be very important in certain systems, it is difficult to quantify in the form described in Equation 1.7. Thus one can go a step further and use the Berry vector potential to define a type of 'field' related to the Berry phase. A field tensor based on the Berry vector potential can be defined, mimicking the three-dimensional electromagnetic field tensor commonly seen in electrodynamics[10, 12]:

$$\Omega(\alpha) = \nabla_\alpha \times A(\alpha) \tag{1.8}$$

This field Ω is known as the **Berry curvature**. Using Stoke's theorem the Berry phase can be written as a surface integral of the Berry curvature over a closed volume:

$$\gamma = \int_S d\alpha \cdot \Omega(\alpha) \tag{1.9}$$

While seemingly abstract concepts, Berry Curvature (Equation 1.8) and Berry phase (Equation 1.9) have been shown to be powerful tools in explaining exotic phenomena in complex oxides, such as the anomalous Hall effect described further in Chapter 2.

1.2.3. ANOMALOUS TRANSPORT

Berry Curvature can be used to describe what is known as 'anomalous' velocity in topologically non-trivial materials such as some complex oxides. The velocity operator ($\boldsymbol{v}$) is the time derivative of the position operator ($\boldsymbol{r}$) and is defined as the following[8]:

$$\boldsymbol{v} \equiv \frac{i}{\hbar}[\boldsymbol{H}, \boldsymbol{r}] \tag{1.10}$$

Where $\boldsymbol{H}$ is a Hamiltonian as described in 1.2.2. Now following the reasoning from 1.2.2, derivative operations are also not necessarily gauge invariant. Hence a gauge-covariant derivative in momentum space ($\boldsymbol{k} = k_x, k_y, k_z$) can be introduced:

$$\nabla_{\boldsymbol{k}} \rightarrow \nabla_{\boldsymbol{k}} - iA(\boldsymbol{k}) \tag{1.11}$$

This can be further described by position operators $\hat{x}$ and $\hat{y}$ as:

$$\hat{x} = \nabla_{k_x} - iA(k_x) \tag{1.12}$$

$$\hat{y} = \nabla_{k_y} - iA(k_y) \tag{1.13}$$

Consider now the application of a slowly varying (aka. approximately adiabatic) electric field in the x direction (E_x). It is described by the Hamiltonian $\hat{H} = -eE_x\hat{x}$. Going back to Equation 1.10 and describing it in terms of the position operator $\hat{y}$:

$$\begin{aligned} < \frac{d\hat{y}}{dt} > &= \frac{i}{\hbar}[\boldsymbol{H}, \hat{y}] \\ &= \frac{-ieE_x}{\hbar}[\hat{x}, \hat{y}] \\ &= \frac{eE_x}{\hbar}(\frac{\delta A(k_y)}{\delta k_x} - \frac{\delta A(k_x)}{\delta k_y}) \\ &= \frac{e}{\hbar}E_x\Omega^z_{\boldsymbol{k}} \end{aligned} \tag{1.14}$$

Where $\Omega^z_{\boldsymbol{k}}$ is the Berry Curvature in the z direction of the momentum-space basis*. Hence there is an additional contribution to the velocity and this contribution is perpendicular to the direction to the applied electric field. Additionally this contribution depends on the Berry Curvature and is also perpendicular to it. This Berry Curvature-dependent anomalous velocity has profound effects in the form of unconventional transport phenomenon and additionally helps describe the anomalous Hall effects discussed further in Chapter 2.

1.2.4. MATERIALS USED IN THIS WORK

STRONTIUM RUTHENATE ($SrRuO_3$)

$SrRuO_3$ (SRO) is an orthorhombic perovskite (space group $Pbnm$) where its orthorhombic unit cell can be described by a pseudocubic unit cell of lattice parameter a_{pc} = 3.93Å. The Ru^{4+} atoms have 4 valence electrons and have the electronic configuration [Kr]$4d^4$[14]. The oxygen tetrahedra surrounding the Ru atoms give rise to crystal field splitting which results in the splitting of the 4d band into t_{2g} and e_{2g} orbitals (Figure 1.3 (b)). These four valence electrons in the t_{2g} orbitals in combination with the Ru atom's large spin-orbit coupling give rise to a rich phase space for high conductivity, magnetism, and topological phenomena.

---

*A good discussion for Berry Curvature described in terms of gauge derivatives can be found in Xiao et al [8]. The anomalous velocity was first derived by Karplus & Luttinger in 1954[13].

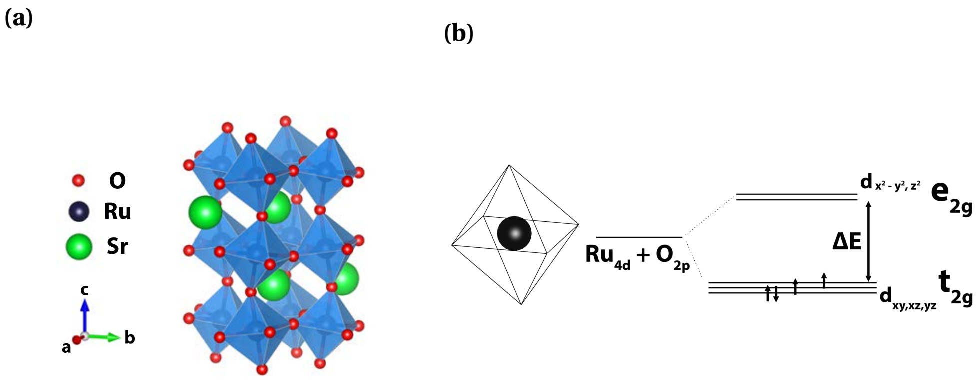

Figure 1.3: (a) Orthorhombic unit cell of $SrRuO_3$ (b) Crystal field splitting of a Ru atom inside and bonded via an oxygen octahedra. The degeneracy of the Ru 4d valance band (hybridized with the O 2p band) is split into lower level t_{2g} and higher level e_{2g} orbital orbitals. The small arrows represent the spins (up or down) of the occupying electrons. A high spin state (S = 1) of the t_{2g} orbitals is shown which occurs due to Hund's rules.

NEODYNIUM NICKELATE ($NdNiO_3$)

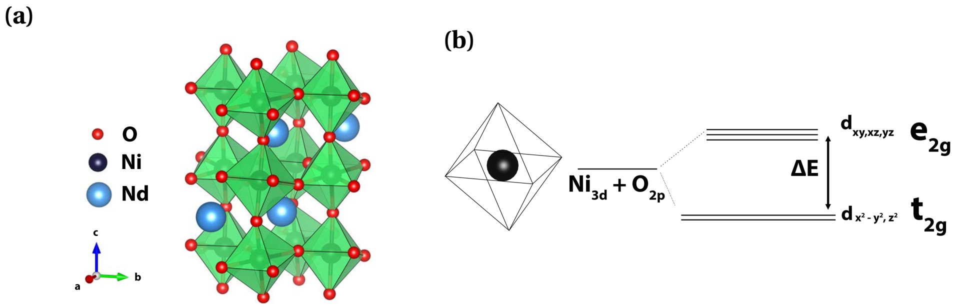

Figure 1.4: (a) Orthorhombic unit cell of $NdNiO_3$ (b) Crystal field splitting of the Ni atom inside the oxygen octahedra. The Ni 3d band, hybridized with the O 2p band, has its degeneracy broken and separates into higher energy e_{2g} orbitals and lower energy t_{2g} orbitals. The electron occupation is not shown as there are additional factors that need to be taken into account (Section 4.2).

$NdNiO_3$ (NNO) is also an orthorhombic perovskite (space group $Pbnm$) with a pseudocubic lattice parameter of $a_{pc} = 3.81$Å. The Ni^{3+} atoms have 7 valence electrons and have the electronic configuration $[Ar]3d^7$. Crystal field splitting also occurs resulting in the splitting of the 3d band into t_{2g} and e_{2g} as shown in Figure 1.4 (b). But, this picture is not entirely correct as there are multiple additional factors that need to be taken into account. To start, the Ni 3d bands are very narrow and hybridize with the surrounding O 2p orbitals. This helps explain its (electronic) insulating properties. In more detail:

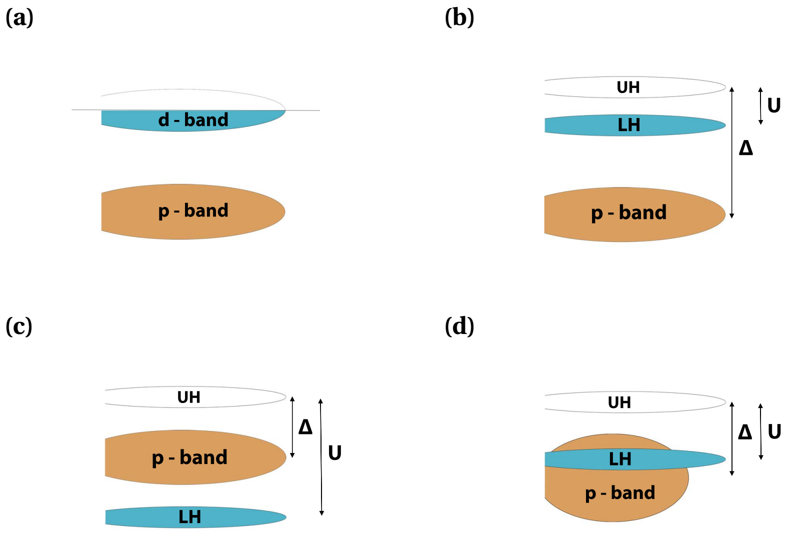

Figure 1.5: (a) Half-filled conduction d-band and fully-filled valance p-band (b) Mott insulator, where the d-band splits into an empty Upper Hubbard band (UH) and full lower Hubbard band (LH) (c) Charge transfer insulator with charge-transfer gap Δ. (d) Small/negative charge transfer insulator due to the strong hybridization of the p and d-bands.

It was observed that bulk NNO is a paramagnetic metal at room temperature and undergoes a metal-to-insulator transition (MIT) to become an antiferromagnetic insulator as the temperature is cooled below 200K[15]. Mott physics plays a role, where a Mott insulator is described as a half-filled d band splitting into an empty upper Hubbard band (UH) and a full lower Hubbard band (LH) due to the 3d band's narrowness and Hund's Rules[16] (Figure 1.5 (b)). In some cases a p-band (such as an O-2p band) can energetically lie between the UH and LH band resulting in Figure 1.5 (c). This configuration is described as a charge-transfer insulator, where the energy difference between the p-band and the UH band is called the charge-transfer gap. For NNO one has to take the strong Ni 3d and O 2p hybridization into account. This results in the charge-transfer gap being very small or even negative (Figure 1.5 (d)). Thus NNO is sometimes described as a negative charge-transfer insulator[17]. Historically this was believed to be the sole reason for NNO's MIT[18] where it occurred due to NNO undergoing a phase transition to a charge-transfer insulator. In recent times it has been discovered that the exact origin of its MIT is more subtle than this and NNO is no longer described as a charge-transfer insulator but instead experiences bond-disproportonation[19]. This is described further in Chapter 3. Regardless the above explanation provides a rudimentary overview required for beginning to understand the electronic properties of NNO.

Tri-Strontium Aluminate

Tri-Strontium Aluminate (SAO) has the chemical formula $Sr_3Al_2O_6$ with cubic space group *Pa3*. While it is not a perovskite it has in recent times proved a reliable method for producing freestanding complex oxide perovskite membranes by acting as a sacrificial layer[20]. One reason for this is that SAO has a high water solubility[21] while many complex oxides do not. To understand this one needs to look at its (rather complicated) crystal structure shown in Figure 1.6. The first noteworthy feature is the rings of Al_2O_6 tetrahedra that exist in its unit cell (Figure 1.6 (b)). These Al_2O_6 rings are key to its water solubility. Water molecules hydrolyse the Al-O bonds resulting in these Al_2O_6 rings being broken, thus causing the material to quickly dissolve. This reaction is described as[22]:

$$3SrO \times Al_2O_3 + 6H_2O \rightarrow 3SrO \times Al_2O_3 \times 6H_2O \tag{1.15}$$

The activation energy of this hydrolysis is influenced by the distortion of these Al_2O_6 rings, where the distortion manifests itself as changes to the bond angles of a number of Al-O bonds in both the Al_2O_6 tetrahedra and the bonds creating the rings. These changes in bond angle, and hence their polarisability, influence their degree of reactivity with water molecules[23].

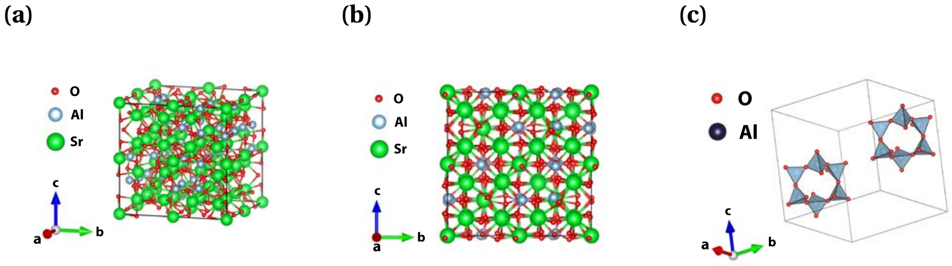

Figure 1.6: (a) Cubic unit cell of $Sr_3Al_2O_6$ (b) Looking down the a-axis of the unit cell shown in (a). This represents the (001) plane. (c) The unit cell shown in (a) with multiple atoms and bonds removed to highlight the existence of the AlO_6 rings.

While this may help explain its water solubility it does not explain its connection to perovskites. The key to that lies in its unique surface. Surprisingly, the (001) plane of SAO is remarkably similar to the (001) plane of Strontium Titanate (STO) where the (001) plane of one unit cell of STO matches one-quarter of the (001) plane of an SAO unit cell, as seen in Figure 1.7. It should be noted that while these planes match very well, it is not exact. Comparing the (001) SAO plane to the (001) STO plane, there are vacancies on the (001) SAO plane. Nevertheless, it has been shown that SAO thin films can epitaxially grow on STO substrates or thin layers. If one can grow other complex oxide perovskite thin films on top of this SAO layer, this provides a route to create freestanding complex oxide perovskite membranes via exfoliating the SAO layer.

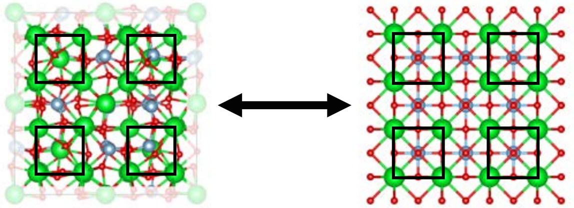

Figure 1.7: The (001) plane of one unit cell of SAO (left) and the (001) plane of four unit cells of STO (right). The black squares highlight the similarities between the two.

1.3. EXPERIMENTAL TECHNIQUES

1.3.1. THIN FILM GROWTH

PULSED LASER DEPOSITION

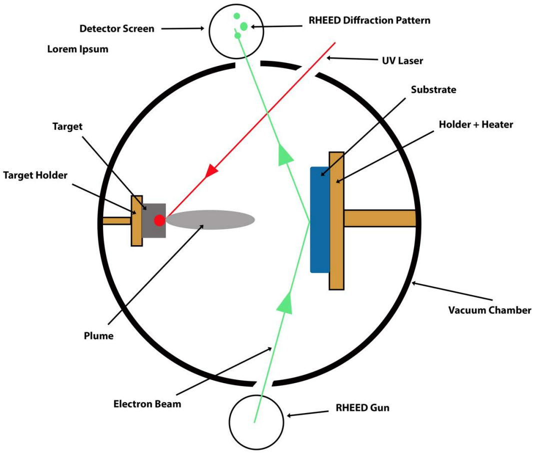

Figure 1.8: Schematic of thin film epitaxial growth via Pulsed Laser Deposition with the growth and film thickness monitored *in-situ* via RHEED

Pulsed Laser Deposition (PLD) is a well-established technique used to epitaxially grow thin films and heterostructures. A schematic of the process is outlined in Figure 1.8. A 1-inch circular block (known as a target) is inside a vacuum chamber. This target is a stoichiometrically-balanced solid consisting of atoms or species that the user inevitably wants to grow into thin films. Nearby (55 mm away to be exact) is a substrate that is the surface the atoms from the target will epitaxially grow on. Before the growth process begins the substrate is heated to hundreds of degrees creating a surface where it is energetically favourable for deposited atoms to move freely before undergoing the epitaxial growth process. A powerful UV laser is fired, at rates of 1-10Hz, at the target. Immediately after each pulse a plume of the target atoms/species is ejected from the target and travels in the direction of the substrate. The plume atoms/species then land on the substrate and epitaxially grow on its surface. A number of different epitaxial growth mechanisms can occur depending on the temperature of the substrate, the pressure of the chamber, and the laser fluence. Each of these parameters are tested and varied in order to enable to most optimal growth conditions of the desired thin film. A number of different thin films can be grown on top of one another in the same growth session, creating a stack of thin films known as a heterostructure. The growth of these thin films can be monitored *in-situ* using reflection high-energy electron diffraction (see Section 1.3.2).

1.3.2. THIN FILM CHARACTERISATION

X-RAY DIFFRACTION

X-Ray Diffraction (XRD) is a technique commonly used to determine a number of characteristics of thin films, such as crystallinity, thickness, strain, and mosaity. The technique is based on Bragg's Law of diffraction where $2d\sin(\theta) = n\lambda$, see Figure 1.9. X-rays in particular are used as their wavelength is on the order of the atomic distances between atoms (atomic spacings in complex oxides $\sim 3-4$Å, x-ray wavelength from standard Cu2α radiation: $\lambda = 1.5406$Å), hence the diffraction of coherent X-rays can be sensitive to the atomic spacings of the material. The resulting diffraction patterns are commonly described by interactions of diffraction peaks with the corresponding Ewald sphere.

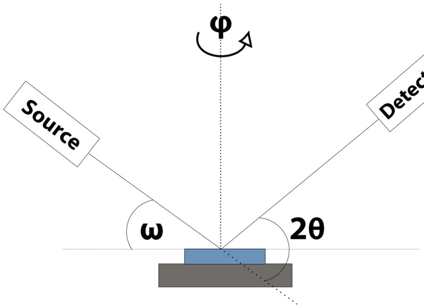

Figure 1.9: Schematic outlining the measurement process and with the appropriate angles defined. ω is the angle between the source and the film, 2θ is the angle between a projection of the source beam and the detector while ϕ is the angle of rotation around the z-axis

RHEED

Reflection High Energy Electron Diffraction (RHEED) is a method used to characterise surface crystallinity of thin films. It is commonly used *in-situ* while growing epitaxial thin films via pulsed laser deposition. Its usefulness shines here as it can determine both the crystalline quality of the thin films as you grow them, but it can also be used to determine the growth rate of the thin films. When accurately aligned, desired diffraction spots can be observed due to diffraction rods intersecting the Ewald sphere.

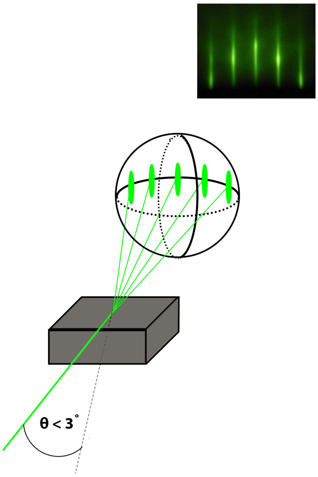

Figure 1.10: Schematic of a RHEED measurement with a low angle ($\theta < 2^\circ$) electron beam striking the film surface. The electron beam diffracts and, depending on the surface quality and crystallinity, diffraction rods intersect with the Ewald sphere as shown. This can be recorded on a screen with green spots and stripes indicating the intersection of these diffraction rods with the Ewald sphere. An example of a typical RHEED pattern is also shown.

By continuously recording the intensity of these diffraction pattern spots during growth, the oscillations in the peak intensity can determine how many unit cells were grown. The peak intensity is at a maximum when the electron beam diffracts from the surface edge of a complete unit cell. Hence this can be used to give a reasonable estimate of the thickness of the film (no.pulses fired/pulses per u.c). In Figure 1.11, the peak of each oscillation occurs with a period of roughly 140 laser pulses (fired at 1Hz). Thus a total of 1400 pulses created a film corresponding to $\sim$ 10 unit cells.

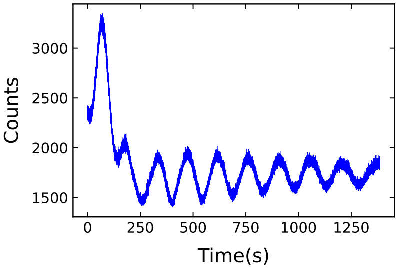

Figure 1.11: RHEED growth pattern of an NNO film grown on an LAO(001) substrate. After the initial peak due to heteroepitaxy, each peak corresponds to the growth of one unit cell of NNO. The growth rate of this sample is $\approx$ 40 pulses per unit cell

1.3.3. FABRICATION

ELECTRON BEAM LITHOGRAPHY

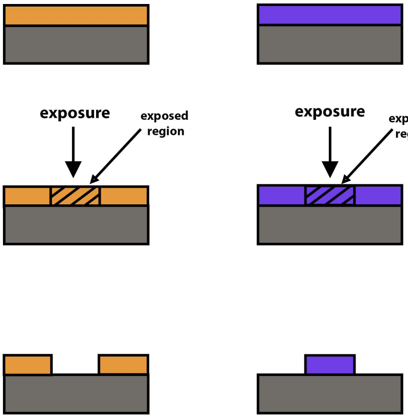

Figure 1.12: Representation of resists. A positive resist (orange) only becomes soluble in a developer after being exposed to an electron beam. Meanwhile a negative resist (blue) is insoluble in a developer only when it is exposed to an electron beam

Electron beam lithography is a sample fabrication process that is vital not just to thin-film research but to the semiconductor industry as a whole. It enables the creation of patterned nanostructures, electrical contacts, selective etching and additionally, in our case, exfoliation of epitaxially-grown thin films. A core aspect of the lithography process is the chemical properties of certain polymers, known as resists, which exhibit changes in their chemical bonding properties via exposure to an electron beam*. There are two types of resists, positive and negative. An example of a standard lithography processes utilising both types of resists is shown in Figure 1.12. After a positive resist is exposed to an electron beam it will be chemically etched away by a select chemical known as a developer. Meanwhile the unexposed polymer is unaffected. For a negative resist the opposite occurs, where the unexposed regions are chemically etched away via a reaction to a developer while the exposed regions are unaffected.

---

* The same process can occur for polymers that react to certain wavelengths of light, this is known as optical lithography.

1.4. CONCLUSION

This chapter provides an outline of the materials used, measurement techniques performed, and the background theory relevant to this work. A fundamental description of freestanding membranes and their advantages over their epitaxial counterparts are discussed.

2

FREESTANDING $\mathrm{SrRuO_3}$ MEMBRANES

Nanometer-thin freestanding Strontium Ruthenate membranes were fabricated. Extensive characterisation measurements provided detailed insight into their growth and structural properties. Electrical transport measurements demonstrate the preservation of the material's intrinsic properties after exfoliation. SQUID measurements highlight the ability to tune the material's strong magneto-crystalline anisotropy via exfoliation. Lastly, extensive anomalous Hall effect and magnetotransport measurements demonstrate how the material's topological properties can be manipulated by strain release via exfoliation.

2.1. INTRODUCTION

Freestanding membranes are an exciting recent development in the field of complex oxides, allowing intrinsic material properties and phenomena to be probed in ways that would be difficult or otherwise inaccessible in epitaxially-bound heterostructures. $SrRuO_3$ is a highly conducting itinerant ferromagnet, with applications ranging from high-quality electrodes[24] to magnetic tunnel junctions [25], but little is known about its magnetotransport phenomena in its freestanding form. By employing a water-sacrificial layer $Sr_3Al_2O_6$, strain-free ultra-thin $SrRuO_3$ membranes were created exhibiting bulk lattice parameters (c = 3.929 Å), an increase in Curie temperature ($\Delta T_c \sim 10$ K), and a shift of the easy axis angle ($22° \pm 2°$). A reduction in the anomalous hall signal and a sign change of magnetoresistance was observed, indicating a smaller out-of-plane magnetisation. Our measurements provide a first insight into the magneto-electronic properties of $SrRuO_3$ membranes, highlighting the influence of the exfoliation process and paving the way for the future applications of freestanding conducting perovskite membranes. Utilising methods that can reduce the complexity of this multi-variable landscape while at the same time directly influencing the electronic and magnetic properties are crucial to understanding the exotic properties of SRO. The goal of this work was to compare the structural and magnetotransport properties of SRO before and after this exfoliation process.

2.2. MAGNETIC ANISOTROPY IN SRRUO3

SRO has a strong uniaxial anisotropy (anisotropy constant 1.2×10^7 ergs·cm^3[26]) which arises from the electronic configuration of its 4+ Ru atom. Four electrons lie in the t_{2g} orbitals and due to Hund's rules undergo a spin configuration of (↑↓↑↑). In addition, the octahedral network surrounding the Ru atom quenches the orbital momentum in specific directions resulting in the Ru atom's orbital moments being largest in particular directions. The spin of the (↑↑) valence electrons then couple to these specified Ru orbital momentum directions, resulting in a strong magnetic anisotropy. In bulk form SRO has an easy axis of ~ 25° off its normal[27, 28], as shown in Figure 2.1.

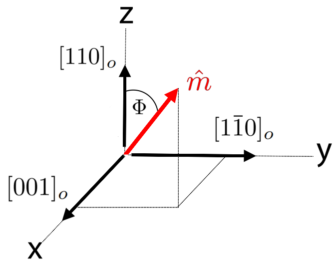

Figure 2.1: Easy axis of unstrained SRO displayed in both orthorhombic and cartesian coordinates. The easy axis direction is represented by the red arrow which deviates an angle Φ from normal and lies between the $[001]_o$ and $[1\bar{1}0]_o$ directions.

2.3. BERRY CURVATURE

As described in the introduction chapter (Section 1.2.2) Berry curvature is a topological field relating to the Berry phase, which is the additional geometrical-dependant phase that a state function picks up as it adiabatically traverses a closed path. While it was described in a general case, its relation to band structure, symmetries, and spin-orbit coupling are vital to understanding its effects on magentotransport phenomenon observed in complex oxides such as SRO.

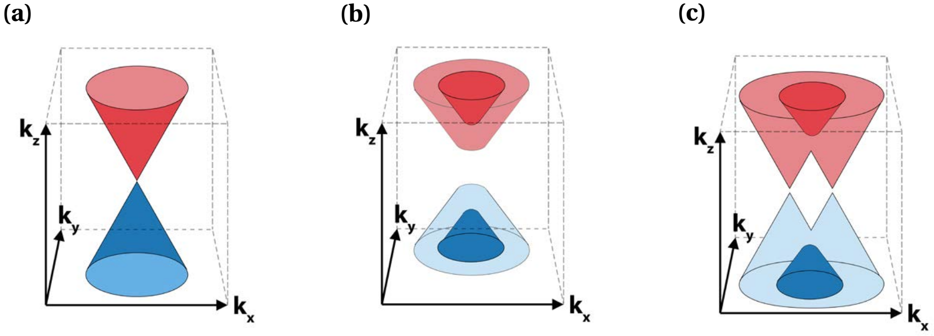

Figure 2.2: Examples of band crossings/anti-crossings between a conduction band (red) and valence band (blue) (a) Dirac point of a non-magnetic metal with massless fermions (b) Band anti-crossing of a metallic ferromagnet with low spin-orbit coupling and carriers exhibiting a finite effective mass. The degeneracy of the valence and conduction bands are split with each sub-band exhibiting a spin majority. (c) Weyl point of a metallic ferromagnet exhibiting strong spin-orbit coupling. Spin-orbit coupling in combination with the preservation of time-reversal symmetry results in the creation of a pair of Weyl nodes with opposite chiralities.

SRO is classified as a Weyl semimetal, this is where the valence and conductance bands coincide at some points across the Brillouin zone. These points are crucial to the origin of non-zero Berry curvature observed in SRO. Figure 2.2 (a) represents a band anti-crossing of the valence band and the conductance band in a standard non-magnetic metal. If the metal is a ferromagnet the degeneracy of the bands is broken due to magnetic ordering, as shown in Figure 2.2 (b). The band are split depending on their respective majority spins. These point where the bands touch are known as Weyl nodes. If one considers an electron traversing around a Weyl node, these Weyl nodes act as monopoles of Berry flux, ie. are sinks and sources of Berry curvature[29]. Each Weyl node has a chirality, which describes the ’handedness’ of the Berry flux about that node. This chirality* is denoted C and can be ±1. The total chirality inside an enclosed volume depends on the number of Weyl points (aka. the number of Berry curvature monopoles) inside the volume. But, according to the ‘no-go theorem’ C needs to be zero when integrating over the entire Brillouin zone[30, 31]. Hence Weyl nodes come in pairs, ie. A Weyl point consists of two Weyl nodes of opposite chirality separated in momentum space, as shown in Figure 2.2 (c). The Berry flux at Weyl nodes is a local property in that it is cancelled out when integrating over the entire Brillouin zone.

---

*This chirality value is also known as the Chern number.

With regards to SRO, Weyl nodes that exist close to the Fermi level can contribute to a number of phenomena in complex oxides, such as the anomalous Hall effect.

2.4. ANOMALOUS HALL EFFECT IN SRRUO3

$SrRuO_3$ (SRO) is an excellent platform to observe the anomalous Hall effect (AHE) due to its itinerant ferromagnetism and Berry curvature[32]. Anomalous Hall effect measurements are a powerful tool for investigating magneto-electronic phenomena in conducting ferromagnets as it has a rich dependence on the materials' magnetisation, spin-orbit coupling, and topological landscape.

A phenomenological model describing the anomalous Hall effect in SRO is the following[26]:

$$\rho_{xy}^{\mathrm{AHE}} = (a\rho_{xx} + b\rho_{xx}^2)\mu_0 M_\perp \tag{2.1}$$

Where ρ_{xy}^{AHE} is the anomalous hall resistivity, ρ_{xx} the longitudinal resistivity, $M_\perp$ the out-of-plane magnetisation and μ_0 the vacuum permeability. The linear resistivity component of equation 2.1 is attributed to the extrinsic mechanisms that describe the anomalous Hall effect, such as skew scattering[33], while the quadratic resistivity term is attributed to the side jump mechanism[34]. But in recent times it has been shown that the topological landscape also plays a role, where there is an additional AHE mechanism (known as the 'intrinsic' mechanism) that depends on the band structure of the material. Specifically, this intrinsic mechanism originates from the fact that integrating the Berry curvature over the Fermi surface can give rise to a transverse conductivity[29, 35]. The magnitude of this transverse conductivity depends on the separation of paired Weyl nodes in crystal momentum space, where it is assumed the chemical potential lies at the Fermi level. Phenomenologically this transverse conductivity can be described by the following[29]:

$$\rho_{\mathrm{AHE}}^{xy} = -\rho_{xx}^2 \sigma_{xy}^{\mathrm{BP}}(M_\perp) \tag{2.2}$$

Where $\sigma_{xy}^{\mathrm{BP}}$ is the Berry phase transverse conductivity, which scales with $M_\perp$. This interplay of intrinsic and extrinsic mechanisms, along with the influence of $M_\perp$, gives rise to the complex dependence of ρ_{AHE} on the electronic and magnetic properties of SRO[36, 37, 38].

2.5. FABRICATION AND EXPERIMENTAL PROCEDURE

15 u.c of the sacrificial layer strontium aluminate $Sr_3Al_2O_6$ (SAO) was grown on a TiO_2 terminated STO(001) substrate (Crystec). Thin films of SRO were then grown on top of this layer while capped with 8 unit cells (u.c) of $SrTiO_3$ (STO) on both sides. The laser ablation was performed using a KrF eximer laser (Coherent LPXpro 305, $\lambda = 248$nm) with a pulse frequency of 1Hz. The total heterostructure consisted of STO(001)/SAO/STO/SRO/STO (Figure 2.3 (a)). The following labels represent the samples with the corresponding thickness of the SRO layer: **Sample A ≈ 40 unit cells, Sample B ≈ 14 unit cells, Sample C ≈ 6 unit cells**. The thickness was monitored *in situ* using Reflection High Energy Electron Diffraction (RHEED) and each sample was post O_2 annealed with 300 mbar O_2 at 550°C. The resulting heterostructures' structural characteristics were measured via XRD and AFM. Following this, aluminum contacts were wire bonded to the corners of each sample in a Van Der Pauw geometry. Magneto-transport measurements were then performed using a custom He cryostat with a 10T superconducting magnet. The samples were then exfoliated by attaching each to a PDMS stamp and being exposed to deionised water for 24 hours. Each PDMS stamp was then stamped onto a commercial Al_2O_6 substrate (SurfaceNet). The XRD measurements were repeated for these SRO membranes on Al_2O_6. Using PDMS domes coated with PPC, suitable flakes stamped on the Al_2O_6 substrate were then transferred onto a pre-patterned Silicon substrate via a dry stamping technique. Using electron lithography and deposition, Hall contacts of Palladium were deposited onto each flake where the outer STO capping layer was etched away via Argon milling prior to the Palladium deposition. The magneto-transport measurements in the He cryostat were then repeated for these flakes.

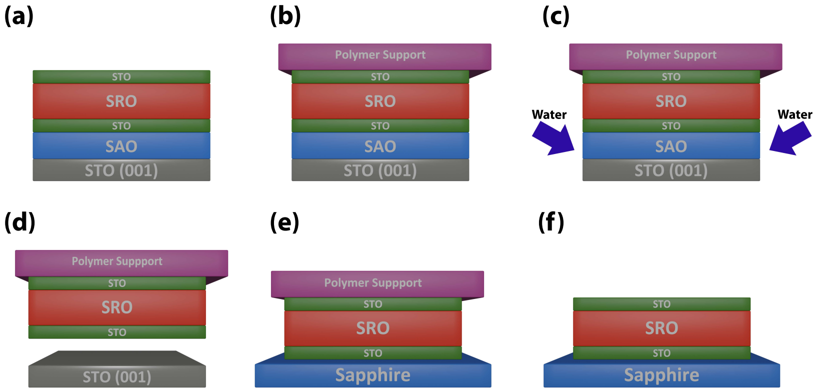

Figure 2.3: Illustration of the exfoliation and transfer technique. (a) STO(001)/SAO/STO/SRO/STO heterostructure (b) PDMS stamp placed on top of the heterostructure (c) Heterostructure and PDMS stamp are immersed in de-ionised water for 24 hours. The de-ionised water dissolves the SAO layer. (d) The substrate is separated from the epitaxial layers due to the SAO layer dissolving. (e) The STO/SRO/STO layers are stamped onto a sapphire substrate. (f) The PDMS stamp is removed and the STO/SRO/STO layers remain on the sapphire substrate.

2.6. SAMPLE GROWTH

2.6.1. REFLECTION HIGH-ENERGY ELECTRON DIFFRACTION

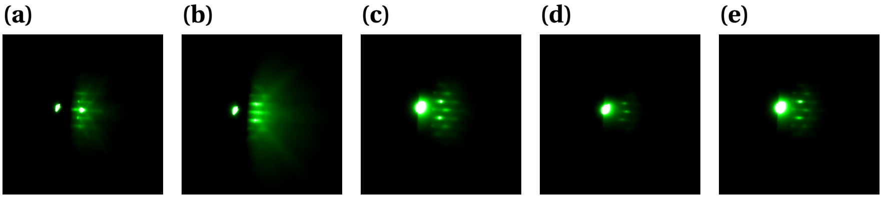

Figure 2.4: RHEED patterns recorded of sample C during the PLD growth process. (a) STO(001) substrate (b) SAO (c) STO 1st layer (d) SRO (e) STO 2nd layer

Figure 2.4 shows the RHEED patterns recorded for sample C during the PLD growth process. Similar patterns were seen for all three samples. The SAO RHEED (Figure 2.4 (b)) has large stripes indicative of a flat surface with small domains. Both the 1st and 2nd STO layers (Figure 2.4 (c) and (e)) show a pattern resembling 3D island growth. Lastly the SRO layer (Figure 2.4 (d)) resembles more of a multi-level stepped surface. Oscillations of the peak intensity for each layer was recorded. The RHEED oscillations for SAO and STO are described further in Chapter 2. Note no oscillations were found for the SRO layer. This could be due to either step-flow growth or the high O_2 pressures reducing the diffraction peak resolution recorded.

2.6.2. GROWTH PARAMETERS

SAO requires low pressures and high temperatures to grow epitaxially, meanwhile SRO requires relatively low temperatures and high pressures. Thus after the SAO layer was grown the temperature of the substrate (750°C) was cooled (rate of $\sim 10°$C per minute) to 550°C. Then a higher flow of O_2 was introduced into the chamber until an equilibrium at the appropriate pressure (1×10^{-6}mbar) was met. The SRO and STO capping layers were then grown while maintaining these temperature and pressure parameters. After the growth of the top STO capping layer was completed, the substrate was cooled to $350°C$. The substrate was then annealed in 300mbar O_2 for one hour at this temperature, after which the substrate was cooled to room temperature and the O_2 gas was evacuated.

Layer	**Temperature (°C)**	**Pressure (mbar)**	**Fluence* (J/cm^2)**	**No.Pulses**	**No.Unit Cells**
SAO	750	1×10^{-6}	1.2	700	15
STO (1st)	550	1×10^{-1}	1	400	8
SRO	550	1×10^{-1}	1	1555(6uc) 3500(14uc) 10000(40uc)	Varied
STO (2nd)	550	1×10^{-1}	1	400	8

---

*With a rectangular laser spot area of $2cm^2$

2.7. RESULTS AND DISCUSSION

2.7.1. AFM

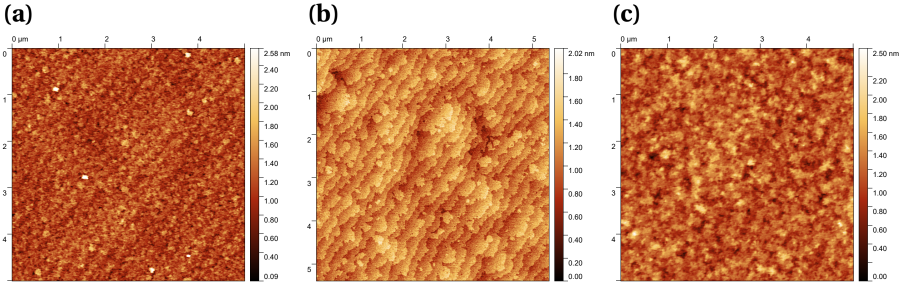

Figure 2.5: AFM scans of the surface of top STO capping layer for each SRO heterostructure grown. (a) Sample C - 6uc (b) Sample B - 14uc and (c) and Sample A - 40uc samples before exfoliation

Large differences can be seen of the surfaces of the three samples (Figure 2.5) where AFM measurements of the top STO layer of each heterostructure was performed. Sample C exhibits the more step and terrace like surface akin to the (001) STO substrate the heterostructure was grown on. Meanwhile sample B exhibits a surface much more resembling high-quality SRO films, with the characteristic budding pattern[26]. Lastly the surface of sample A indicates a more disordered surface with the budding pattern no longer seen. Qualitatively one can hypothesise the following: The SAO and first STO capping layers are very thin (≈ 6nm in total) thus little strain relaxation occurs. Thus if a very thin SRO layer is then grown on top it would be strongly compressively strained (as shown in Figure 2.6). Meanwhile if a thicker SRO film is allowed to grow (14 unit cells), a larger degree of homoepitaxy occurs allowing the budding growth mechanism to occur. That being said it is unclear why this pattern is lost when even thicker films are grown (40 unit cells). It could be related to the fact that while the SAO (001) plane is similar to STO there are intrinsic vacancies (Figure 1.7) which may result in a disorder that compounds over an increasing amount of unit cell growth. A similar disorder is seen in Chapter 3 for nickelate films grown on strontium aluminates.

2.7.2. X-RAY DIFFRACTION

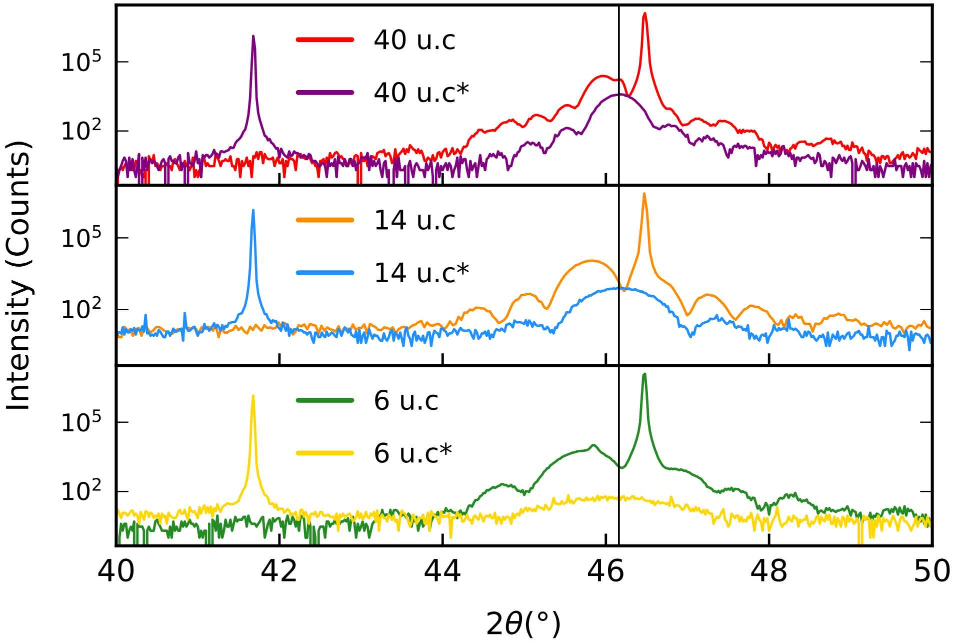

Figure 2.6: (a) X-Ray diffraction spectra of samples A,B and C before and after exfoliation. The * represents the sample after exfoliation. The vertical line at $2\theta = 46.16°$ represents the bulk value of the SRO (002) peak. The sharp peak at $2\theta = 41.68°$ is the (0006) peak of the Al_2O_3 substrate that the exfoliated samples were stamped onto.

Figure 2.6 shows the XRD spectrum obtained for each sample before and after exfoliation. Figure 2.7 shows the fit used to extract the approximate thickness, lattice parameters, and strain state of each material layer. Note it was difficult to accurately fit the exfoliated 6uc SRO sample (Sample C) due to its low intensities. SRO has a bulk lattice parameter of 3.93 Å, which produces a (002) 2θ peak at 46.16°[39]. Due to SRO having a larger lattice parameter than STO (3.905 Å), SRO epitaxially grown on STO substrates experiences a compressive strain of 0.47%[40]. A signature of this compressive strain is found in the (002) 2θ peak position, which shifts to a lower value due to the c lattice parameter increasing. For all three epitaxially bound samples, the (002) 2θ peak was shifted to values lower than bulk (40uc film - 45.96° (0.43%), 14uc film - 45.805° (0.76%), 6uc film - 45.74° (0.91%)), indicating that all three samples experienced compressive strain in their epitaxial form. While the sacrificial layer SAO has a larger lattice parameter (3.99Å), this layer was very thin (15 unit cells) thus it also maintained a lattice parameter similar to the STO substrate, ie. it did not undergo thickness-induced strain relaxation. After exfoliation the (002) 2θ peak reverts back to its bulk value (40uc and 14uc - 46.16°, 6uc - 46.14-16°), indicating that the SRO film is stain-free in its membrane form. The fitting in Figure 2.7 was performed via a kinematical model[41]. Based on the fitting, the STO capping layers on both sides conform to the SRO layer, resulting in the STO lay-

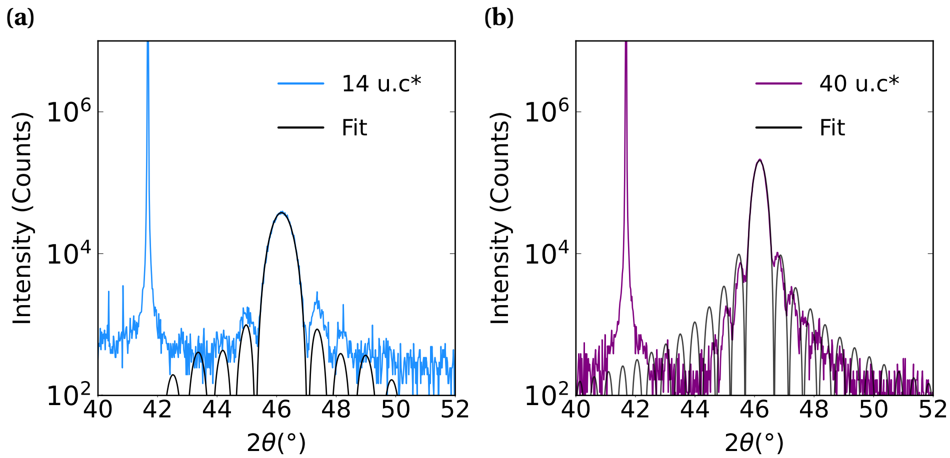

Figure 2.7: (a) XRD fitting of sample B (14 u.c) sample after exfoliation (b) XRD fitting of sample A (40 u.c) after exfoliation

ers having a larger-than-bulk lattice parameter of 3.92Å. While this is puzzling as STO has a larger Young's modulus than SRO (bulk STO Young's modulus - 279 GPa[42], bulk SRO Young's modulus - 161 GPa[43]) it has recently been observed that SRO can have a smaller Young's modulus in its freestanding form compared to bulk[44]. The same phenomenon could perhaps occur for STO and, due to the SRO layer being thicker than the STO capping layers for samples A and B, it could happen to a larger degree to STO than SRO.

2.7.3. ELECTRON TRANSPORT

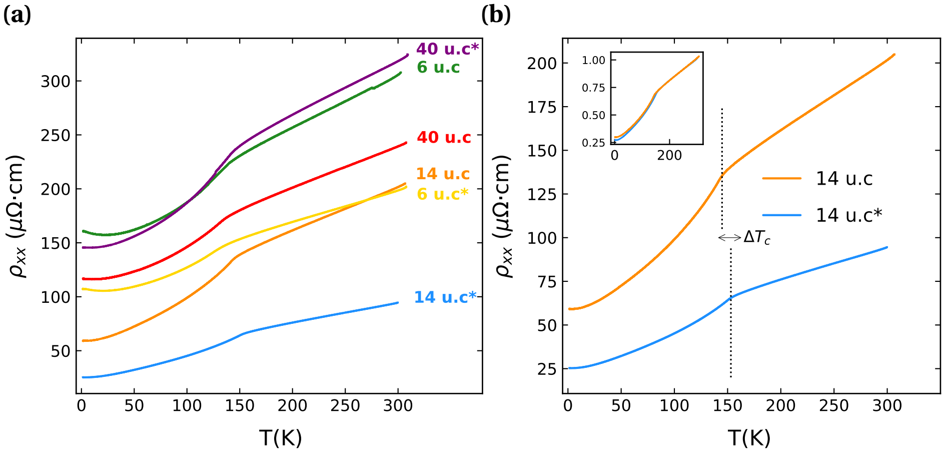

Figure 2.8: (a) Resistivity vs Temperature of samples A,B and C before and after exfoliation. The * represents the exfoliated form of the sample. (b) Resistivity vs temperature for Sample B before and after exfoliation. The dotted lines represent the T_C value. The data normalised with respect to room temperature is shown in the inset.

Figure 2.8 (a) shows the resistivities vs temperature of the SRO film of each sample before and after exfoliation. All the curves display a kink which is indicative of the transition from paramagnetic to ferromagnetic as the temperature is reduced.[45]. This kink represents the Curie temperature (T_C) of the SRO film. In Figure 2.8 (b) an increase of T_C is observed for Sample B, with ΔT around 7K (145K → 153K). This increase in T_C is attributed to the strain release via exfoliation[46, 47, 48, 49, 50]. The release of compressive strain increases the tilting of the RuO_6 octahedra, resulting in a larger overlap and hybridization of the Ru_{4d} (d_{xy}, d_{yz}) - O_{2p_π} orbitals[51]. This increased orbital overlap results in an increased thermal stability of the electrons responsible for the net magnetic moment.

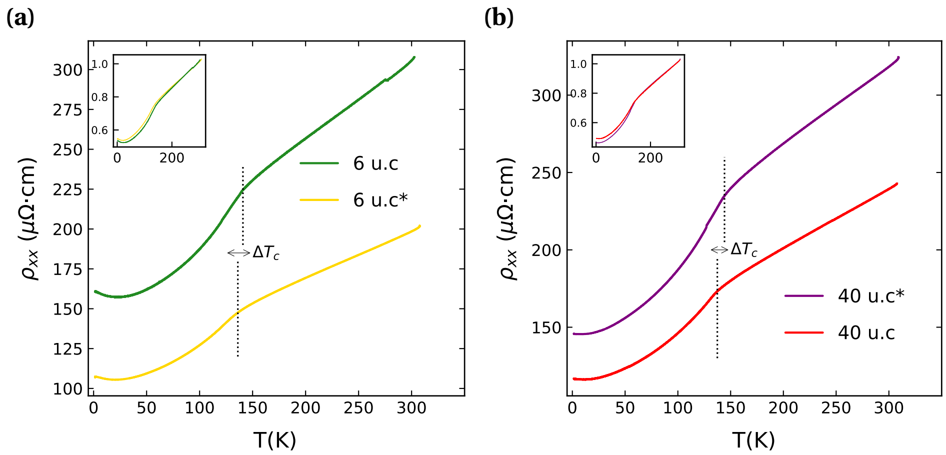

Figure 2.9: (a) Resistivity vs Temperature of Sample C before and after exfoliation. The arrows represent the value of T_C for each sample respectively. (b) Resistivity vs temperature for Sample A before and after exfoliation. The dotted lines represent the T_C value. The data normalised with respect to room temperature is shown in the inset.

Figure 2.9 highlights that the T_C increases for sample A after exfoliation (138K → 144K, $\Delta T \approx$ 6K) while it decreases for sample C (141K → 136K, $\Delta T \approx$ -5K). Sample C deviating from the behaviour of sample A and B could be an indication of lower film quality due to defects, particularly due to the increased broadness of its ferromagnetic transition. Figure 2.10 highlights the lack of change of normalised resistivity values for each sample after exfoliation. Sample B has overall lower ρ^0_{xx} than sample A and C, this could be related to the quality of the growth shown in Figure 2.5 where sample B exhibits the characteristic budding pattern of high-quality SRO thin films.

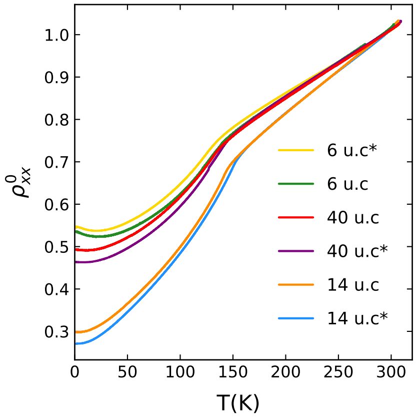

Figure 2.10: Resitivities normalised with respect to their room temperature values vs temperature

2.7.4. SQUID

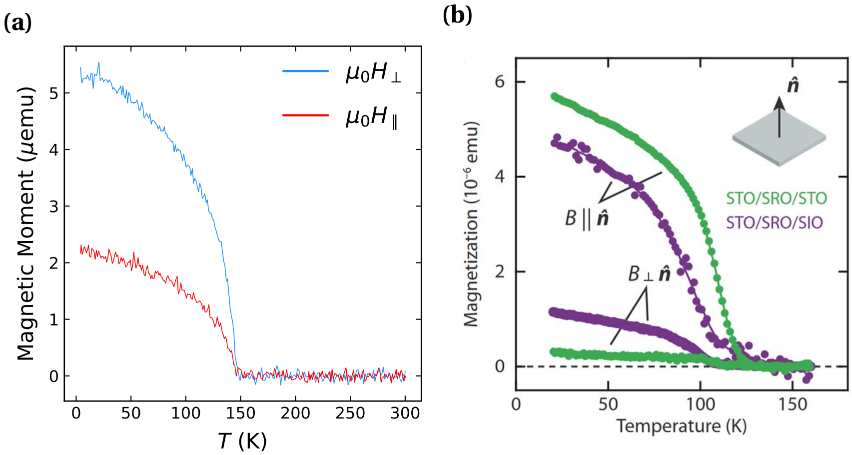

Figure 2.11: (a) SQUID measurements of Sample B performed with a 5mT external magnetic field applied in-plane and out-of-plane. (b) SQUID measurements performed on an STO(10uc)/SRO(4uc)/STO(001) heterostructure grown in our lab, figure taken from [52].μemu is a cgs unit commonly used for SQUID measurements of complex oxides for historical reasons, hence it is provided to enable easier comparison to literature. To convert to SI units, $1\text{emu} \rightarrow 1 \times 10^{-3}\text{Am}^2$.

Figure 2.11 shows the magnetization of Sample B with an external magnetic field (5 mT) applied both in and out-of-plane. It should be noted that this data was recorded via a remanence magnetization measurement. The measurement procedure was as follows: The sample was placed inside a plastic straw holder and placed in the SQUID (MPMS3) at room temperature. The sample was then cooled from 300K to 5K. A large external magnetic field was applied (a few T) to saturate the SRO sample. This external magnetic field was then reduced to 5 mT. The sample was then warmed up to room temperature at a fixed rate (0.5K per min) while the magnetic moment of the sample was measured (known as M(T) curves in the literature). These measurements were performed while the external magnetic field was applied out-of-plane of the sample. The sample was then placed on a quartz holder so that the external magnetic field pointed in-plane to the sample, where the corresponding measurements were again performed. An identical measurement procedure was performed on a clean sapphire substrate for control purposes. There were numerous reasons for using a 5 mT external magnetic field for the M(T) measurements, namely: There was a large paramagentic signal from the sample holder + substrate while applying large external magnetic fields, meanwhile the magnetic moment signal from the SRO was very small. Additionally there is always an unwanted negative residual field due to the trapped flux in the superconducting magnet of the SQUID (roughly 1 mT for MPMS3 instruments), hence an external magnetic field of 5 mT was applied to overcome this. The magnet was reset at room temperature after each measurement and the measurement procedure was identical for each measurement, hence the size and variability of the negative residual was greatly minimised.

Using $\tan^{-1}\frac{m_{ip}}{m_{oop}}$ on the data in Figure 2.11 (a) the easy axis was found to be 22° ± 2°.

The direction of the magnetic easy axis has shown to be heavily influenced by strain[53]. Compressive strain causes $M_{\perp}$ to point more out-of-plane, while tensile strain causes it to point more in-plane. This can be attributed to the fact that compressive strain from the STO substrate increases the tilting of the octahedra[54] resulting in larger orbital overlap of (d_{xz}, d_{yz}) orbitals with O_{pz} orbitals, where this overlap results in d_{xz}, d_{yz} having a larger z-component. Concordantly the SOI causes the magnetic moments to point more out-of-plane due to the increased z-character of these orbitals that have preferential occupation. In bulk form SRO has an easy axis 25° off-normal[26], meanwhile thin films of SRO grown on STO (001) substrates have been shown to have an easy axis 0-5° off-normal. Figure 2.11 (a) shows SQUID measurements performed on a 4 unit cell STO(10uc)/SRO(4uc)/STO(001) heterostructure grown in our lab. Its easy axis was found to be ~ 5° off normal. It should be noted that some assumptions are made here. First of all one assumes the sample is a single domain. This is clearly not the case as multiple domains are formed when growing in complex-oxide thin films, including SRO[55]. Each of these domains may have different easy axes directions and also interact with each other[56]. But, one can assume that an averaging over multiple domains occurs resulting in the overall unaxial magnetocrystalline easy axis observed. Secondly one assumes that the contribution of shape anisotropy is minimal. This is a reasonable assumption due to SRO's very large uniaxial anisotropy energy[26] (1.2×10^7 ergs/cm^3), a factor of 2 larger than normal metals[57], where its large uniaxial magnetocrystalline anisotropy originates from its strong spin-orbit coupling.

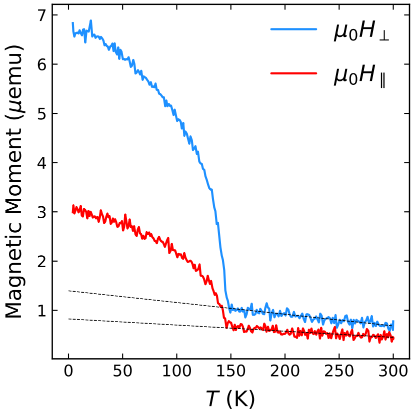

Figure 2.12: (a) SQUID measurements as described in Figure 2.11 (a) before the linear subtraction of the parametric contribution from the sample holder is performed. It should be noted that an additional paramagnetic contribution from the sapphire substrate was measured via a control experiment and subtracted to produce this plot. The dotted line represents the linear parametric contribution from the sample holder which was subtracted to then produce Figure 2.11 (a).

It should be noted that these excellent SQUID measurements and analysis of SRO membranes was performed by fellow colleague Graham Kimbell (ORCID ID: 0000-0001-9610-3589).

2.7.5. ANOMALOUS HALL EFFECT

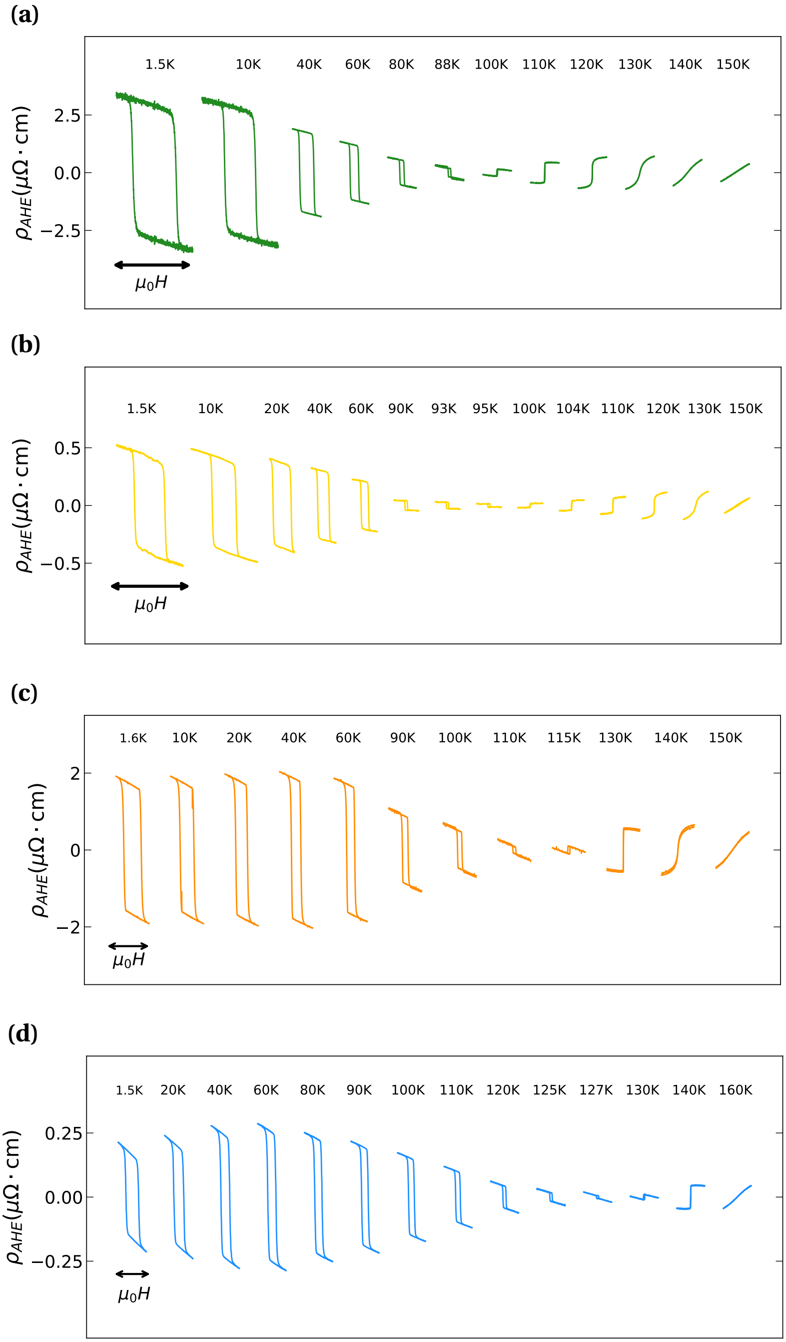

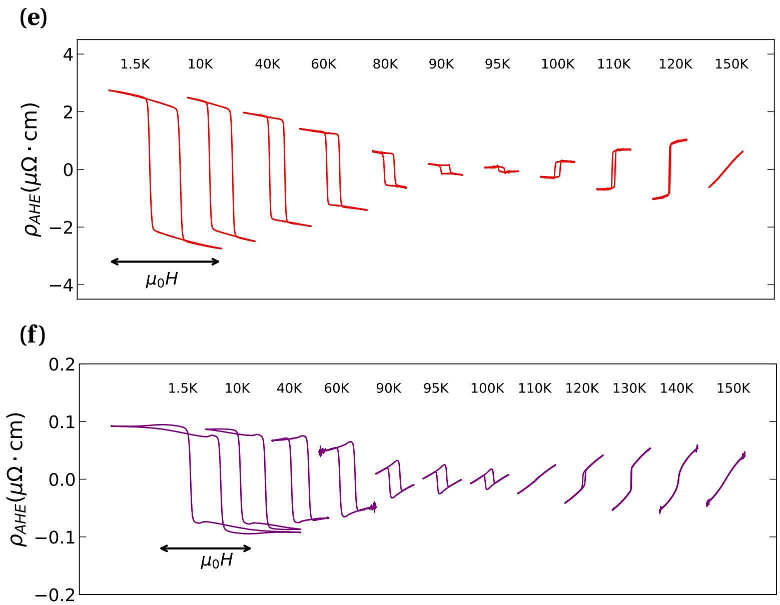

Figure 2.13: (a)-(b) Anomalous Hall resistivity of Sample C before and after exfoliation across a range of temperatures. (c)-(d) Anomalous Hall resistivity of Sample B before and after exfoliation across a range of temperatures. (e)-(f) Anomalous Hall resistivity of Sample A before and after exfoliation across a range of temperatures.

Figure 2.13 shows the anomalous resistivity (ρ^{xy}_{AHE}) hysteresis loops for Samples A,B and C both before and after exfoliation. The temperature at which the sign of the AHE switches increases after exfoliation for all three samples. ρ^{xy}_{AHE} is reduced dramatically after exfoliation. A unique characteristic of the AHE in SRO is the fact that it changes sign at a certain temperature (T_{switch})[58]. This is attributed to the Berry curvature contribution to the intrinsic AHE, where the Fermi level crosses a band at a certain temperature which has a Berry Curvature of the opposite sign[29]. We observed an increase of T_{switch} after exfoliation. This could be due to due to the increased overlap of the $\text{Ru}_{4\text{d}}$-$\text{O}_{2\text{p}}$ orbitals, resulting in a larger thermal energy required to facilitate the crossing of itinerant electrons from one band to another. There is a large decrease of ρ_{AHE} after exfoliation. Based on equation 2.1, one could attribute this to the drop in ρ_{xx}. But this explanation is incomplete as ρ_{xx} increases after exfoliation for sample A while a large drop in ρ_{AHE} is still observed (Figure 2.14). Thus the drop in ρ_{AHE} could instead be attributed to a decrease in $M_{\perp}$ due to a release of the compressive strain via exfoliation.

Figure 2.14 shows the AHE loops for each sample at 1.5K before and after exfoliation. Figure 2.14 (a)-(c) highlights the drop in magnitude after exfoliation. Figure 2.14 (d)-(f) are the plots on separate y-axes to show the loop similarities. Figure 2.14 (f) highlights how there is an extra transverse resistivity component in the exfoliated AHE loop. Linear fits of the high field regime (5T < x < 10T) were performed and are shown in Figure 2.15. Note, only the fits for the 6uc sample are shown as the measurements only went up to 5T for Sample A and Sample B. The fits highlight the preservation of linear ρ_{AHE} thus

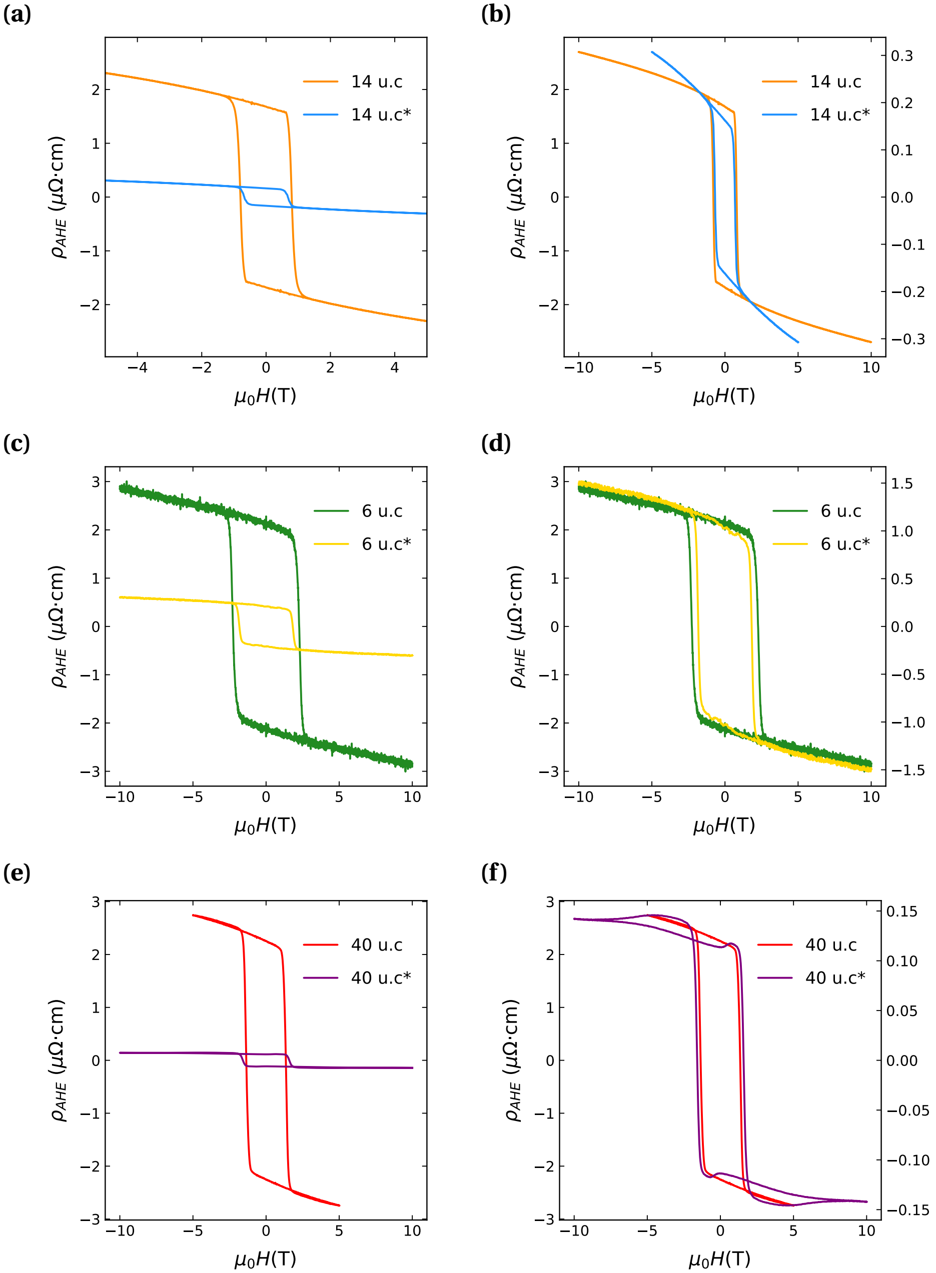

Figure 2.14: (a),(c),(e)Full AHE loop of samples B,C,A at 1.5K before and after exfoliation. (b),(d),(f) Separate y axes

implying no overlap of additional bands at the Fermi level.

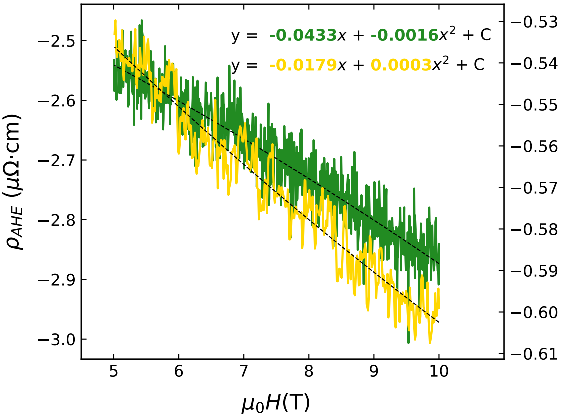

Figure 2.15: Fit of high field regime of 6uc AHE loops at 1.5K. The left y-axis is for the sample before exfoliation, the right y-axis is for the sample after exfoliation.

2.7.6. MAGNETORESISTANCE

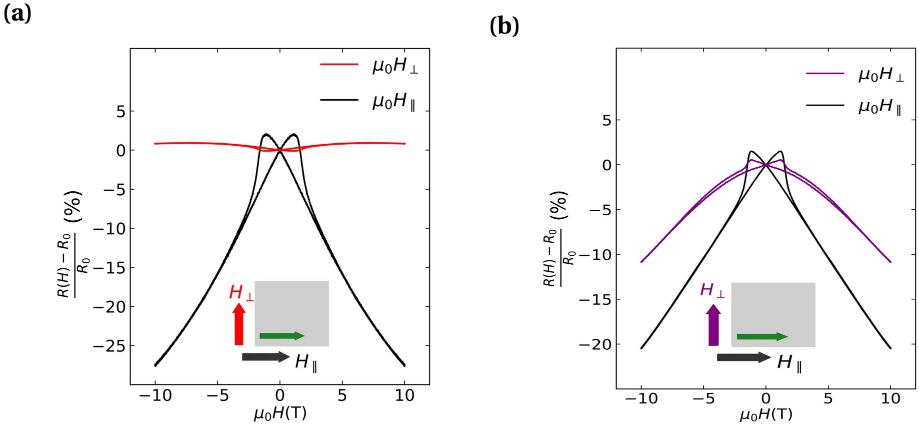

The in-plane magnetoresistance (MR) for each sample before and after exfoliation is shown in Figure 2.17. A reduction in coercivity is observed for all three samples after exfoliation (Sample A: 1.25T → 1.2T for μ_0H$_\parallel$, 1.35T → 1.2T for μ_0H$_\perp$. Sample B: 1T → 0.73T for μ_0H$_\parallel$, 1T → 0.62T for μ_0H$_\perp$. Sample C: 1.5T → 1.2T for μ_0H$_\parallel$, 1.8T → 1.6T for μ_0H$_\perp$). This indicates that the magnetization points more in-plane after the strain release. The MR curve for the applied in-plane magnetic field perpendicular to the electric current has a continuous negative slope after exfoliation.

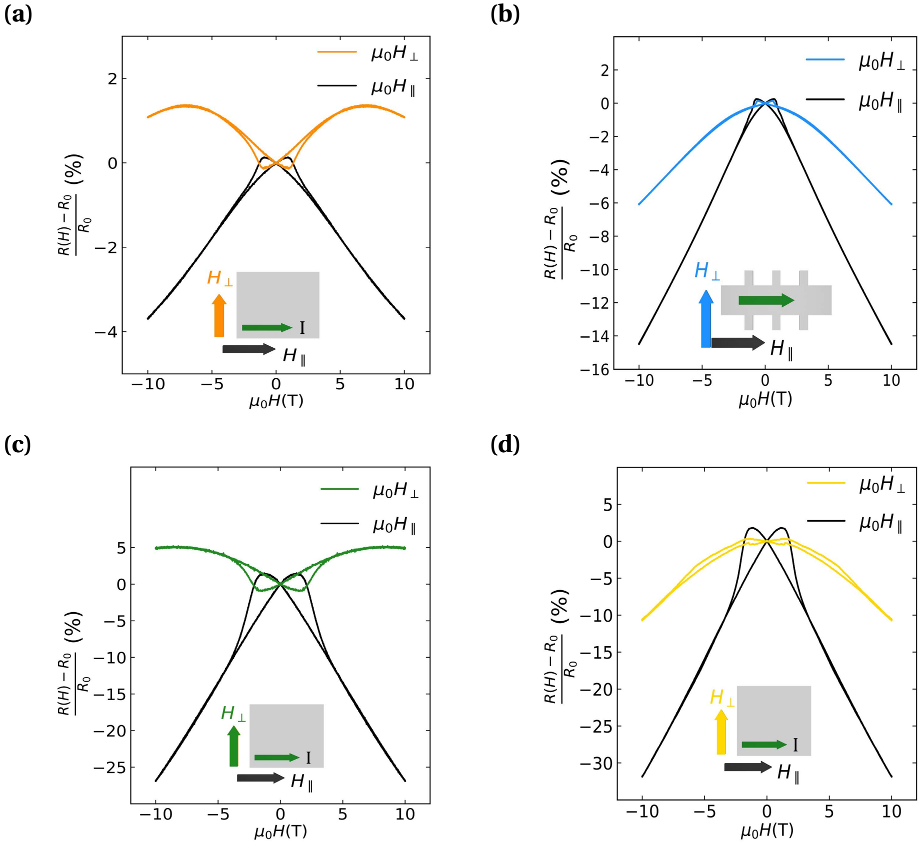

Figure 2.17: (a),(c),(d) The magnetoresistance of samples A,B,C before exfoliation, with electric current applied parallel and perpendicular to an in-plane external magnetic field. (b),(d),(f) The corresponding magnetoresistance of samples A,B,C after exfoliation

Figure 2.17 provides possible evidence for tilting Weyl cones in SRO via exfoliation. To explain further: Weyl points are classified by two types, type I and type II, which differ based on the degree of tilting of the Weyl cones (Figure 2.18). This tilting (R) is defined in terms of the Fermi velocity (v_F):

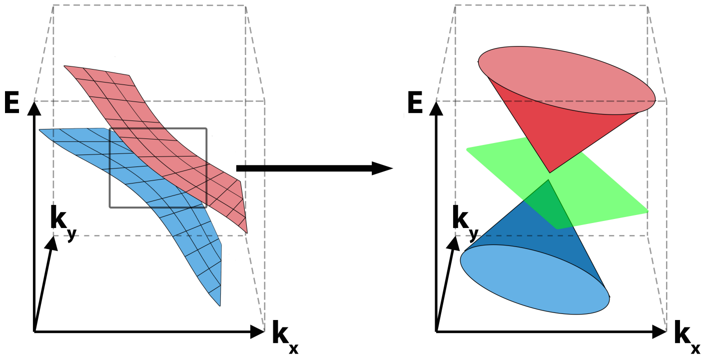

Figure 2.18: Tilted Weyl points. Left: Titled band anti-crossing. Right: Zoomed-in section showing the tilted Weyl point with the green plane representing the degree of tilt.

$$R = \frac{C_s}{v_F} \tag{2.3}$$

Where C_s is the velocity of the electrons in the direction of the tilt vector. $|R| < 1$ represents type-I Weyl points while $|R| > 1$ represent type-II. While Bloch electrons traversing a closed loop around the Weyl points experience the effects of Berry curvature, in some cases the orbital magnetic moment also needs to be taken into account. This orbital magnetic moment (not to be confused with the atomic orbital magnetic moment) originates from the self-rotation of the Bloch electrons as well as their center-of-mass motion[8]. The coupling between the applied current, the applied magnetic field and the Weyl cone tilting, while including this orbital magnetic moment, describes a number of topological phenomena seen in other materials such as $\mathrm{WTe_2}$[59] and LaAlGe[60].

Consider Figure 2.17(c), which displays the in-plane magnetoresistance curves of sample B before exfoliation. The slope of the in-plane magnetoresistance when the applied magnetic field is parallel to the applied current ($\rho_\parallel$) is negative for all values of $\mu H(T)$. Meanwhile the slope of the in-plane magnetoresistance when the applied magnetic field is perpendicular to the applied current ($\rho_\perp$) is positive when $|\mu H(T)| < 7T$. As $|\mu H(T)|$ is increased beyond this value this slope changes from positive to negative. For Figure 2.17(d), which displays the same measurements performed on the sample after exfoliation, the slopes of both $\rho_\parallel$ and $\rho_\perp$ are negative. These trends are seen across all samples measured and hence do not depend on sample thickness. The negative slopes of $\rho_\parallel$ for both before and after exfoliation are the result of the chiral anomaly[61]. Meanwhile $\rho_\perp$ is more dependant on the tilt vector and the inclusion of the orbital magnetic moment. The inclusion of the orbital magnetic moment in the calculation of the magnetoconductivity matrix of tilted Weyl nodes leads to important changes of $\rho_\perp$[62]. One such change is that the additional coupling of the orbital magnetic moment leads to positive values of $\rho_\perp$ at low R values, where $\rho_\perp$ scales via (2-8R^2). As R is increased there is a critical value of R (~ 0.5) where $\rho_\perp$ changes sign from positive to negative. Hence one possible scenario is that after exfoliation the Fermi velocity decreases due to the sample undergoing strain release, aka. the compressive strain is greatly reduced[63]. To elaborate further: This phenomena is two-fold. The strain release affects the separation in momentum space between Weyl nodes of opposite chirality and, perhaps more importantly, it changes the Fermi velocity by an amount proportional to the strain strength. This decrease in Fermi velocity then in turn increases R which leads to the negative slope of $\rho_\perp$ seen in Figure 2.17(d). This is supported by the fact that all three samples experience a reduction in compressive strain, revert back to almost identical strain values, and see a negative slope of $\rho_\perp$ in exfoliated form. But, it should be noted that there are assumptions that one makes when drawing this conclusion. Firstly the Berry Curvature in this system is described by semiclassical Boltzmann formalism, which works best under relatively small magnetic fields, specifically $\hbar\omega_C << \mu$ where ω_C is the cyclotron frequency and μ is the chemical potential[64]. This is difficult to ascertain for SRO due to the difficulties in calculating its Fermi velocities and chemical potential. Secondly the tilt vector is relatively unaffected by the applied magnetic field. This is reasonable as the tilt vector solely depends on the material's bandstructure which, in SRO, has a strong magnetic anisotropy. Thirdly it is assumed that Weyl node pinning due to crystal symmetries is minimal in this system. This is due to SRO having a low orthorhombic symmetry as well as a relatively high degree of disorder, where this disorder is presumed to originate from defects. Lastly it is presumed that $R < 1$.

2.8. CONCLUSIONS

Ultra-thin, metallic, strain-free $SrRuO_3$ membranes of different thicknesses were created via water-exfoliation of a sacrificial layer, $Sr_3Al_2O_6$. Their structural parameters were investigated, showing that there is a release of compressive strain of the $SrRuO_3$ films after exfoliation. Transport measurements show an increase of the Curie temperature after exfoliation, highlighting the increased stability of the ferromagnetic phase due to the release of strain. Magnetotransport measurements display a large decrease in the anomalous hall resistivity after exfoliation for each thickness, which can be attributed to the strain release causing the magnetic easy axis to point more in-plane. Additionally these measurements provide possible evidence for tilted Weyl cones due to a large reduction of the slope of the in-plane magnetoresistance, specifically when the applied magnetic field is perpendicular to the applied current. These flexible, itinerant ferromagnetic membranes provide a suitable platform to investigate complex phenomena such as the anomalous hall effect, while highlighting the significant influence exfoliation has on the material's structural, electronic and magnetic properties.

2.9. APPENDIX

2.9.1. ANISOTROPIC MAGNETORESISTANCE

Anisotropic Magnetoresistance (AMR) is a phenomenon that has been utilised many times to explain the magnetoresistance behaviour of SRO in the past[65, 66, 67, 68]. But, there are reasons why it may not be fully applicable to the phenomenon observed in Figure 2.17. Starting with the background:

The two-channel model for magnetoresistance in metals is based on an electron scattering mechanism first proposed by Mott in 1936[69, 70] which was expanded further to the concept of 'two channels' by Fert[71]. This model describes electrical conduction (via scattering between s and d bands) occurring within two individual channels for charge carriers (electrons say) with one channel consisting of spin-up electrons and one channel for spin-down electrons. The resistivity of each spin-channel can be represented by:

$$R^S_{tot} = R^S_0 + R^S \tag{2.4}$$

Where R^S_0 describes scattering via impurities, S is the spin (spin-up or spin-down) and R^S is spin-dependent scattering. Specifically, R^S describes the scattering of electrons from the s-band to the d-band. Most importantly, R^S is proportional to the number of empty d-states available for the s→ d scattering process to occur. The link to magnetoresistance is that by changing the direction of magnetisation, you can change the number of empty d-states available for conduction[72]. The relation between this magnetoresistance (known as anisotropic magnetoresistance) and an applied magnetic field for a positively spin-polarised ferromagnet can be seen in Figure 2.19. The magnetoresistance increases when the applied magnetic field is applied parallel to the direction of the current 2.19 (a), while the magnetoresistance decreases when the applied magnetic field is applied perpendicular 2.19(b). But, for SRO it is hypothesised that the opposite occurs because it is negatively spin-polarised, in that its itinerant electrons have an opposite spin to the spins of the itinerant electrons responsible for its ferromagnetism[73, 74].

With this, one can explain the magnetoresistance in 2.17 (a). In 2.17 (a) the sample is experiencing compressive strain, hence its magnetisation is almost fully out-of-plane (Figure 2.11) (a). When the external in-plane magnetic field is applied perpendicular to the direction of the current ($\mu_0 H_\perp$), the component of the magnetisation in-plane becomes larger, and is perpendicular to the direction of the current. Hence the magnetoresistance increases. When the SRO magnetisation fully saturates, aka. reaches its 'hard axis' ($> 7T$ in SRO[75]) the magnetoresistance starts to drop. Meanwhile when the external magnetic field is applied parallel to the current ($\mu_0 H_\parallel$), a larger component of the magnetisation is in-plane and parallel to the direction of the current. Hence the magnetoresistance decreases. One reason why both the $\mu_0 H_\perp$ and $\mu_0 H_\parallel$ magnetoresistance continue to decrease after saturation can be due to spin-dependent impurity scattering[76]. This is where electron scattering can occur via impurities, but the probability for scattering decreases when the spins are preserved. Hence when the spins of the impurities become more aligned due to an increasing external magnetic field, a reduction

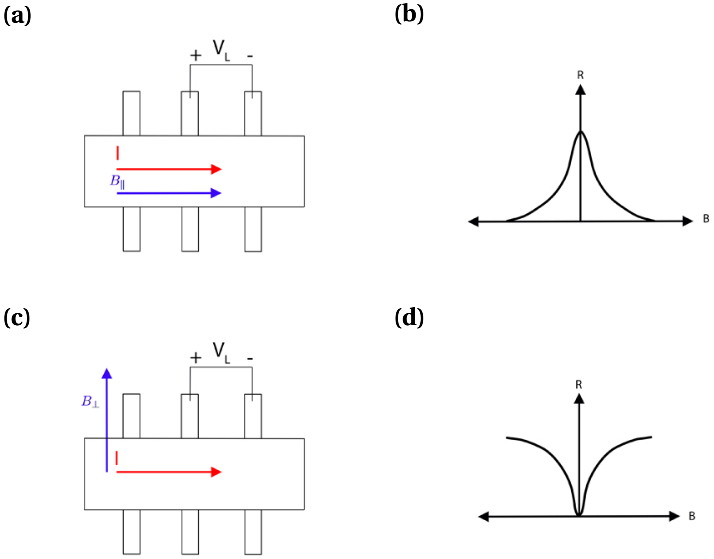

Figure 2.19: Representation of anisotropic magnetoresistance in a positively spin-polarized ferromagnet (a) External magnetic field applied parallel to the direction of the electric current (b) Resistance vs applied external magnetic field with the configuration shown in (a). (c) External magnetic field applied perpendicular to the direction of the electric current (d) Resistance vs applied external magnetic field with the configuration shown in (c)

in scattering occurs hence the magnetoresistance decreases.

But, there are numerous problems when one tries to apply this theory to the phenomenon observed in Figure 2.17 (b). The sample is now strain-free, hence its magnetisation now points more in-plane (Figure 2.1). While this larger in-plane component (due to the easy axis being $\approx 22^\circ$ off normal) will lead to a reduction in the observed in-plane magnetoresistance, it should not negate it entirely as is seen for the $\mu_0 H_\perp$ curve in 2.17 (b). Secondly s→ d scattering should be minimal for SRO as its valence electrons lie within the t_{2g} orbitals in the 4d band. Whether Mott's scattering mechanism and two spin channels can apply solely to scattering between bands consisting of t_{2g}/e_{2g} orbitals is unclear. Lastly, evidence for a two-channel model should be seen in the anomalous Hall loops (Figure 2.14), where significant non-linearity of the curves should occur after hysteresis, instead the curves are mostly linear (apart from perhaps an additional component occurring in Figure 2.14 (e) and (f)). With a larger sweep range of the applied magnetic field perhaps this linearity could be further justified but unfortunately the largest sweeps performed were ±10T.

3

FABRICATION AND SHAPE CONTROL OF FREESTANDING COMPLEX OXIDE MEMBRANES

A robust, adaptable fabrication method is introduced allowing the reliable creation of high-quality, crack-free, crystalline freestanding complex oxide membranes. This process allows the geometry of the membranes to be fully customisable while also greatly increasing the number of complex oxides eligible to be produced as freestanding membranes.

3.1. INTRODUCTION

Freestanding complex oxide membranes are a relatively new field with a sparse collection of established literature outlining fabrication methods for creating high-quality complex oxide membranes. The purpose of this work was to create a robust, reproducible fabrication process to grow, exfoliate, and stamp freestanding complex oxide membranes of any desired shape and size. There are a number of hurdles to overcome when fabricating freestanding complex oxide membranes such as lattice mismatch, shape determination, and film protection. This newly developed method directly addresses these problems and helps open up freestanding complex oxide membranes to a plethora of well-established, and also new, measurement techniques and investigations.

3.2. CALCIUM-DOPED STRONTIUM ALUMINATE

$Sr_3Al_2O_6$ (SAO) has been described in Chapter 2 as a method for creating freestanding complex oxide membranes by acting as a sacrificial layer. While SAO has been utilised for this purpose in a number of works[20] one problem it has is a phenomenon known as lattice mismatch[77]. It has been shown that having a large mismatch between the SAO lattice parameter and the desired complex oxide grown on top of it facilitates strain release in the form of cracks after exfoliation. Further, it has been shown that the degree of crack formation is proportional to the degree of lattice mismatch[2]. SAO has a relatively large lattice constant (~ 3.99Å) which severely limits the amount of complex oxides that can be grown on it without having a significant lattice mismatch. If the SAO lattice parameter could be tuned, it could open up a wide array of large, crack-free freestanding complex oxides that could be created. One method to tuning the SAO lattice parameter is doping SAO with calcium.

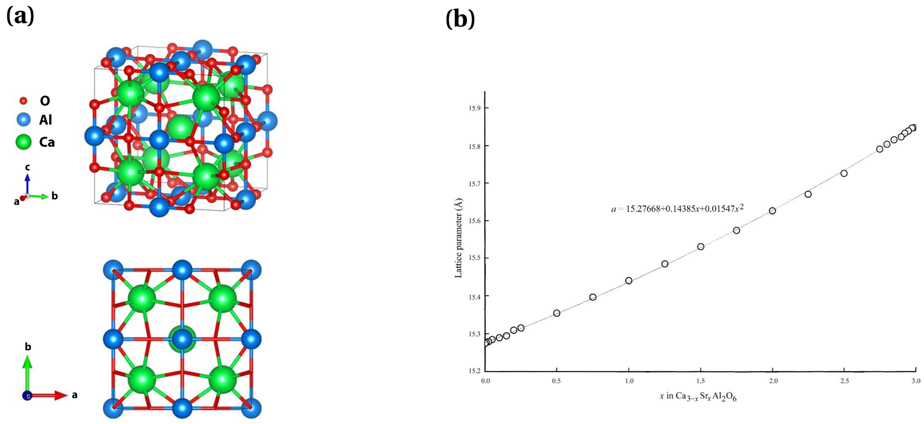

Figure 3.1: (a) (Upper) Pseudocubic unit cell of Ca3Al2O6. (Lower) Psuedocubic unit cell viewed along z-axis (b) Change in lattice parameter of Ca-SAO with Sr doping, taken from [23]. The equation of the line can be used to determine the lattice parameter *a* from the degree of doping *x*.

Calcium-doped strontium aluminate $Ca_{3-x}Sr_xAl_2O_6$ (Ca-SAO) has a very similar lattice structure to SAO[78] ($Ca_3SrAl_2O_6$ shown in Figure 3.1 (a)) where strontium atoms are replaced with calcium. Ca-SAO has the same space group as SAO of $Pa\overline{3}$. Its pseudocubic unit cell also has an identical structure to SAO's. The percentage of strontium atoms being replaced with calcium depends on the level of doping. Calcium atoms are smaller than strontium atoms (calcium atomic mass - 40.074u, strontium atomic mass - 87.62u, calcium atomic radius - 194pm, strontium atomic radius 219pm) and replacing strontium atoms with calcium decreases its pseudocubic lattice parameter. One key aspect is that the reduction of Ca-SAO's lattice parameter can be controlled by the degree of calcium doping[23]. The lattice parameter has been shown to be linearly proportional to the degree of calcium doping, providing a range of lattice parameters from 3.81Å to 3.99Å. Hence, by varying the concentration of calcium in Ca-SAO, the lattice mismatch problem can be greatly reduced. This was particularly relevant when attempting to grow sacrificial layers for $NdNiO_3$ in this work, as it has a pseudocubic lattice parameter of $c_{NNO} \approx 3.81$Å. A high degree of calcium doping is required $Ca_{2.5}Sr_{0.5}Al_2O_6$ (Ca2.5-SAO) to provide adequate lattice matching to $NdNiO_3$ (0.5% strain). But, doping SAO with calcium creates additional problems. Firstly Ca-SAO is less water-soluble than SAO. Increasing the degree of calcium doping dramatically reduces Ca-SAO's water solubility[79]. Calcium is more electronegative than strontium, which leads to an increase in the high coordination number(X(5)-O, X(6)-O) bond strengths as as well as shorter bond distances, where X represents the coordinate site of Sr/Ca atoms. This increases the protonation activation energy of these high-coordinate X-O bonds. Secondly it proved difficult to epitaxially grow Ca2.5-SAO directly on $SrTiO_3$ (001) substrates, where poor-quality amorphous films formed when using the same growth conditions as SAO (Figure 3.2 (a)). The growth conditions can be found in Chapter 4, Table 4.2. Higher quality RHEEDs were observed for Ca2.5-SAO when grown at much higher temperatures (850-900°C) (Figure 3.13 (b)) but the films showed no signs of exfoliation after being immersed in 70°C de-ionised water for 1 week (Figure 3.14).

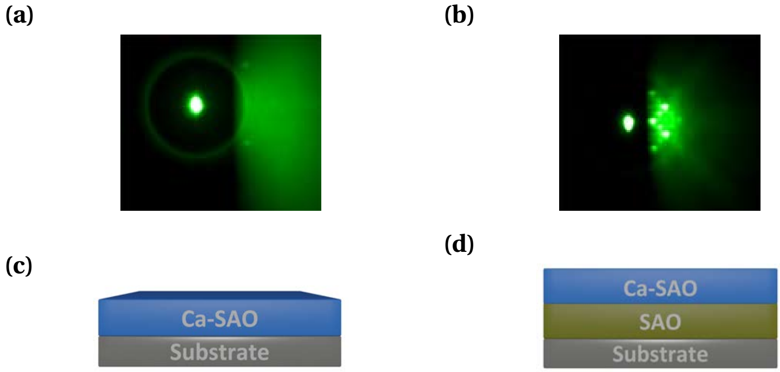

Figure 3.2: Highlighting the improved growth of Ca2.5-SAO by growing on SAO/STO(001) rather than the STO(001) substrate directly. (a) Ca2.5-SAO grown directly on STO(001) substrate (b) Ca2.5-SAO grown on SAO/STO(001 (c) Heterostructure for (a) with the substrate being STO(001) (d) Heterostructure for (b) with the substrate being STO(001)

The heterostructure shown in Figure 3.2 (d) was created to rectify these problems. The thin (15uc) SAO layer allows the Ca2.5-SAO layer to be grown on top with lower temperatures and fluences, identical to the parameters used to grow the SAO layer (Table 4.2). The Ca2.5-SAO layer is thick (80uc) allowing it to strain-relax to its bulk value (3.83 Å). The desired thin film, $NdNiO_3$, is then closely lattice-matched to the Ca2.5-SAO (0.5% strain). The SAO layer also increases the etching rate of the sacrificial layers as it dissolves quicker than the Ca2.5-SAO causing the substrate to drop and exposing a vastly larger surface area of Ca2.5-SAO to water resulting in a much faster etch rate. The addition of the SAO layer shortened the exfoliation time of our samples from 3 days to 6 hours.

3.2.1. REFLECTION HIGH ENERGY ELECTRON DIFFRACTION

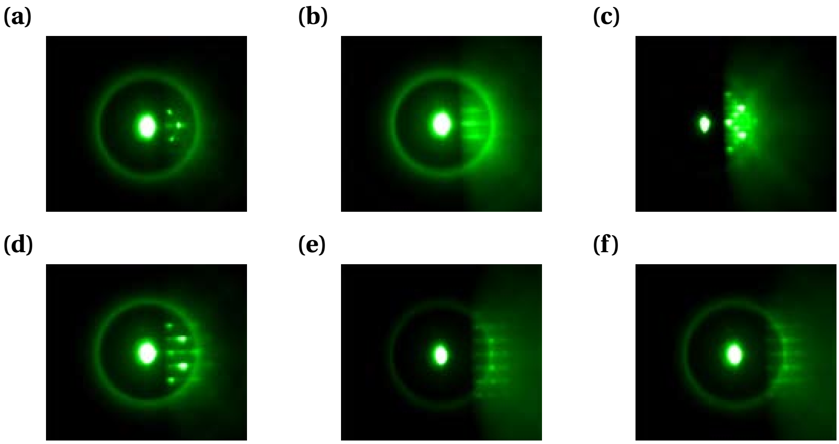

Figure 3.3: RHEED patterns for each layer of heterostructure shown in Figure 3.4 (b). (a) $SrTiO_3$ substrate (b) SAO (c) Ca2.5-SAO (d) $SrTiO_3$ capping bottom layer (e) $NdNiO_3$ (f) $SrTiO_3$ capping top layer

Figure 3.3 shows the reflection high energy electron diffraction (RHEED) patterns of each thin film layer *in-situ* as the heterostructure is epitaxially grown. Each layer shows clear diffraction patterns highlighting surface crystallinity. The intensity, size and nature of the patterns can indicate the surface topology[80]. The diffraction pattern of a smooth, flat, monodomain surface produces sharp spots. This is best represented by the RHEED of the STO substrate in Figure 3.3 (a). Figure 3.3 (b) shows the RHEED of the SAO film. Large stripes are indicative of a flat surface with small domains. For the Ca2.5-SAO and bottom STO capping RHEEDs Figure 3.3 (c)-(d) the modulated streaks indicate a rougher multi-stepped surface with small domains. Lastly the NNO and upper STO capping show a reduction of the multi-stepped topology and a return to a flatter surface with small domains via stripes. Figure 3.4 displays the RHEED oscillations recorded during the growth of the SAO layer, with an average of 30 pulses per unit cell. The clear oscillations indicate layer-by-layer growth[81]. The growth conditions can be found in Table 4.2. Figure 3.5 (a) displays the RHEED oscillations found for the Ca2.5-SAO layer

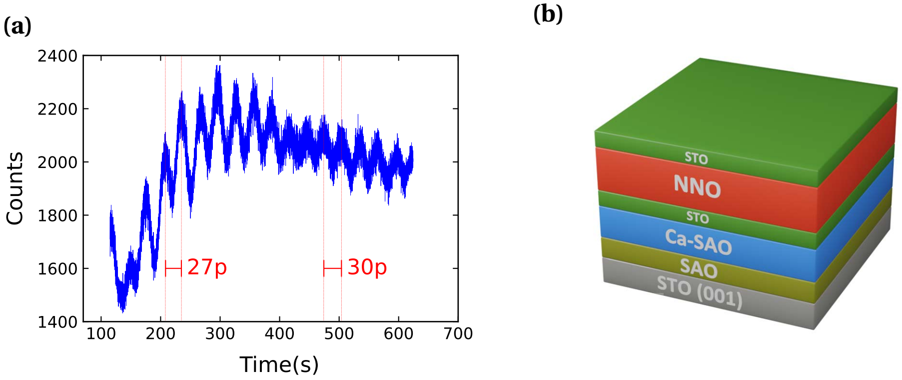

Figure 3.4: (a) SAO RHEED with number of pulses per oscillation. (b) Heterostructure grown in Figure 3.3

grown on the SAO layer. The diffraction peak intensity drops for the first ~ 200 pulses with a smaller number of pulses per unit cell ~ 20p/u.c (Figure 3.5 (b)). The diffraction peak intensity then grows dramatically and a larger number of pulses per unit cell (~ 40p/u.c) is found (Figure 3.5 (c)). This RHEED pattern behaviour was found across all SAO/Ca2.5-SAO samples grown. One explanation is that ~ 200 pulses are needed to stabilise the heteroepitaxial layers, following which layer-by-layer homoepitaxial growth can occur. While the oscillations are less prominent compared to SAO, they still indicate that layer-by-layer growth also occurs for Ca2.5-SAO.

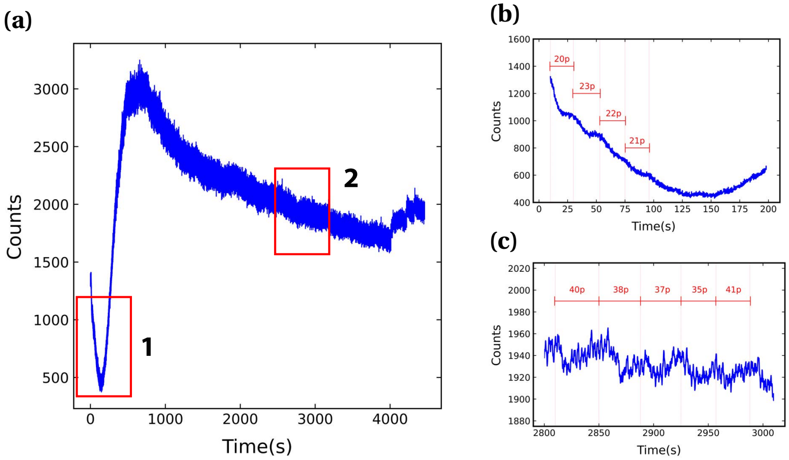

Figure 3.5: (a) Ca2.5-SAO RHEED. Depositions were performed at a rate of 1Hz with a total of 4000 pulses. The rectangles 1 and 2 highlight the areas magnified in (b) and (c) respectively. The increase in intensity after 4000 seconds represents the surface reconstruction immediately after the growth (4000 pulses) is finished.

After depositing an STO capping layer (8 u.c) the $NdNiO_3$ film can then be grown on top, with an example of the resulting RHEED shown in Figure 3.3 (d). No oscillations could be recorded due to the high O_2 pressures used for the growth of the $NdNiO_3$ layer. An additional $SrTiO_3$ capping layer of 8 u.c (Figure 3.3 (e)) was deposited on top of the $NdNiO_3$ layer to help protect it during the ensuing fabrication process. It should be noted that for the specific $NdNiO_3$ membranes on which the electronic transport measurements were performed in Chapter 3, the $NdNiO_3$ and top STO capping layers were grown via off-axis sputtering due to a lab move resulting in the unavailability of the PLD, thus no RHEED is available for those layers in those particular samples.

3.3. Shape Control

With the lattice mismatch problem minimised the next steps were to control the shapes of the membranes produced. While the method described in Chapter 2 (Section 2.3) creates freestanding complex oxide membranes, it only produces membranes of random shapes and sizes. Membranes with select geometries are a requirement for numerous experiments, for example Hall bars can be utilised for accurate resistivity measurements[82, 83]. Hence a fabrication method involving e-beam lithography and etching steps was employed. The full process is shown in Figure 3.6.

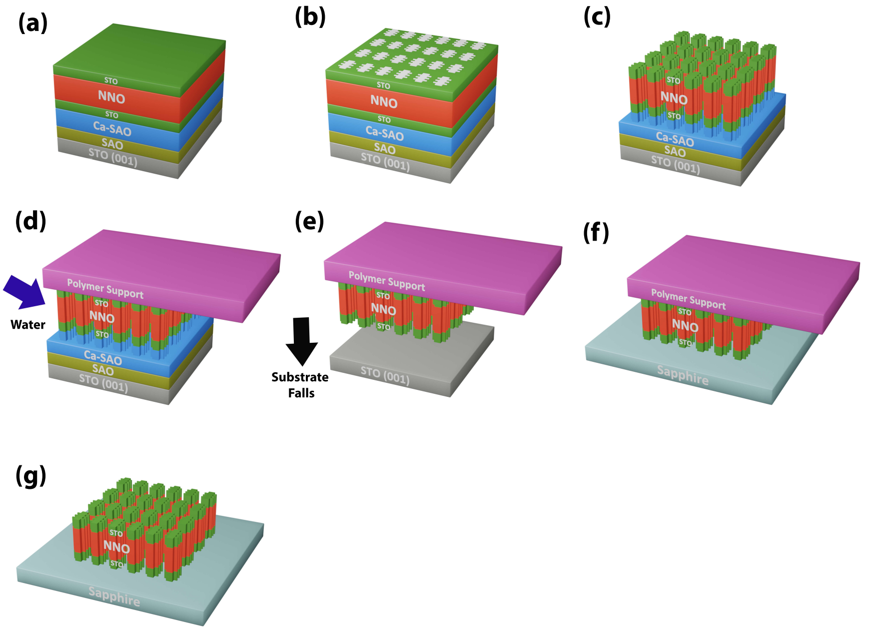

Figure 3.6: Outline of fabrication process described in this chapter. (a) Grown heterostructure (b) Array of Hall bars with each Hall bar having a layer photoresist on top. (c) Resulting Hall bars after Ar milling and top layer resist removal (d) Placement of PDMS stamp and immersion of entire structure in de-ionised water (e) Exfoliation of sacrificial layers resulting in the substrate falling (f) Stamping exfoliated Hall bars onto sapphire substrate (g) Removal of PDMS stamp with stamped freestanding Hall bars on sapphire substrate.

3.3.1. PATTERNING THE ARRAY

A 4.5 x 4.5mm array of Hall bars was patterned on top of the heterostructure via ebeam resist. Hall bars of size 40μm x 10μm were chosen so that they are large enough to have an ideal geometry[84] but small enough to reduce the chance of them having cracks due to dislocations, buckling, and strain release via exfoliation. Each Hall bar was separated from one another by 100μm to allow adequate space for the deposition of metal contacts at a later stage. The lithography process to create the array was as follows:

- Clean the heterostructure surface via qtip, using acetone and IPA.
- Spincoat PMMA 495 A4, 4000rpm, 1 minute. Place on hot plate at 180°C for 2 minutes. Produces 180nm thick layer.
- Spincoat PMMA 950 A8, 4000rpm, 1 minute. Place on hot plate at 180°C for 20 - 40 minutes. Produces 600nm thick layer.
- Deposit 20nm Au film on top of spincoated PMMA via sputtering.
- Expose via e-beam (ebeam Raith EBPG-5000+ with parameters 100 kV, 300μ aperture, 43nm spot size, beam current 63nA including proximity correction).
- Place sample in Au etchant (potassium iodide) for a few seconds to remove the top Au layer. Rinse in de-ionised water.
- Develop the exposed resist by immersing the sample in MIBK:IPA (Ratio 1:3) for 1 minute. Rinse in IPA for 30 seconds.

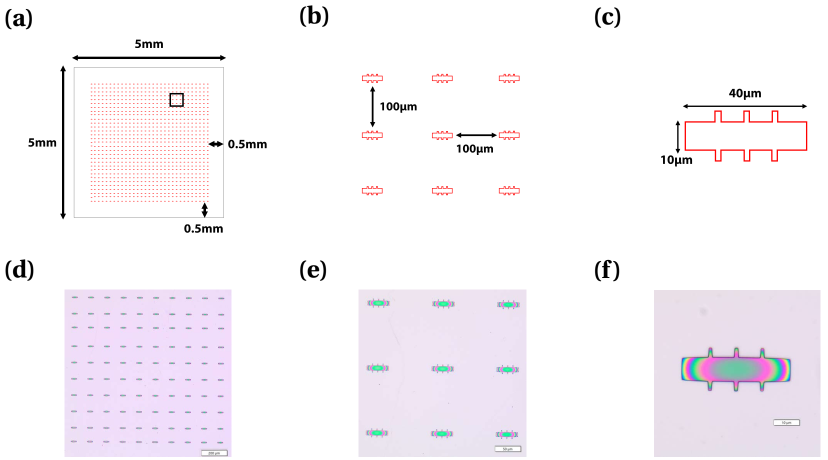

Figure 3.7: (a) CAD file of 4.5 x 4.5mm array of Hall bars with 0.5mm border on a 5x5mm substrate. The black rectangle is the area shown in (b) (b) Zoomed in area of (a) showing distances between separate Hall bars (c) Dimensions of individual Hall bar (d) Array after development (e) zoomed in (f) Individual hall bar

The reasons for these steps are numerous. Firstly PMMA (a positive resist) is used as the developers for negative resists are basic and were found to dissolve the NNO layer.

Note one drawback of using a positive resist for fabricating the array is that the areas around the Hall bars are exposed (while the areas that form the Hall bar shape are not) which results in longer writing times. Secondly an Au layer is required as while NNO is metallic, a material with greater metallicity was required to avoid charging issues when exposing the resist (Subsection 3.5.3). Lastly, long baking times for the PMMA 950 A8 were used as it was discovered that not baking the PMMA 950A8 for long enough (and/or not using a thick enough Au layer) would result in thin lines being formed at the edges of the writefields, as well as charging lines at the edges of patterns (Subsection 3.5.3).

3.3.2. ETCHING

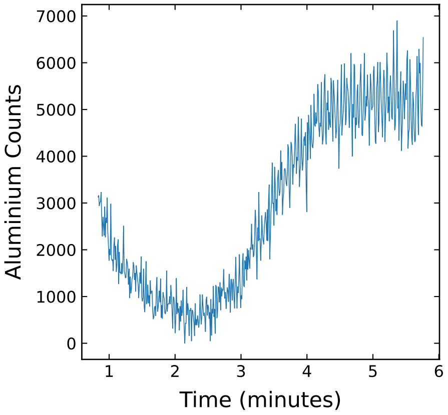

Figure 3.8: Counts of Aluminium during argon etching. Etching of the sacrificial layer begins around the 3 minute mark. The etch was stopped shortly after the aluminium counts stabilised.

Utilising argon milling (via a SCIA Mill 150) the exposed heterostructure is then etched. The SCIA Mill 150 includes a mass spectrometer which can be used to determine *in-situ* the layer currently being etched. The etching was deliberately stopped when the sacrificial layers were reached. This is so that a 0.5mm border of sacrificial layers will be directly exposed to de-ionised water in the exfoliation step. This is to account for any dirt or residues that might be on the vertical edges of the substrate which might block the nanometer-thick sacrificial layers from being exposed to the de-ionised water. The remaining resist on top of the exposed Hall bars was then removed via q-tip with acetone and IPA.

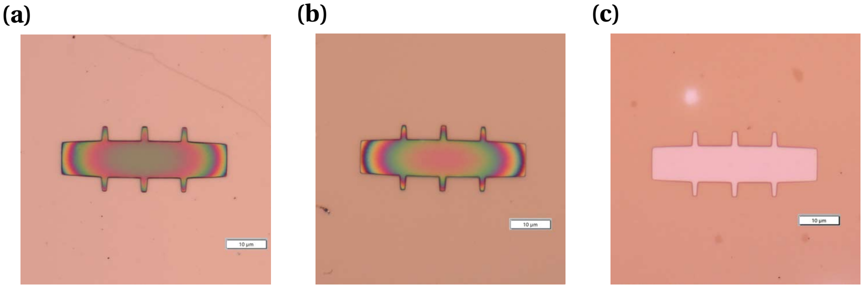

Figure 3.9: (a) Image of a Hall bar after the development step in the lithography process described in 3.3.1. The resist remains on top of the Hall bar area to protect it during the argon milling step. (b) Hall bar after argon milling via a SCIA MIll 150. Resist remains on the Hall bar, clarifying that the Hall Bar area is not etched. (c) Hall bar after the remaining resist is removed via a q-tip.

3.3.3. EXFOLIATION

A square thin film of PDMS (Gel Pak, PF-30-X4) was cut into a certain shape, allowing it to be stamped on top of the exposed Hall bars (Figure 3.10 (a)). The plastic thin film covering the PDMS was only removed on the rectangular piece. The rectangular piece was cut thin enough so that the 0.5mm etched borders are directly exposed to the de-ionised water. The PDMS film with the heterostructure attached is placed into a beaker of de-ionised water. Two dense blocks are used to keep the PDMS film & heterostructure securely under the surface of the de-ionised water while also not touching the bottom of the beaker (Figure 3.10 (b)). The de-ionised water was then heated to 60-70°C for ~ 6 hours. If the substrate had not fallen the PDMS film & heterostructure were removed from the de-ionised water and the substrate was peeled off the PDMS film. The PDMS film and attached exfoliated membranes are then dried with an N_2 gun (Figure 3.10 (c)). The desired substrate (that the membranes will be stamped onto) is cleaned with a q-tip, acetone and IPA. The desired substrate is then further cleaned via O_2 plasma (PVA Tepla 300), with a O_2 flow of 250ml and a power of 300W for 1 minute.

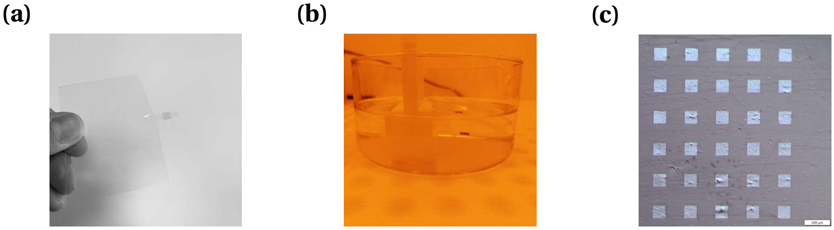

Figure 3.10: (a) Image of substrate attached to a PDMS stamp. (b) Stamp and substrate immersed in de-ionised water, using two wafter holders to ensure the substrate is securely kept under the water surface and not touching the bottom of the beaker. (c) Square $NdNiO_3$ membrane array remaining on the stamp after exfoliation

3.3.4. STAMPING

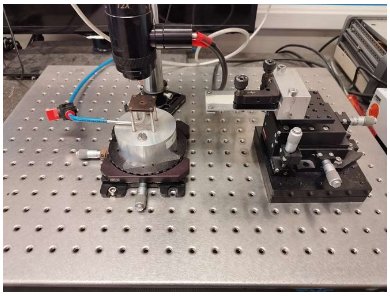

Figure 3.11: Stamping setup used to stamp exfoliated membranes from the PDMS stamp onto a desired substrate.

Figure 3.11 shows the stamping setup used to stamp the exfoliated membranes onto the desired substrate. It consists of a micromanipulator with the PDMS stamp & exfoliated membrane secured into it, a heater & vacuum stage and an overhead camera. The PDMS stamp is slowly placed on top of the substrate, the substrate is then heated to 80°C and the PDMS stamp is held in place for 1 minute. Then the PDMS stamp is slowly lifted away while the substrate remains in place due to the vacuum stage. The exfoliated membranes are now transferred onto the desired substrate.

3.3.5. ELECTRICAL CONTACTS

For the creation of electrical contacts, the substrate is pre-patterned with Au markers prior to stamping the membranes onto it. After stamping the membranes, the substrate is heated to 350°C for one hour. It was discovered that without this strong annealing, the membranes moved slightly ($\sim \mu m$) during the next spin coating process which interferes with the e-beam alignment (Subsection 3.5.4). After annealing, taking optical images and creating the e-beam CAD pattern for the electrical contacts, the sample undergoes the same fabrication process as described in Section 3.3.1. Ni(15nm)/Au(50nm) contacts were then deposited via sputtering (Alliance EVA 450). Sputtering was performed in vacuum ($< 1 \times 10^{-6}$ Torr) with no break in vacuum between the Ni and Au deposition steps. It was observed that if the vacuum was broken in between the Ni and Au depositions (moving the sample to a different sputtering machine for the Au deposition for example) large Schottky barriers were formed. This was most likely due to the sputtered Ni oxidising with air. Liftoff was performed via immersing the sample in acetone at 50°C for a few hours. The sample was then rinsed in IPA, dried and then pasted onto a chip carrier via varnish (GE 7031). The contacts were then wirebonded to the chip carrier with aluminium wire bonds.

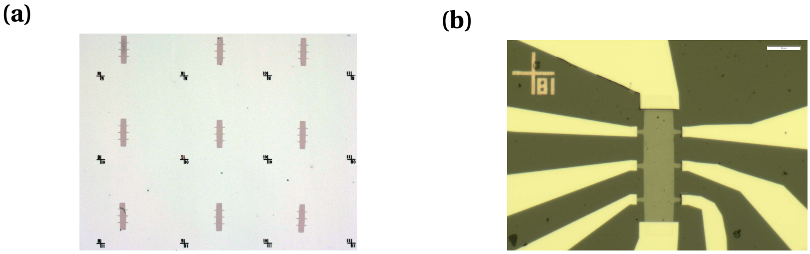

Figure 3.12: (a) Optical image of 9 stamped $NdNiO_3$ Hall bars. Pre-patterned alignment markers can be seen between each Hall bar. (b) 100x Image of freestanding NNO Hall bar with Ni/Au contacts. The number and cross in the upper left is a contacts alignment marker. The scale bar on the upper right represents a distance of 10μm

3.4. CONCLUSIONS

This chapter described a new, robust process for the fabrication of high-quality complex-oxide membranes. Emphasis was placed on shape control and the utilisation of Hall bars to enable accurate electrical resistivity measurements. This process is designed to be generic in that it can work with many different types of complex oxides, as long as an appropriate sacrificial layer is used. This process helps solve a number of issues with the fabrication of freestanding complex-oxide membranes such as exfoliation times, cracks due to strain release, and undesired membrane shapes. Systematically producing arrays of high-quality complex-oxide membranes enables their use in a multitude of fundamental experiments.

3.5. APPENDIX

3.5.1. CA2.5SAO GROWN AT HIGHER TEMPERATURES

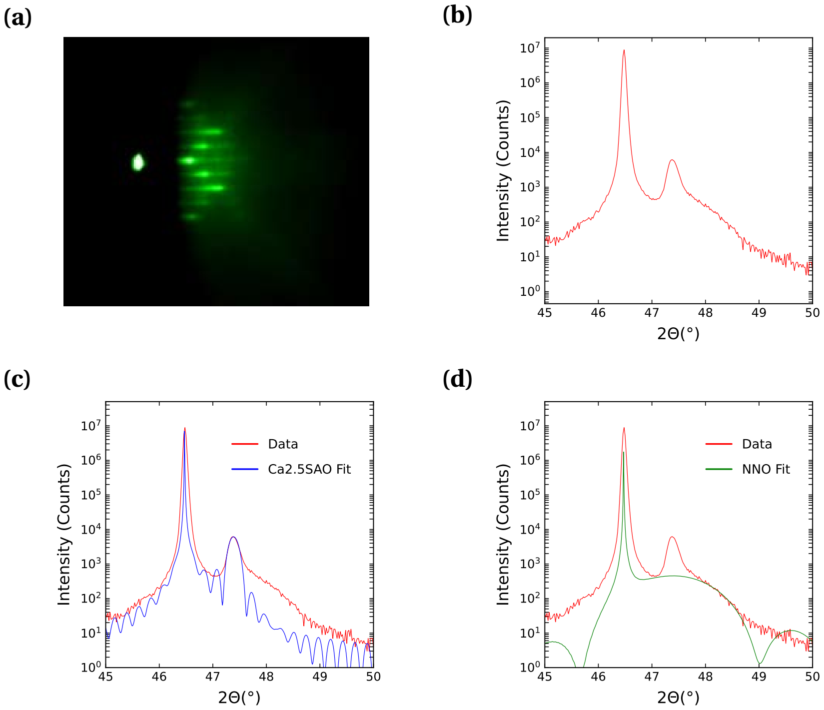

Figure 3.13: (a) Ca2.5-SAO RHEED grown at 850°C (b) XRD Spectra of NNO/STO/Ca2.5-SAO/STO(001) (c) Ca2.5-SAO fitting. $c_{\text{Ca2.5-SAO}}$ = 3.83Å, thickness 30 unit cells. (d) NNO fitting. c_{NNO} = 3.815Å, thickness 15uc.

Ca2.5-SAO was found to epitaxially grow directly on STO(001) substrates only when temperatures much higher than the conditions used in Subsection 3.2 (b) were used. Specifically, Ca2.5-SAO was found to epitaxially grow directly on STO(001) at a temperature of 850°C, compared to 700-750°C when grown on SAO. The laser fluence and pressure are identical for both cases. Figure 3.13 shows the characterisation of a Ca2.5-SAO film grown at this higher temperature. Figure 3.13 (a) shows the RHEED observed, which is similar to the RHEEDs grown at lower temperatures. Figure 3.13 (b)-(d) display and XRD spectra and fits for a STO/NNO/STO/Ca2.5-SAO/STO(001) heterostructure where the Ca2.5-SAO is grown at higher temperature. The NNO and STO layers were grown in identical conditions to Figure 3.3. Satisfactory XRD spectras were observed, with fitting producing the lattice parameters $c_{\text{Ca2.5SAO}}$ = 3.83Å, c_{NNO} = 3.815Å, with a Ca2.5-SAO layer thickness of 30uc, NNO layer thickness 15uc. No evidence of parasitic peaks was observed. But, unfortunately Ca2.5-SAO films grown at these higher temperatures proved difficult to exfoliate, shown in Figure 3.14. Whether the difficulty in exfoliating is due to the increased growth temperature, or simply that the only sacrificial layer in those heterostructures is less water soluble, the outcome is the same regardless in that the addition of an additional SAO layer greatly improved the degree and rate of exfoliation.

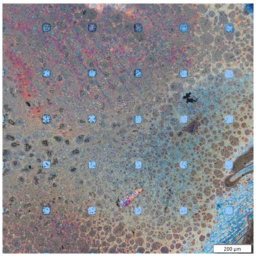

Figure 3.14: NNO heterostructure (STO/NNO/STO/Ca2.5-SAO/STO(001)) after an exfoliation attempt with the stamp peeled off. The substrate was attached to a stamp and immersed in de-ionised water at 70°C for three days. The stamp was peeled off after the exfoliation attempt. The heterostructure was patterned via the process described in Section 3.3.1 with an array consisting of 40μm squares. The squares, not exfoliated, can be clearly seen remaining on the substrate.

3.5.2. WATER-SENSITIVE MATERIALS

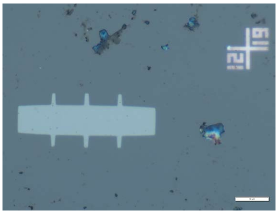

Figure 3.15: Freestanding NNO Hall bar stamped on sapphire after removal of the additional protective PMMA layer via acetone. A pre-patterned platinum alignment marker can be seen in the upper right. Polymer residues remain which proved resistant to O_2 plasma treatment as well as xylene wet etching.

The fabrication process described in Section 3.3.1 also be used for complex oxides that are sensitive to water, for example the iridates[85]. After etching the heterostructure, stopping in the middle of the sacrificial layers, and removing the leftover resist on the Hall bar areas, a polymer (such as PMMA) can then be spin-coated on the surface of the etched heterostructure. Utilising capping layers, all sides of the desired material is now protected from the de-ionised water used to exfoliate the sacrificial layers (top and bottom via the capping layers, the sides via the polymer) while the sacrificial layers can still be exposed to the de-ionised water. The same exfoliation and dry-polymer transfer technique described in Section 3.3.1 can be performed to exfoliate and stamp the etched structures. An additional step of immersing the stamped substrate in acetone is required after stamping the exfoliated membranes, to remove the polymer that protected the desired layer during the exfoliation step. But, it was observed that additional polymer residues remained on the stamped surface after removing the polymer via acetone and ipa (Figure 3.15).

3.5.3. E-BEAM PARAMETERS

The optical transparency and electrically insulating properties of STO results in difficulties when performing e-beam lithography on heterostructures grown on STO substrates. It was found that not sputtering a thick enough Au layer caused stitching errors when attempting to fabricate electrical contacts (Figure 3.16 (a)). A certain degree of reflectivity is required from the heterostructure to allow the ebeam to accurately calculate the height of the surface it will pattern. Without a large enough reflectivity, errors in the *in-situ* height calculations that the e-beam performs can lead to spurious deflections which result in stitching errors. These errors manifest as gaps in the areas one wishes to expose. The thicknesses of the thin film layers grown on the STO substrate were too low to provide a high enough average reflectivity, hence a thick (20nm) Au layer was sputtered on to rectify this. It was also found that having too thin of an Au layer (<10nm) and/or not baking the PMMA 950 A8 for long enough times (<20 minutes) resulted in unwanted charging phenomena (Figure 3.16 (b)) which leads to the patterned contacts shorting (Figure 3.16 (b)).

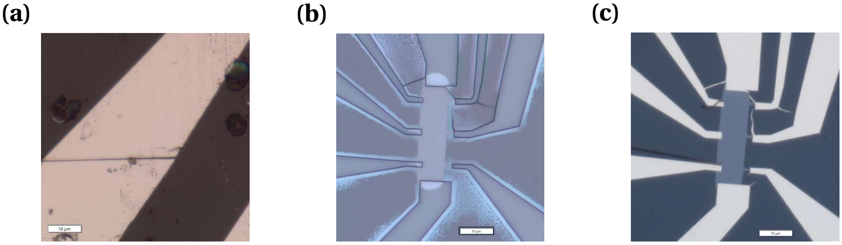

Figure 3.16: (a) Gaps in deposited electrical contacts due to stitching errors (b) Hall bar contacts after development. 8nm Au was used as a metallic layer instead of 20nm in the process described in 3.3.1. Charging lines can be seen at the end of the contacts. (c) After sputtering Ni/Au onto the Hall bar shown in (b). The contacts are shorted to each other, reducing the amounts of electrical contacts available for accurate electrical resistivity measurements.

3.5.4. REQUIRED ANNEALING

It was observed that in order to pattern electrical contacts onto stamped freestanding membranes, sufficient annealing of the membranes was required. When the membranes were not annealed, it was observed that they moved ~ μm's after the metal liftoff step of the electrical contacts. There was no indication that the membranes had moved after the e-beam exposure and resist development steps. One hypothesis is that without sufficient annealing, the membranes move slightly while being spincoated with resist before the e-beam exposure. The resist ‘holds’ the shear stress that the membranes experience due to a lack of proper adhesion to the substrate. This stress is then released after the resist is removed during the liftoff step. This release of stress causes the membranes to move slightly, breaking the patterned electrical contacts (Figure 3.17). This problem was rectified by annealing the substrate after the membranes are stamped onto it. It was found that annealing at 350°C for 90 minutes in air was sufficient to provide strong enough adhesion to the substrate and stop the membranes moving during the fabrication process.

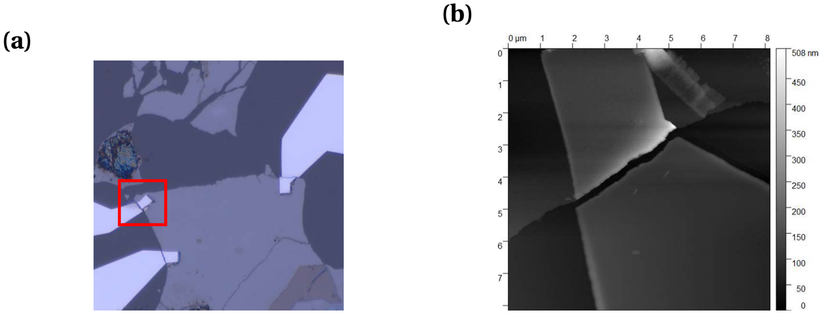

Figure 3.17: (a) Freestanding NNO membrane with 3 contacts broken due to membrane moving slightly after liftoff. (b) AFM of rectangle shown in (a)

3.5.5. NANOSCROLLS

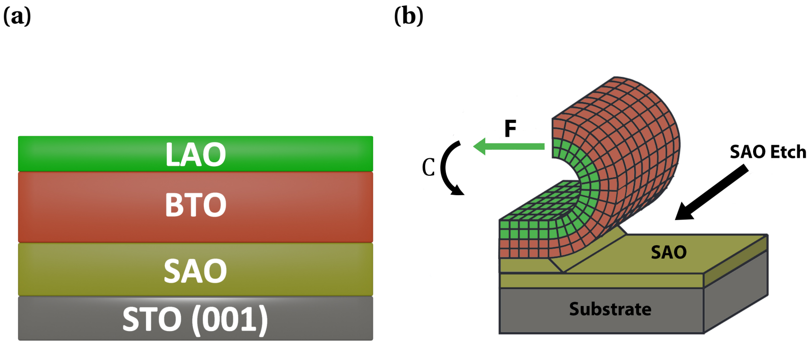

Figure 3.18: (a) LAO/BTO/SAO/SAO(001) heterostructure grown for rolling experiments (b) Schematic outlining how the combination of tensile strain and compressive strain (F) and etching can lead to thin film layers experiencing a curvature (direction C) due to a sacrificial layer being etched.

It has been demonstrated that significant curvature can be induced in freestanding thin films by means of strain gradients and layer etching [86, 87]. The mechanism is outlined in Figure 3.18 (b). Curvature can be induced by epitaxially growing two thin films which have a large difference of in-plane lattice parameters, and then etching the layer (or substrate) that the films are grown on. Specifically, the upper-most layer needs to have a smaller in-plane lattice parameter than the layer it is grown on ($a_1 < a_2$). In our case $LaAlO_3$(LAO) was grown on $BaTiO_3$(BTO)) (Figure 3.18 (a)) with lattice parameters a_{LAO} = 3.79Å and a_{BTO} = 4.01Å, where the LAO layer was thin (2nm) hence it was not strain-relaxed. The sacrificial layer used, SAO, has a lattice parameter of a_{SAO} = 3.99Å in bulk form, hence the BTO layer is relatively strain-free. Concordantly the requirement $a_1 < a_2$ is satisfied. The LAO layer experiences a large amount of tensile strain ($\approx 5.5\%$) and when the SAO layer is being etched, the LAO/BTO layers above the etched SAO are no longer epitaxially bound. The large tensile strain in the LAO layer then induces a force that causes the partially released LAO/BTO layer to curve inward. If the sacrificial layer is etched in a continuous fashion, rolled up nanotubes (called ‘nanoscrolls’) can be created [88]. It has been calculated how much of a lattice mismatch is required, with a determined layer thickness, in order to create a tensile strain large enough to induce the formation of nanoscrolls [89]. The required parameters are calculated using the following formulas:

$$\epsilon_1(\%) = \frac{a_{LAO} - a_{BTO}}{a_{BTO}} \times 100 \tag{3.1}$$

$$\epsilon_2(\%) = \frac{a_{BTO} - a_{SAO}}{a_{SAO}} \times 100 \tag{3.2}$$

$$\Delta\epsilon(\%) = \epsilon_2 - \epsilon_1 \tag{3.3}$$

$$\bar{\epsilon}(\%) = \frac{\epsilon_1 d_1 + \epsilon_2 d_2}{d1 + d_2} \tag{3.4}$$

Where ϵ_1,ϵ_2 are the in-plane lattice mismatches of the LAO/BTO layers (ϵ_1) and the BTO/SAO layers (ϵ_2). $\Delta\epsilon$ is the overall strain gradient of the relevant layers of the heterostructure (LAO/BTO/SAO layers). Lastly $\bar{\epsilon}$ is the average strain of the layers experiencing curvature-inducing forces (LAO/BTO) where the thicknesses of the LAO and BTO layers d_1,d_2 are taken into account respectively. Figure 4 in [89] outlines the necessary strain gradients and average strain required to produce nanoscrolls. Using the in-plane lattice parameters for LAO and BTO of thicknesses (2nm and 7nm respectively), one calculates the values $\epsilon_1 = -4.98\%$, $\epsilon_2 = 0.5\%$, $\Delta\epsilon = 5.98\%$, $\bar{\epsilon} = -0.717\%$. These strain gradient and average strain values are well above the values required for nanoscrolls to form. The radius of curvature can be estimated by using the following formula [90]:

$$R = \frac{1}{6}\frac{1}{\Delta\epsilon}\frac{(d_1 + d_2)^3}{d_1 d_2} \tag{3.5}$$

Where R is the radius of the nanoscroll, $\Delta\epsilon$ is the strain gradient found in Equation 3.3 and d_1, d_2 are the thicknesses of the upper and lower layers, which in our case are LAO and BTO respectively. Using the values found previously, one calculates $R = 1.35$nm. Figure 3.18 (c) shows an AFM image of a LAO/BTO nanoscroll that was fabricated. While the thickness of the nanoscroll is difficult to accurately determine due to probing a curved surface, it can be reasonably assumed that the overall radius of the nanoscroll is >50nm, hence it appears the nanoscroll has many windings. This follows the method outlined in [89] where they estimate hundreds of windings would occur for the strain gradients and average strain values that our LAO/BTO layers would create.

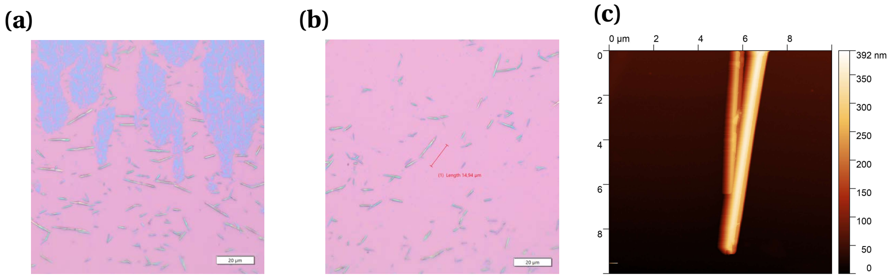

Figure 3.19: (a) 50x optical image of LAO/BTO membrane stamped onto a Si substrate. The cylindrical objects are LAO/BTO nanoscrolls that formed after stamping. (b) Optical image of nanoscrolls, with length scale provided. (c) AFM image of a LAO/BTO nanoscroll

3.6. AVOIDING SCHOTTKY BARRIERS IN FREESTANDING MEMBRANES

One significant hurdle with performing electron transport measurements on NNO membranes (described in Chapter 3) was the unwanted creation of Schottky barriers. In the past, NNO heterostructures have largely been contacted by depositing a metal with a high work function (such as Pt, or Ni) directly on top of the NNO layer. But, this was initially avoided in our work due to the idea of using a capping layer (10u.c STO) to protect the NNO layer from the membrane fabrication process. Hence to contact the NNO layer, in both heterostructure and freestanding membrane form, argon milling was required to etch through the capping layer. Unfortunately this argon milling resulted in the creation of large Schottky barriers when a metal was deposited. This occurred regardless of the metal deposited (Pt, Pd, Ni/Au and Al were attempted). Additionally, ensuring that the sample was kept in a high vacuum and depositing the metal immediately after etching still resulted in large Schottky barriers. The main sample used in the measurements described in Chapter 3 was uncapped, ie. it had no upper STO capping, hence no argon milling was required to contact the NNO film. While this stopped Schottky barriers from forming, it proved difficult to get low contact resistances due to unwanted residues on the NNO surface occurring from the freestanding membrane fabrication process. Thus, below is an outline of a potential fabrication process to create freestanding NNO Hall bars that will have no Schottky barriers and low contact resistances:

Use an uncapped NNO heterostructure, in this case the same heterostructure as in Figure 3.4 (b) but without the upper STO capping layer. Clean the surface vigorously with acetone, IPA and a Qtip. Using a positive resist (PMMA for example) and the design shown in Figure 3.20 (a), pattern, expose, and develop an array of this design on the top of the heterostructure (the NNO layer). Then deposit an appropriate metal (Pt for example) which will be contacted directly to the clean NNO surface. Perform liftoff with an appropriate method (acetone at 50°C for a number of hours for example). What should remain is an array of Pt contacts directly contacted to an NNO layer. Spincoat PMMA on this surface. Then, using the metal contacts and alignment markers as an alignment reference, expose all of the surface area outside both the contacts and the additional area

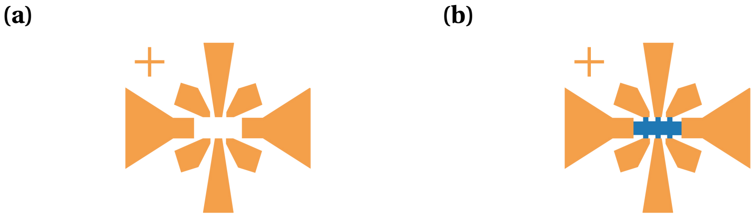

Figure 3.20: Possible CAD design of Hall Bar. Orange represents electrical contacts. Blue represents the area designated as the Hall bar (see text) (a) Step one of creating Hall bars (b) Step two of creating Hall bars

shown in blue in Figure 3.20 (b). Develop using the same method as previous. Afterwards, both the orange and blue areas in Figure 3.20 (b) should be covered in resist while the rest of the surface is exposed. Then the argon milling, exfoliating, and stamping procedure as described in Section 3.3 can be performed. Assuming the procedure was performed correctly, one will have freestanding membranes in the shape of the structure shown in Figure 3.20 (b). Note while there will be an NNO Hall bar, there will also be NNO underneath the contacts. This may actually be a benefit as it can be difficult to stamp metals directly onto complex oxides substrates due to a lack of sufficient adhesion. This method ensures that no part of the NNO membrane was directly exposed to argon milling. One question is whether the metal/NNO interface as well as the NNO surface is unaffected when being immersed in heated de-ionised water for a number of hours. Figure 3.21 highlights resistance vs temperature measurements performed on an NNO(20 u.c)/STO(001) sample where Pt pads were deposited in the corners of the 5 x 5mm square sample. The sample was then immersed in de-ionised water at 70°C for a number of hours, dried, and then had the resistance vs temperature measurements performed again. No significant change to the characteristic metal-insulator transition occurred but there is an overall increase in the resistivity after the water immersion. One reason could be due to the metal pads not being cleaned after water immersion and thus were dirtier before they were re-bonded to the holder chip with aluminium wire.

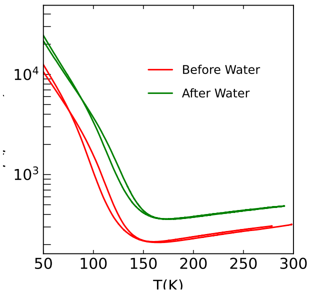

Figure 3.21: Comparison of NNO/STO heterostructure before and after being immersed in DI water at 70°C for a number of hours.

4

FREESTANDING $NdNiO_3$ MEMBRANES

High-quality freestanding $NdNiO_3$ membranes were fabricated, following which extensive structural and electrical characterisation measurements were performed. It was observed that not only the strain-free, freestanding $NdNiO_3$ membranes maintained their metal-to-insulator transition properties but that these transitions are sharper and more well-defined. Hall effect measurements show a lack of switching of charge carriers across the metal-insulator transition, highlighting the complicated connection between the material's strain and its electronic properties.

4.1. INTRODUCTION

Chapter 3 outlined a robust fabrication method to reliably produce arrays of high-quality freestanding $NdNiO_3$ membranes. Nickelates ($ReNiO_3$) are a class of complex oxides where strain plays a vital role in its intrinsic properties. One such phenomenon is its metal-insulator transition (MIT) temperature which can vary by hundreds of Kelvin depending on its strain state[91]. Thus they are a viable candidate to be investigated in the form of a freestanding membrane. This chapter investigates MITs measured in freestanding $NdNiO_3$ Hall bars and compares them to their epitaxial counterparts. The goal is to improve our understanding of the subtle, complicated relationship between strain and electronic properties in $NdNiO_3$.

4.2. NDNIO$_3$ AND STRAIN

ELECTRONIC CONFIGURATION

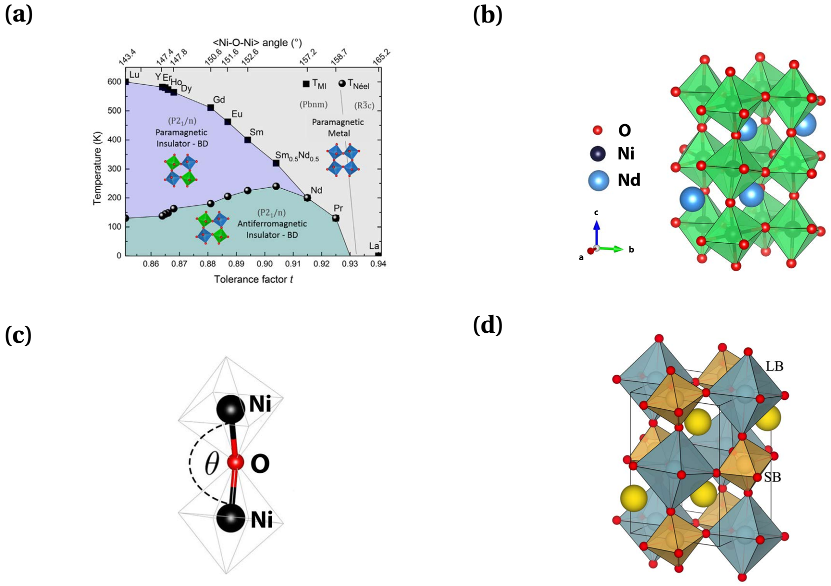

Figure 4.1: (a) Phase diagram of $ReNiO_3$ complex oxides. Figure taken from [91] (b) Orthorhombic unit cell of $NdNiO_3$ (c) Schematic of the defined bond angle θ between two adjacent Ni atoms in separate oxygen octahedra. In bulk $NdNiO_3$ this value is 157.2°[15, 92] (d) Breathing distortion in $NdNiO_3$ as $T < T_{MIT}$. The blue octahedra have larger bond lengths when below T_{MIT} while the yellow octahedra have smaller bond lengths respectively.

$NdNiO_3$(NNO) is a complex oxide that is orthorhombic at room temperature (space group $Pbnm$) where its orthorhombic unit cell can be described by a pseudocubic unit cell of lattice parameter $a_{pc} = 3.81$Å. The ground state electronic configuration can be described by d^8L where the central Ni atom (with electron configuration d^8) in the oxygen octahedra strongly hybridises with the surrounding oxygen atoms, resulting in ‘self doping' of a hole by an oxygen ligand (L)[19]. NNO is metallic in this state where the MIT of bulk strain-free crystals was first measured via differential scanning calorimetry in 1991[93]. As the temperature is cooled $NdNiO_3$ undergoes a first-order MIT where a structural phase transition takes place. The lattice becomes slightly monoclinic and bond length disproportonation occurs[94, 95, 96, 97], where a pattern of alternating larger and smaller oxygen octahedra forms[98]. The Ni atom inside the larger octahedra does not self dope resulting in d^8, while the Ni atom in the smaller octahedra is hole-doped by an additional oxygen ligand, resulting in d^8L^2. Thus these large and small octahedra result in the ground state electronic configuration $d^8 + d^8L^2$, where both d^8 and d^8L^2 describe insulating behaviour. Both the hysteretic behaviour and temperature where the MIT occurs (T_{MIT}) is strongly influenced by strain, whereby changing the Ni-O-Ni bond angle of connected octahedra changes the degree of overlap of the Ni-3d and O-2p bands[99, 100]. This overlap influences the material's electrical conductivity.

Strain is not the only knob one can use to tune the MIT of nickelate thin films. Oxygen vacancies and doping can heavily influence the MIT[101]. It has been somewhat difficult to isolate the nature of oxygen vacancies influence as it is also tied to strain. One way in which the nickelate films compensate for defects and oxygen vacancies is by forming Ruddleston-Popper(RP) phases. While HAADF-STEM can be used to view the phases directly[102], XRD can also provide evidence for their existence as RP phases have a larger c lattice parameter[103, 102] which results in a larger shift of an NNO peak than would be expected from solely lattice mismatch[104]. It is expected that a certain degree of RP phases would exist in our films as they consist of NNO being grown on STO substrates which has been shown to induce RP phases[105]. But surprisingly it is not clear that this is the case with our NNO films being grown on sacrificial layers.

4.3. SAMPLE FABRICATION

Samples of STO(001)/SAO/Ca2.5-SAO/STO/NNO/STO were prepared via pulsed laser deposition on a commercial 5x5mm TiO_2 terminated $SrTiO_3$ (001) substrate (SurfaceNet). The laser ablation was performed using a KrF eximer laser (Coherent LPXpro 305, λ = 248nm) with a pulse frequency of 1Hz. The thickness was monitored *in situ* using Reflection High Energy Electron Diffraction (RHEED) and each sample was post O_2 annealed with 300 mbar O_2 at 550°C. Another round of samples for the purpose of XRD and electrical transport measurements was prepared via PLD and off-axis sputtering. The SAO,Ca2.5-SAO and bottom STO capping layers were prepared via PLD as described in Section 4.4.1. The samples were then removed from the PLD chamber and placed in an off-axis sputterer where the NNO and top STO capping layers were then grown. The resulting heterostructure's structural properties were measured via XRD. Following this, Ni/Au pads were deposited on the corners of the samples via Ar milling and sputtering. Aluminium bonds were wire bonded onto the pads, allowing electron transport measurements to be performed via Van Der Pauw geometry. Following characterisation of the epitaxial heterostructures, an array of Hall bars was patterned on top of the 5x5mm heterostructure using electron-beam lithography and a positive photoresist (PMMA). The array consisted of 960 Hall bars, with each Hall bar of size 40μm x 10μm (length x width). The sample was then etched via Ar milling with a SCIA Mill 150, where the aluminium counts were measured *in situ* via a mass spectrometer. During the milling process a significant increase of aluminum signal indicated that the sacrificial layers were being etched. The milling was stopped shortly afterward to ensure that the etching stopped inside the sacrificial layers. The resist remaining on top of the Hall bar structures was then removed via acetone, IPA, and a q-tip. A PDMS stamp was then placed on top to the Hall bar structures. Both the stamp and etched heterostructure were fully immersed in deionised water. The stamp and attached heterostructure were held fully underneath the water surface, but not sitting at the bottom of the beaker, via clamps. The de-ionised water was heated to 80°C for 6 hours. If the substrate had not fallen the stamp and attached heterostructure was then removed from the water after which the stamp was peeled off the attached heterostructure. The exfoliated Hall bars attached to the PDMS stamp were then stamped onto a pre-patterned Al_2O_6 substrate using a dry-polymer transfer technique. The sapphire substrate was pre-patterned with alignment markers to facilitate the fabrication of electrical contacts to the freestanding Hall bars. Using electron-beam lithography Ni/Au contacts were contacted to the desired freestanding Hall Bars. The electron transport measurements that were performed on the epitaxial heterostructures were then repeated on the freestanding Hall bars. Some additional details of the samples measured are shown in table 4.1. Note two samples did not have an upper STO capping, thus their heterostructures consisted of NNO/STO/Ca2.5SAO/SAO/STO(001).

Table 4.1

Sample	**NNO layer thickness (unit cells)**	**Upper STO capping?**	**Contacts used for film (Metal)**	**Contacts used for Hall Bars (Metal)**
A	60	No	Pt	Ni/Au
B	80	Yes	Ni/Au	Ni/Au
C	60	No	Pt	-
D	80	Yes	Pd	-

4.4. RESULTS AND DISCUSSION

4.4.1. GROWTH CONDITIONS

A number of STO/NNO/STO/Ca-SAO/SAO/STO(001) heterostructures were grown with the purpose of investigating their structural and electronic properties before and after exfoliation. The growth of these heterostructures, including the RHEEDs, are largely described in Chapter 3. It should be repeated that while the sacrificial layers and bottom STO capping layers were grown via PLD, the NNO and upper STO capping layers for the samples described in this chapter were grown via off-axis sputtering. Hence the procedure was the following: The STO(001) substrate (SurfaceNet) was heated to 700°C and the SAO, Ca-SAO, and bottom STO capping layers were grown via the conditions described in Table 4.2. The sample was then cooled to 350°C at a rate of 10K per minute, after which it was annealed at 300mbar of O_2 for 1 hour. Afterwards the sample was cooled, removed from the PLD chamber and placed in the off-axis sputtering chamber. The sample was heated to 550°C and the NNO and top STO capping layers were grown. Afterwards the sample was once again cooled to 350°C and O_2 annealed for 1 hour.

Table 4.2

Layer	**Growth type**	**Temperature (°C)**	**Pressure (mbar)**	**Fluence* (J/cm^2)**	**No.Pulses**	**No.Unit Cells**
SAO	PLD	700	1×10^{-6}	1.2	800	40
Ca-SAO	PLD	700	1×10^{-6}	1.2	4000	100
STO(1st)	PLD	700	1×10^{-6}	1.2	120	4
NNO	Sputter	550	2×10^{-1} (3.5:1 - Ar:O2)	-	-	varied
STO(2nd)	Sputter	550	2.5×10^{-1} (3:2 - Ar:O2)	-	-	10

---

*With a rectangular laser spot area of $2cm^2$

4.4.2. AFM

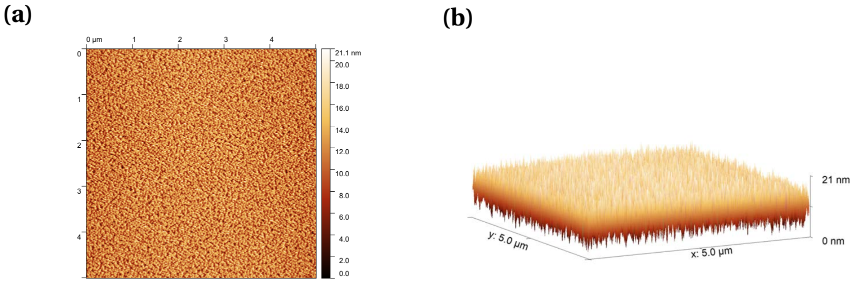

Figure 4.2: AFM scans on the top STO capping layer of NNO heterostructure of Sample A (a) $5\mu m^2$ area (b) 3D map of (a)

Figure 4.2 highlights the extremely rough surface that is produced when growing NNO on STO/Ca-SAO/SAO/STO(001). This is most likely due to the intrinsic vacancies and surface roughness that Ca-SAO/SAO exhibits (Figure 3.1). This roughness was observed for every NNO heterostructure (Section 4.6.1) that was grown in our lab. Remarkably a clear single-phase XRD signal and electronic MIT is still observed across multiple samples, highlighting that perhaps the NNO films consist of a percolation of large, interconnected crystallites. The surface roughness appears to be greatly reduced after exfoliation (20nm → $6nm$) as seen in Figure 4.3. One can hypothesise that the stamping process helps to 'smooth' out some of the surface roughness in combination with the NNO film no longer being bound to the rough sacrificial layer surface. That being said, if this scenario occurs it highlights the robustness of the the NNO layer as it is very malleable yet still able to produce clear XRD and MIT signals.

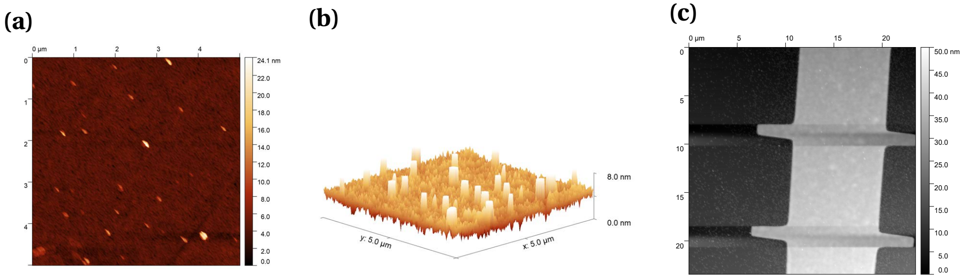

Figure 4.3: AFM scans of top STO capping layer of NNO heterostructure (a) 5um2 area (b) 3D map of (a) (c) 1um2 area

4.4.3. X-RAY DIFFRACTION

Figure 4.4 (a) displays the XRD spectra of Sample C of the $NdNiO_3$ (002) peak both in its epitaxial form and after exfoliation. The calculated c parameters are c_{epi} = 3.805Å and c_{fs} = 3.81Å (epi = epitaxial, fs = freestanding). The c_{fs} value can be explained by NNO being grown on Ca2.5-SAO where $c_{Ca2.5SAO}$ = 3.83Å, in combination with the thickness of the NNO layer (80 u.c) enabling a degree of strain relaxation. After exfoliation the (002) peak shifts back to its bulk value of 3.81Å, highlighting the strain release due to exfoliation. The FWHM of the NNO (002) peak appears to improve after exfoliation (0.3863 for film, 0.3370 for membrane). The peak at 46.47° is the (002) STO peak from the STO substrate. Note XRD scans for Sample A were only performed in epitaxial form and showed an identical (002) NNO peak, as seen in Figure 4.17 (a). The reason for this is mundane in that when using a sample to create an array of freestanding Hall bars the coverage of the Hall bars is not sufficient to produce a clear XRD signal in its freestanding form. Hence Sample C was grown as an identical counterpart to A for XRD purposes while Sample A focused more on electron transport.

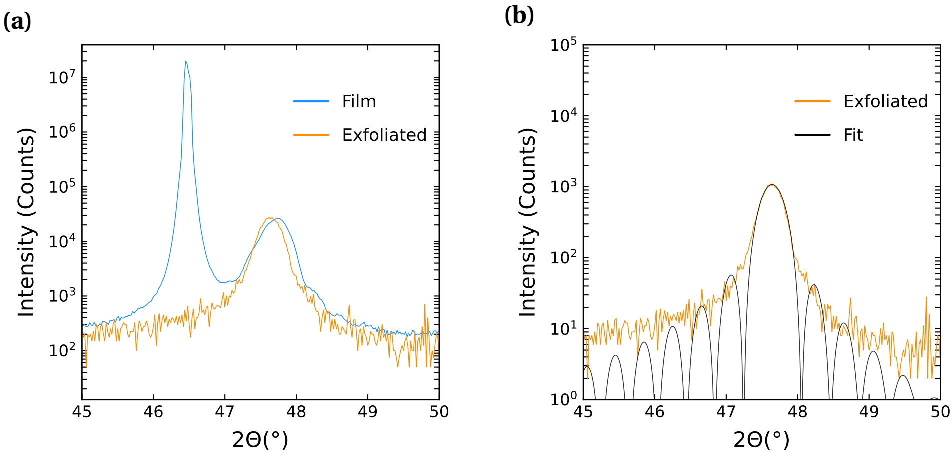

Figure 4.4: (a) X-Ray diffraction spectra around the (002) peak of NNO before and after exfoliation for Sample C. (b) Fit of NNO (002) peak after exfoliation.

4.4.4. ELECTRON TRANSPORT

AC MEASUREMENTS

Figure 4.5 shows the resistivity ρ vs temperature of sample A both before and after exfoliation. The MIT temperature(T_{MIT}) decreases slightly ($\Delta T \sim 13K$) after exfoliation. It is difficult to entail whether this decrease of T_{MIT} originates from the small strain release or the introduction of additional defects due to exfoliation but one may attribute it to the latter as an overall increase in resistivity is also observed in the membrane. A signature of defects can be the broadening of the measured XRD peak which is seen in Figure 4.4 where relatively high FWHMs are observed.

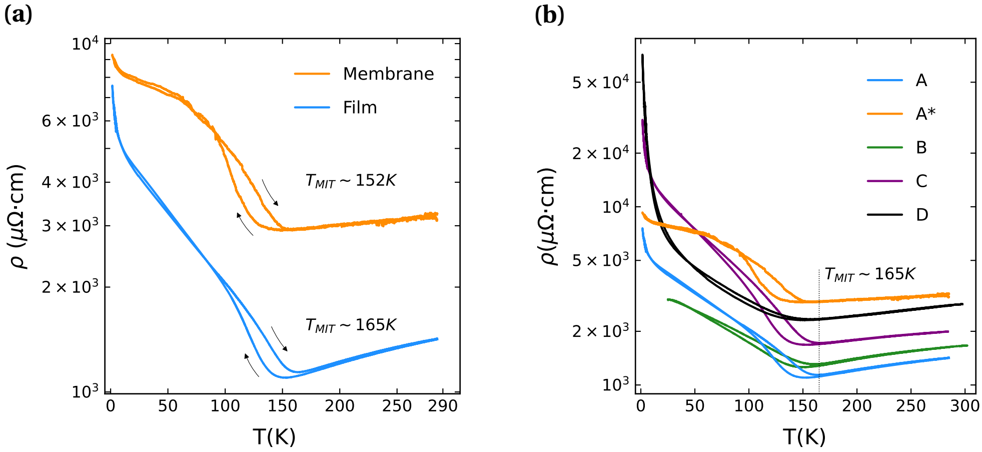

Figure 4.5: (a) Comparison of ρ vs T for sample A before and after exfoliation (b) ρ vs T for samples A-D where A* indicates that the sample is in freestanding membrane form.

Figure 4.6 (a) shows the resistivity values of Figure 4.5 (a) normalised with respect to the room temperature values (285K). It can be seen that both the area and slope of the hysteretic region increases after exfoliation. This can indicate that there are more 'switchable' domains available in the film after exfoliation, as will be described shortly. The electronic resistivity ρ of $NdNiO_3$ in the metallic regime (ie. T > T_{MIT}) can be described by a power law equation $\rho(T) = \rho(0) + AT^n$, where A is a coefficient describing electron scattering, T is temperature, $\rho(0)$ is the resistivity at 0K and n is a power exponent[106]. Figure 4.6 (b) shows the fitting of the metallic regime (160K - 285K) of Figure 4.6 (a). The slope of the metallic regime is reduced over twofold after exfoliation ($y_{film} = 0.0018 \pm 0.00001x + 0.4908 \pm 0.00014$, $y_{membrane} = 0.0007 \pm 0.00001x + 0.7788 \pm 0.00041$). The power exponent, of both the film and membrane, gives the best fit when using the power law equation with n = 1. Both this reduction in slope and having a power exponent equal to 1 (ie. linear) have been attributed to having strain-free films with minimal disorder and oxygen vacancies[105, 107, 108]. But, this is relatively surprising to observe in our samples due to their more disordered nature (Figure 4.2, Figure 4.4).

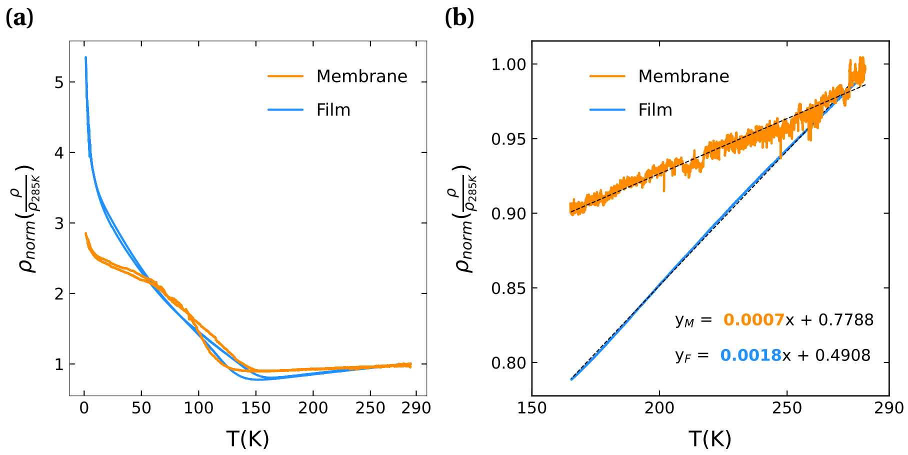

Figure 4.6: (a) Comparison of ρ_{norm} vs T for Sample A before and after exfoliation. (b) Linear Fitting of metallic regime.

Figure 4.5 (a) can also be used to extract information about the percolation of metallic and insulating regions below T_{MIT}. The hysteretic region of Figure 4.5 can be considered a combination of metallic and insulating regions, with the two region types having different conductivities respectively. The fraction of insulating regions within the material can estimated via a percolation model[109]:

$$V_s = \frac{(G_e - g_m)(g_s + G_e(D-1))}{DG_e(g_s - g_m)} \tag{4.1}$$

Where V_s is the volume fraction of the insulating region of the material, G_e is the measured conductance, g_m is the fitted conductance of the metallic region, g_s is the fitted conductance of the region below T_{MIT} and D is the dimensionality of the material. It has been shown that the temperature of the maximum slope of the resistivity, ($T_{\alpha,film,mem}$ for film and membrane respectively), found within the hysteretic region correlates to $V_s \sim 0.6$ in a wide range of nickelates in both bulk and thin film form, irrespective of the substrate the nickelate thin films are grown on[15]. Figure 4.7 compares V_s calculated for both the film and membrane of sample A. The right y-axis displays the slope of the resistivity vs temperature. The calculations were performed on the resistivity data measured via cooling down from room temperature to base temperature at a rate of 1K per minute. Figure 4.7 highlights that the trend described previously still holds where $V_s(T_{\alpha,film}) = 0.6$ and a slight increase of $V_s(T_{\alpha,mem}) = 0.67$ is found after exfoliation. This, in combination with an increase of the slope of the hysteretic region after exfoliation ($\frac{dLn(\rho)}{dT}(T_{\alpha,film}) = 0.38$, $\frac{dLn(\rho)}{dT}(T_{\alpha,mem}) = 0.46$) highlights that a sharper MIT occurs, even with an apparent increase in defects.

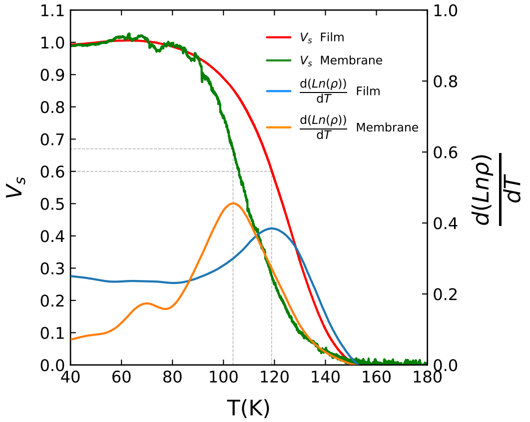

Figure 4.7: Left axis: Volume fraction of insulating regions (V_S) vs T. Right axis: $\frac{dLn(\rho)}{dt}$ vs T. The dotted lines are to guide the eye.

Similar phenomena and behaviours were observed in another NNO sample that was measured, both in its epitaxial and freestanding Hall bar form. But the measurements were performed via DC measurements due to reasons explained below.

DC MEASUREMENTS

Sample B (Table 4.1) had freestanding membranes measured via DC current bias. One significant hurdle with performing electronic transport measurements in freestanding NNO has been the unwanted creation of schottky barriers. It was found that schottky barriers almost always formed when trying to pattern metal contacts through STO-capped freestanding NNO Hall bars (Section 3.6). But, after sample B membranes displayed very large contact resistances due to a schottky barrier it was observed that linear IVs were still able to be measured when performed with a DC current bias. Figure 4.8 shows IVs performed on sample B over a temperature range 300K → 1.5K → 300K in steps of 10K. A large non-linear change in V was observed when applying DC current in the range -5μA$\leq 0 \leq 5\mu$A. This non-linear change also occurred when larger/lower current ranges were applied, for example if a current sweep of $\pm 100\mu$A was applied, the non-linear change would be seen between -20μA$\leq 0 \leq 20\mu$A. This non-linear change increased as the temperature decreased from room temperature and increased further after the sample cooled down below the MIT temperature ($T_{MIT} \approx 160K$). But surprisingly after the initial non-linear change at small values around 0μA, $\frac{dV}{dI}$ stabilises and becomes linear as the applied DC current increases. The measurements were performed via the following procedure: The temperature was increased/decreased by 10K at a rate of 1K per minute. Once the desired temperature was reached a settling time of 10 minutes was provided to allow the sample to thermalise. A DC current sweep of $\pm 10\mu$A was performed at a rate of $1\mu A$ per minute while the corresponding voltage was measured. The contact configuration was a standard 4-point Hall bar configuration. The following analysis was performed to extract the sample's resistivity:

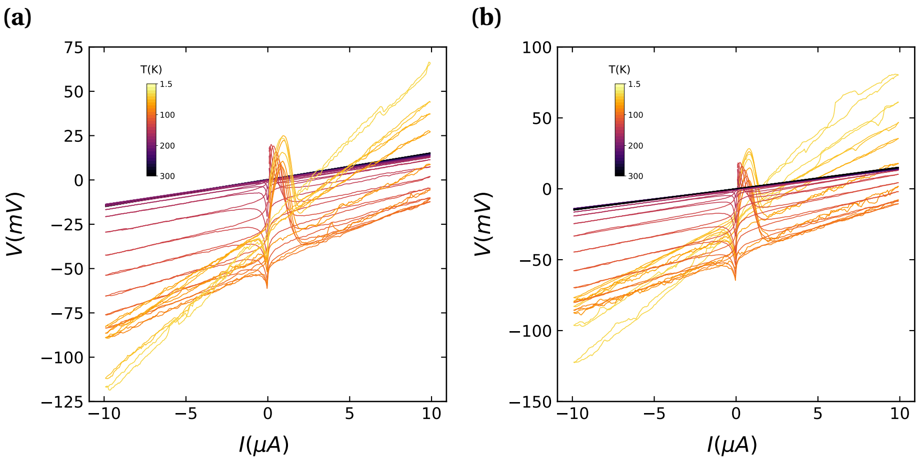

Figure 4.8: Raw IVs (a) Cooldown (b) Warmup

The raw IVs (Figure 4.8) were normalised to 0 so as to remove any offsets due to contact misalignment, defects, etc (Figure 4.9).

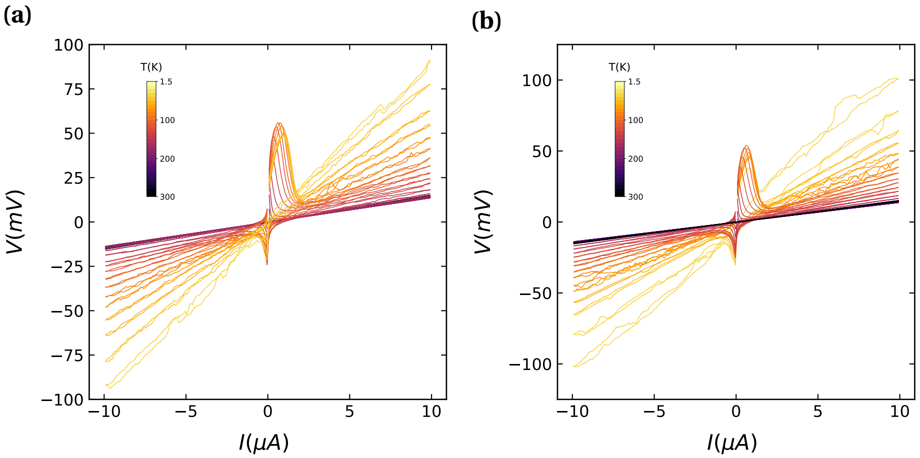

Figure 4.9: IVs Offsetted (a) Cooldown (b) Warmup

The data in the range $-5\mu\text{A} \leq 0 \leq 5\mu\text{A}$ of Figure 4.9 was then cut from the raw data and the resulting curves were fitted with a linear fit (Figure 4.10).

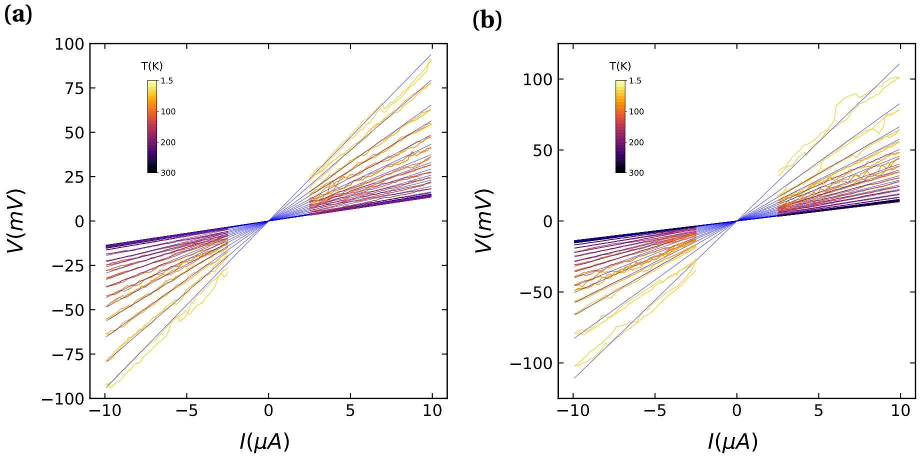

Figure 4.10: IVs Cut (a) Cooldown (b) Warmup

The linear fits of the data were then symmetrised to remove any further offsets (Figure 4.11).

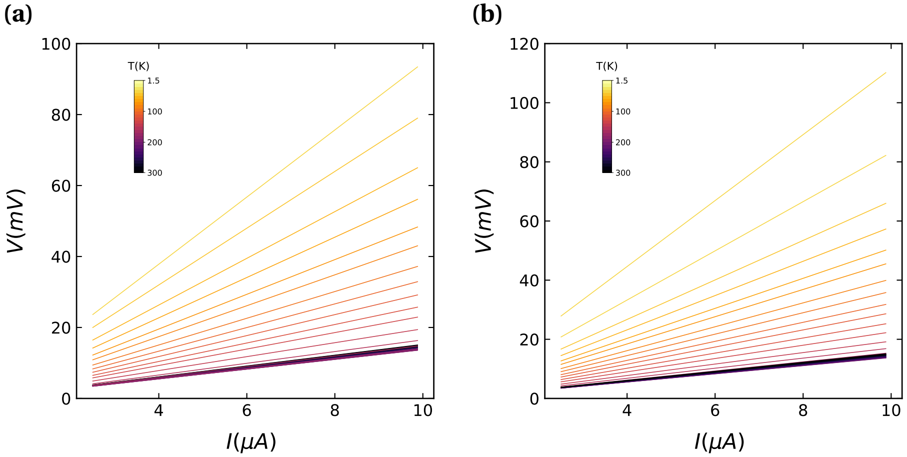

Figure 4.11: IVs Symmetrised (a) Cooldown (b) Warmup

Lastly the symmetrised IVs were then used to calculate the longitudinal resistivity of the sample at a number of temperatures. $\frac{dV}{dI}$ values were taken at I = 10μA, which were then converted to resistivity values ρ via $\rho = \frac{dV}{dI} \cdot A \cdot t$ where A is the sample area ($\frac{length}{width}$) and t is the sample thickness. For this sample A = 1 ($\frac{10\mu m}{10\mu m}$) and t = 30.48 × 10^{-9}m and a factor of 1 × 10^{11} was multiplied to convert ρ to units of $\mu\Omega$·cm.

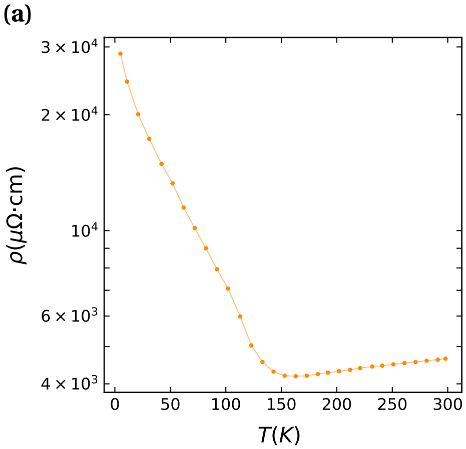

Figure 4.12: IVs R vs T (a) Cooldown (b) Warmup

Figure 4.13 shows the ρ vs T for NNO film of sample B in both epitaxial and freestanding form with $y_{film} = 0.0018 \pm 0.00001x + 0.7994 \pm 0.00313$, $y_{membrane} = 0.0018 \pm 0.00001x + 0.4894 \pm 0.00027$). Similar phenomenon is observed when compared to ρ vs T measurements performed via AC current bias in sample A. These include an increase of the overall resistivity, increased linearity of the metallic phase and an increased sharpness of the MIT. Note there is no noticeable change in MIT temperature ($T_{MIT} \approx 160$K). It also exhibits a similar change in resistivity values (increase of $\sim 2\times10^3 \mu\Omega$·cm).

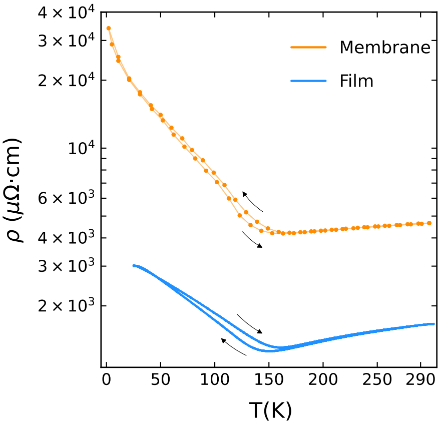

Figure 4.13: Comparison of DC ρ vs T for sample B before and after exfoliation

A linear fit of ρ_{norm} between the range 300K → T_{MIT} shown in Figure 4.14 (b) shows very similar values to sample A (Figure 4.6) with similar differences between their epitaxial and freestanding forms respectively.

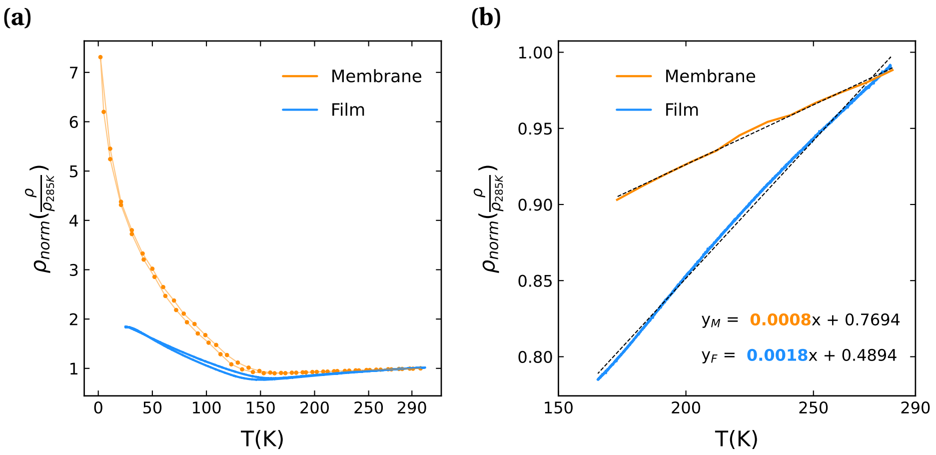

Figure 4.14: (a) Comparison of ρ_{norm} vs T for sample B before and after exfoliation. (b) Linear Fitting of metallic regime.

The volume fraction of sample B also exhibits similar volume fraction values to sample A with $V_S = 0.63$ in freestanding form. Note it was difficult to extract a value of V_S at the peak of $\frac{dLn(\rho)}{dT}$ for the epitaxial form as the MIT was very broad resulting in no clear $\frac{dLn(\rho)}{dT}$ peak. A slight peak may be seen at T = 120K which translates to $V_S = 0.53$.

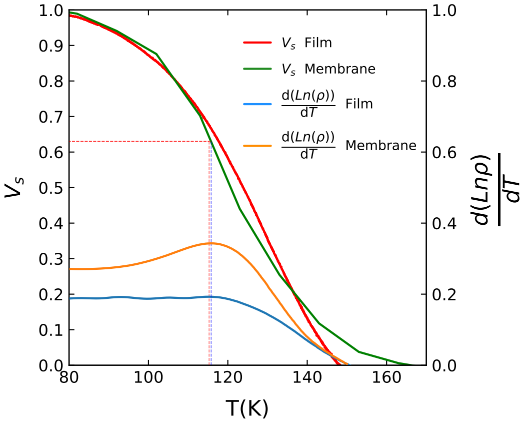

Figure 4.15: Left axis: Volume fraction of insulating regions (V_s) vs T. Right axis: $\frac{dLn(\rho)}{dt}$ vs T. The dotted lines are to guide the eye.

4.4.5. HALL MEASUREMENTS

NNO exhibits a prominent Hall effect that is heavily tied to strain, oxygen vacancies, and doping. Assuming bulk, unstrained NNO, at room temperature its Hall coefficient (R_H) is positive which indicates holes are the majority charge carrier[110]. Above the MIT temperature ($\mathrm{T_{MIT}}$) R_H remains relatively unchanged. But if the sample is cooled below T_{MIT} a rapid sign change occurs, indicating a change in majority charge carriers from holes to electrons. As the temperature is reduced further R_H becomes increasingly negative[111]. To gain insight into this one can look at the first Brillouin zone of NNO thin films on LAO, Figure 4.16, where NNO/LAO experiences minimal compressive strain (≈ 0.5%). At room temperature the Brillouin zone consists of 4 hole pockets at the corners and one small electron pocket in the center. As NNO is cooled below T_{MIT} the central electron pocket greatly increases. Thus this change in electron/hole pockets leads to a change in the sign of Hall coefficient. The size and nature of these electron and hole pockets are also dependent on strain, with tensile strain increasing the size of the hole pockets and compressive strain increasing the size of the electron pocket[112]. But confusingly the Seebek effect, which revolves around temperature gradients inducing a voltage, exhibits the opposite phenomenon. The Seebek coefficient S is negative at room temperature, indicating electron majority carriers while it switches to positive as the temperature is cooled below T_{MIT}. It is hypothesised that due to the multiband nature of NNO, different bands are utilised for thermal transport compared to electronic transport[111]. Nevertheless the Hall effect is a useful tool to quantify the number and type of charge carriers in NNO.

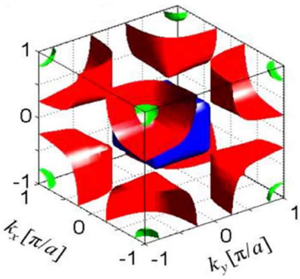

Figure 4.16: Schematic of the first NNO Brillouin Zone, taken from [113]. Hole pockets (red) are in the corners while there is a central electron pocket (blue).

This is expanded further when one includes additional factors such as strain and doping. Starting with strain, it has been shown that tensile strain positively increases R_H meanwhile compressive strain decreases it[112, 114]. These results were obtained by growing NNO thin films on a number of different substrates where the lattice mismatch induces biaxial epitaxial strain. Somewhat similar results are seen when NNO thin films are doped[115, 116]. For example replacing a number of Ni atoms with Zn or Ce leads to a change in the valency of the remaining Ni atoms from $\mathrm{Ni^{3+}}$ to $\mathrm{Ni^{4+}}$. Structural changes were observed such as a slight shift in the (002) NNO peak indicating either an increase in the c lattice parameter due to the change in unit volume and/or an increase in compressive strain. Nevertheless an overall increase in R_H was observed which is proportional to the degree of doping.

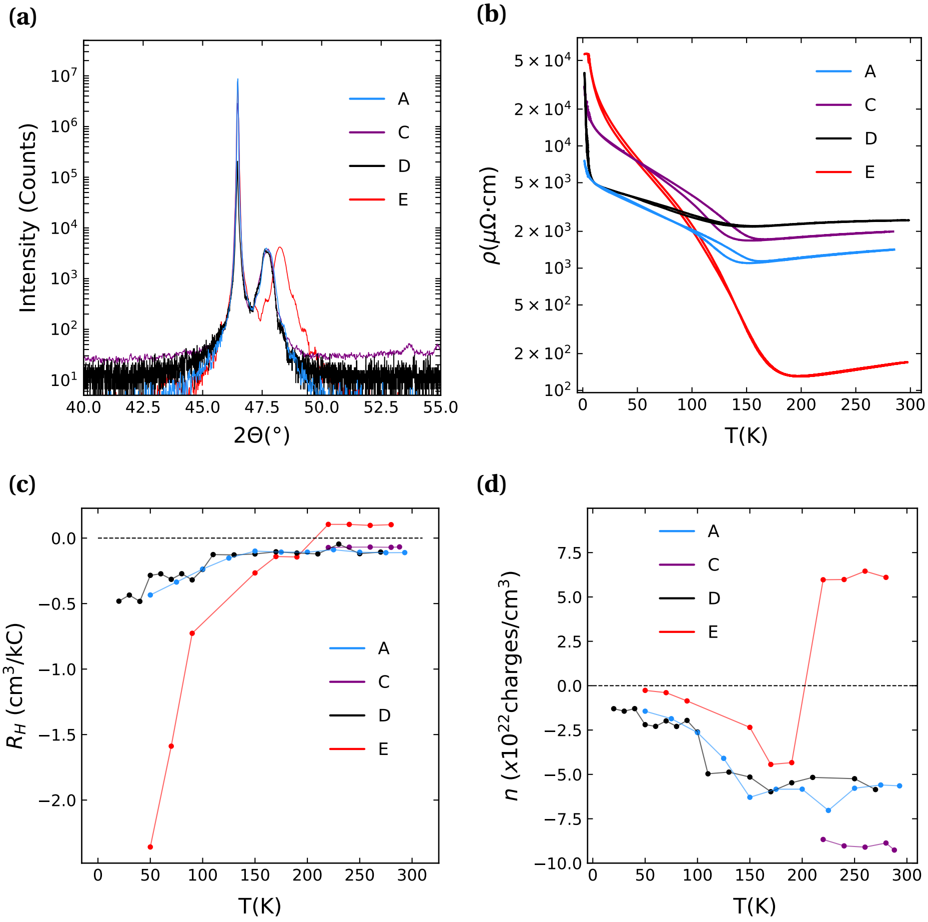

Figure 4.17: (a) XRD scans of samples A,C,D and E. The sharp peak at ≈ 46.47° is the (002) STO peaks while the peaks to the right of it are the (002) NNO peaks. Note samples A,C and D all have very similar c lattice parameters (3.83Å) while the peak for sample E is shifted to the right (c lattice parameter ≈ 3.77Å) due to being tensile strained to the STO substrate with no sacrificial layers. (b) ρ vs T for samples A,C,D and E. Note for sample C measurements were only performed in the metallic regime. (c) Hall coefficient (R_H) vs T (d) carrier density (n) vs T

Samples A,C and D were used to investigate the Hall effect in NNO films on sacrificial layers, details such as their heterostructures and thicknesses are described in Table 4.1. An additional sample, sample E, was grown as a control sample of 60 units cells of NNO grown on an STO substrate via sputtering. The control sample helped confirm the accuracy of the sign determination of R_H (see Appendix 4.6.2). Figure 4.17 (b) displays the RTs of these samples while Figure 4.17 (c) displays the results of their corresponding Hall effect measurements. Starting with the control sample (sample E) in 4.17 (c): There is a positive R_H above its T_{MIT}(190K) with values similar to other works of NNO/LAO heterostructures[111]. The characteristic sign change across T_{MIT} is also seen where R_H decreases further as the temperature is reduced. Meanwhile samples A and D exhibit their own similar R_H values and behaviours. R_H remains negative across all temperatures and decreases further as the temperature is cooled below T_{MIT} (A:165K, D:150K). Sample C was only measured above T_{MIT} but similar R_H values are also observed. Figure 4.17 (d) displays the charge carrier concentration of the samples over the measured temperature range. Sample E has holes as the majority charge carrier above T_{MIT} while it switches to electrons as the temperature is cooled below T_{MIT}. Meanwhile for samples A and D the majority charge carriers are electrons across the entire temperature range. One similarity across all samples is the increase of n towards zero as the samples are cooled further into the insulating regime.

Having electrons as majority charge carriers across the entire temperature range from room temperature to base temperature is not seen in many other works. This electron majority is unusual as it is opposed to the bond-disproportionation picture that is nowadays used to describe the origin of the MIT. Many works have confirmed the significant presence of holes in NNO which aligns with the scenario of an electronic configuration based on hole-doping[19, 117]. This was largely observed by X-Ray absorption and Resonant Inelastic X-Ray Scattering. An electron-majority Hall effect is observed when NNO is grown on $YAlO_3$ substrates where the NNO thin films experience a large amount of compressive strain (3.6%) and the MIT is fully quenched[114]. But the lack of a shift in the XRD peaks of our samples (Figure 4.17 (a)) indicate that they are relatively strain relaxed. Also while the MITs are broadened compared to sample E, clear MITs with hysteresis are still apparent. While O_2 vacancies could be a source of carrier injection, normally a large shift in XRD peaks are seen due to O_2 vacancies increasing the out-of-plane lattice parameter[101]. The very rough surface topologies (Figure 4.2, also Appendix 4.6.1) and the broad XRD peaks(Figure 4.17 (a)) of these samples indicate that a large amount of structural disorder is apparent, even if the NNO thin films are strain-free and single-phase. More investigation will be required to determine whether this very disordered surface is one explanation for this electron-majority Hall effect. Unfortunately due to large contact resistances and Schottky barriers Hall effect measurements were unable to be performed on the freestanding NNO membranes. But utilising the method described in Section 3.6, one perhaps may produce contact resistances low enough for clear Hall effect signals to be measured.

4.5. CONCLUSIONS

Ultra-thin freestanding NNO membranes were created and their structural and electronic properties were investigated. It was observed that while there was minimal strain-release due to the lattice-matching of the CAO sacrificial layer with the NNO film, the MITs were significantly sharper after exfoliation showing an increased volumetric fraction. An accurate resistivity measurement and analysis method was also demonstrated for scenarios where significant Schottky barriers occur between the NNO surface and deposited metal contacts. Hall measurements on NNO films epitaxially bound to the sacrificial layer heterostructure outline the sensitivity of the charge carrier density to defects.

4.6. APPENDIX

4.6.1. ADDITIONAL AFMS

Additional AFM scans of NNO heterostructures and freestanding membranes grown and fabricated over the course of this work. Note Figure 4.18 (a)-(b), (g)-(h) and (i)-(j) are scans of samples grown identically to sample A with the same heterostructure layers and thicknesses.

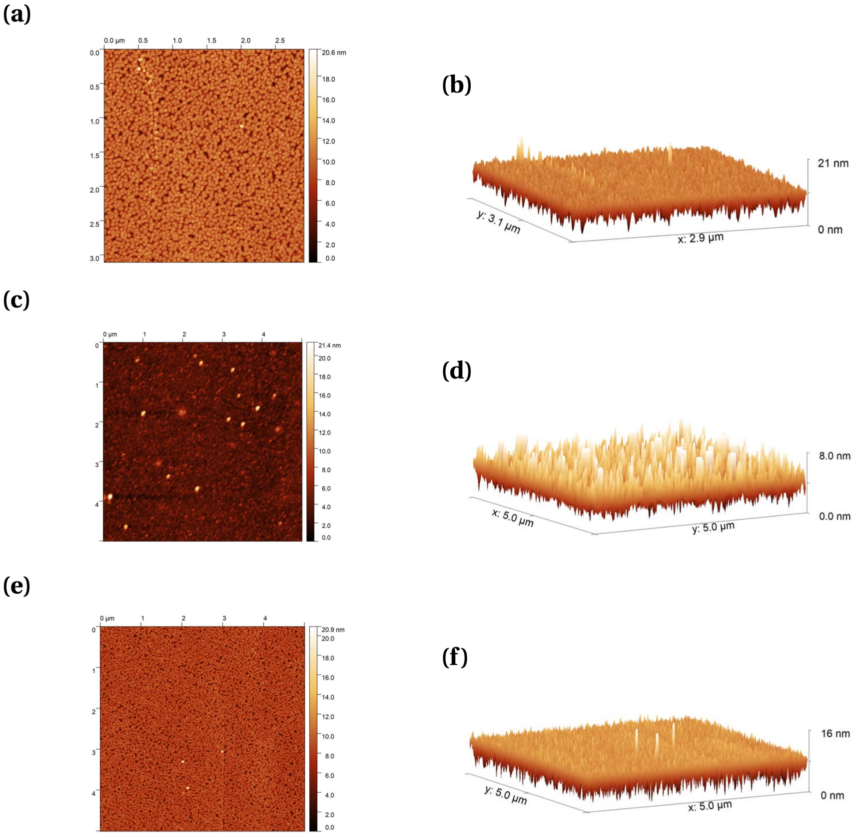

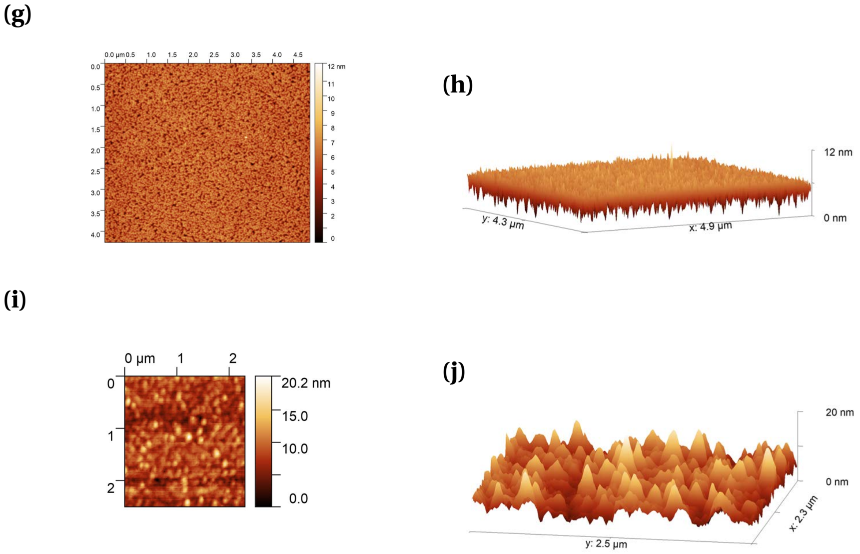

Figure 4.18: (a) AFM scans of an additional NNO heterostructure identical to sample A (b) Corresponding 3D topography map of (a) (c) AFM scan of a freestanding Hall bar produced from sample A (d) Corresponding 3D topography map of (c) (e) AFM scan of sample D (f) Corresponding 3D topography map of (e) (g) AFM scan of another NNO heterostructure identical to sample A (h) Corresponding 3D topography map of (g) (i) AFM scan of a freestanding Hall bar fabricated from the sample shown in (g)-(h) (j) Corresponding 3D topography map of (g)

4.6.2. HALL SIGNS

Figure 4.19 (a) outlines the axes and current direction conventions that are used[118] in this work, ie. one assumes conventional current and a right-handed axes system. Note B points into the sample for our measurements. Figure 4.19 (b)-(f) shows the direction of the current applied (I) under an applied magnetic field (B) with the corresponding Hall voltage measured (V_{H+},V_{H-}). The numbers in the corners are the labels of the contacts used, where the subscripts I(+-),V(+-) show the directions and configurations used when performing the measurement. For example in Figure 4.19 (b): Current is applied between contacts 5(I+) and 11(I-), and the transverse voltage was measured between contacts 12(V+) and 6(V-). In this case a positive voltage signal was measured which increased positively with increasing B, which means the deflection of majority charge carriers produces a potential gradient which is positive in the direction of 12 → 6. This is outlined by the V_{H+} symbol being at contact 12 and V_{H-} being at contact 6.

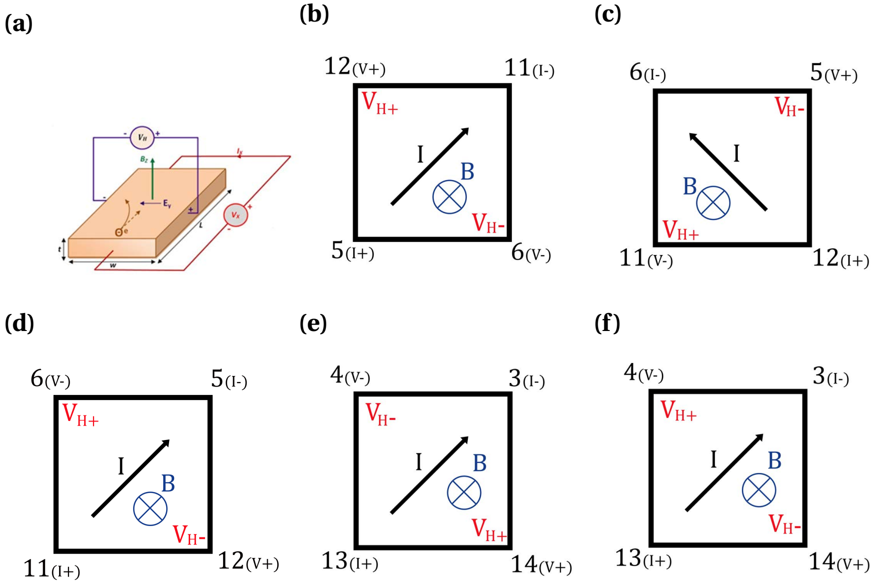

Figure 4.19: Current and voltage probe configurations to calculate the correct signs of the measured Hall effect (a) Axes and current direction conventions that are used[118]. One assumes conventional current and a right-handed axes system (b) Sample C Hall measurements (c) Sample D Hall measurements (d) Sample A Hall measurements (e) Sample E Hall measurements (metallic regime) (f) Sample E Hall measurements (insulating regime)

5

COMPLEX OXIDE MEMBRANES - SUBSTRATE BONDING

This chapter focuses on the applicability of freestanding membranes and their use in measurements outside of structural characterisation and electrical transport. A fabrication method to stamp freestanding complex oxide membranes on TEM grids is discussed. A temperature-dependant X-ray diffraction experiment of freestanding $SrRuO_3$ *membranes on an STO(001) substrate was performed, which in combination with optical acoustic measurements of these membranes provides insight into the nature of the bonding of the freestanding membrane with the substrate it is stamped onto. Lastly reciprocal space mapping of freestanding* $SrRuO_3$ *was performed.*

5.1. INTRODUCTION

The previous chapters outlined the creation of freestanding complex oxide membranes and investigated their structural, electronic, and magnetic properties. This chapter delves into their applicability outside of electronic applications with an emphasis on utilising their freestanding nature to facilitate new, informative experiments and measurements. Firstly a technique is described to allow in-plane lattice parameters of these membranes to be measured via reciprocal space mapping. Secondly a process allowing freestanding complex oxide membranes to be investigated via TEM is described, where measurements along the z-axis can be performed due to being stamped onto a TEM grid. Lastly a temperature-dependant X-Ray diffraction experiment is performed with the goal of investigating the nature of the bonding between the freestanding complex oxide membrane and the substrate it is stamped onto. This experiment is performed in tandem with an optics experiment measuring the acoustic properties of these membranes over the range of measured temperatures. Hence this chapter highlights how freestanding complex oxide membranes can open up complex oxides to a wide array of new, insightful experiments and fields.

5.2. RECIPROCAL SPACE MAPPING OF FREESTANDING STRONTIUM RUTHENATE MEMBRANES

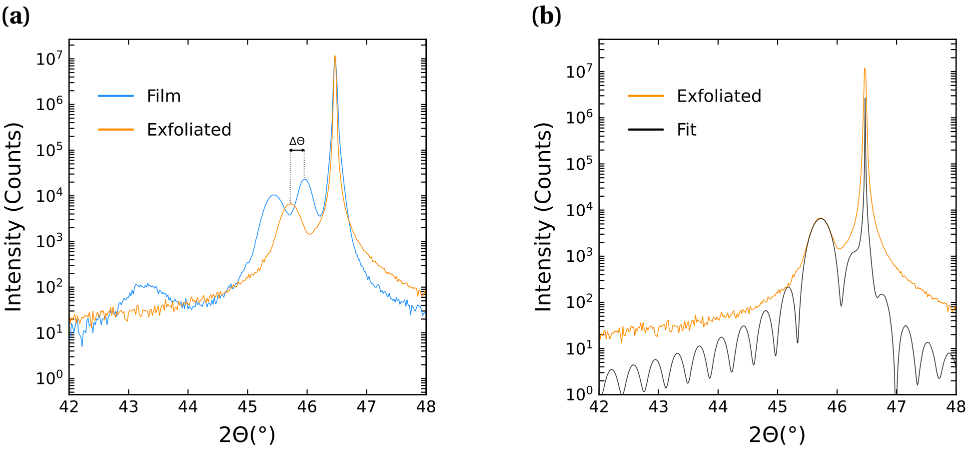

Figure 5.1: (a) XRD scans of 80uc SRO sample before (blue) and after exfoliation (orange). $\Delta\theta$ is the shift of the 002 SRO peak due to strain release after exfoliation. $\Delta\theta = 0.24°$ (45.96° - 45.72°). The peak at $2\theta = 45.96°$ is the (0006) Ca-SAO peak while the peak at 43.24° may be an additional SAO phase unintentionally created [119]. (b) A fit of the exfoliated XRD scan.

A series of reciprocal space maps (RSM) were performed on an SRO sample (STO(10uc)/SRO(80uc) /STO(5uc)/Ca0.5SAO/SAO/STO(001)) that was exfoliated and the SRO membrane was stamped onto an STO(001) substrate. One difficulty of performing RSMs on freestanding membranes is the lack of a reference when performing the peak alignments and scans, Figure 5.2 outlines this in more detail.

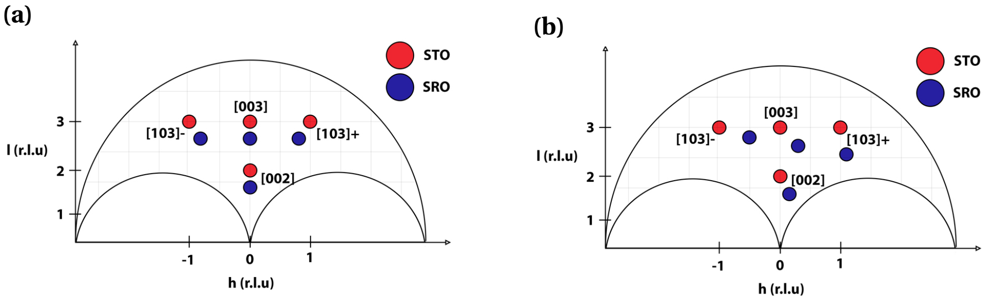

Figure 5.2: (a) Reciprocal space map of SRO epitaxially bound to STO. Note the positions of the peaks are not exact due to illustrative purposes. (b) Reciprocal space map of a freestanding SRO membrane stamped onto an STO substrate at an arbitrary angle. Note the rotation of the SRO peaks about the origin.

Figure 5.2 (a) displays the typical reciprocal space map for a strain-relaxed SRO film epitaxially bound to an STO substrate. The STO peaks in reciprocal space have a larger distance between them compared to SRO as STO has a smaller cubic lattice parameter (STO - 3.905Å, SRO_{pc} - 3.93Å). Meanwhile if a freestanding SRO membrane is stamped onto an STO substrate it is only attached via Van der Waals forces. Hence the standard method of simply using the difference between the peak's h values used to calculate in-plane strain may not be completely accurate. Also the membrane may not be fully flat when stamped on the substrate. This misalignment manifests itself as the SRO peaks appearing to be rotated around the origin[120], see Figure 5.2 (b). But, the in-plane lattice parameters of the freestanding membrane may still be calculated. The following procedure was performed:

1. Align 2θ & ω on the [002] STO peak.
2. Go to the [103]+ STO peak using the alignment performed on the [002] STO peak.
3. Align 2θ & ω on the [103]+ STO peak.
4. Perform RSM scans on the [103]+ STO and [103]+ SRO peaks. A larger, lower-resolution scan may be required to find the [103]+ SRO peak before performing a smaller, higher-resolution scan.
5. Go back to the [002] STO peak
6. Align 2θ & ω again on the [002] STO peak.
7. Perform steps 2-4 for the [103]- peaks.

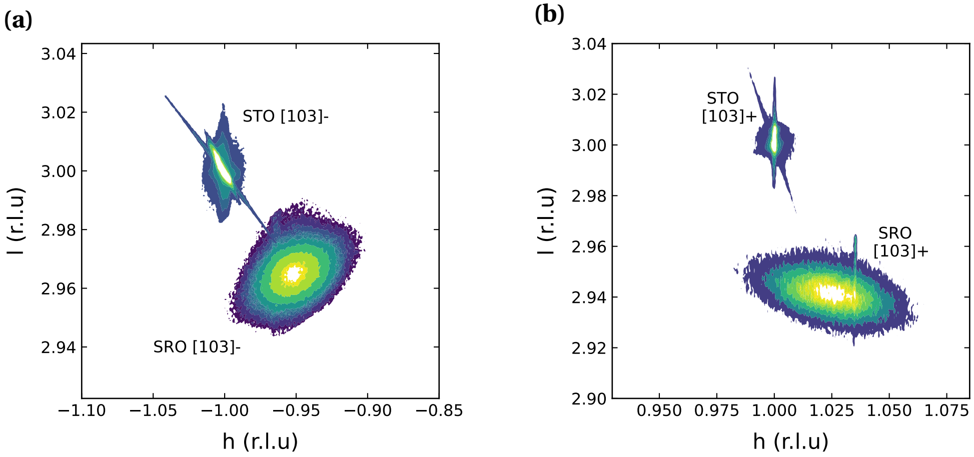

Figure 5.3: (a) Reciprocal Space scans of SRO[103]- and STO[103]- (b) Reciprocal Space scans of SRO[103]+ and STO[103]+

The [103]+ and [103]- peaks are shown in Figure 5.3 (a) and (b) respectively. It should be noted that if the SRO was epitaxially bound the SRO [103]+ peak should be to the left of the [103]+ STO peak, as shown in Figure 5.2 (a). But, if the SRO peaks are rotated in a clockwise direction around [000] it's possible for the SRO [103]+ peak to be to the right of the STO [103]+ peak. Calculating the in-plane lattice parameters from Figures 5.3 does not provide valid values due to the SRO peak rotation. But, a possible solution is outlined in Figure 5.4.

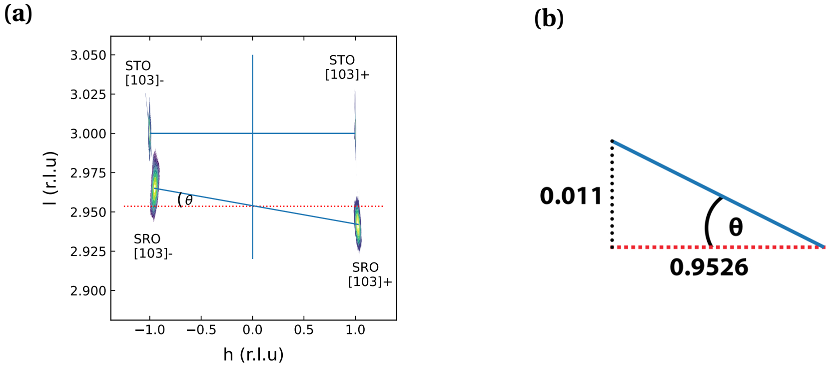

Figure 5.4: (a) Plot of the peaks shown in Figure 5.3 with horizontal lines connecting the positions of each respective peak's maximum intensity. The single vertical line represents [00l]. The dotted red line displays a horizontal line intersecting intersecting the [00l] line and the line connecting the two SRO peaks. (b) The right-angled triangle used to calculate the angle of rotation between the two SRO peaks.

Figure 5.4 (a) shows all the measured peaks (STO[103]+, SRO[103]+, STO[103]+, SRO[103]-) on the same plot. The SRO peaks show rotation as described previously. A line was plotted between the maximum intensity values of the STO and SRO peaks. This line is linear for the STO peaks while there is an angle θ for the SRO peaks. Using the intersection of this line with a vertical line through the origin, a horizontal line can be mapped (shown as the dotted red line). Considering the triangle in Figure 5.4(b), the distance of the hypotenuse and the opposite are known, where the distance of the opposite is found by plotting a vertical line from the maximum value of the SRO peak to the red horizontal line. Using standard trigonometry θ can be found ($\theta = 0.6°$). One can now rotate the SRO peaks by this θ value so that the SRO peaks are parallel with each other. This is performed using the following rotation matrix equations:

$$\begin{bmatrix} x' \\ y' \end{bmatrix} = \begin{bmatrix} cos(\theta) & -sin(\theta) \\ sin(\theta) & cos(\theta) \end{bmatrix} \cdot \begin{bmatrix} x \\ y \end{bmatrix} \tag{5.1}$$

Where x, y are the original coordinates, θ is the angle shown in Figure 5.4, and x', y' are the coordinates after rotation. Then one can compare the distance between the two SRO peaks to the distance between the STO peaks (2 reciprocal lattice units (r.l.u)). Hence one can calculate the in-plane lattice parameters (a_{SRO} = 3.946Å). Using these rotated coordinates the out-of-plane lattice parameter can also be calculated and was found to be the same as the value found via the XRD scans (c_{SRO} = 3.966Å). The broadness of the SRO peaks indicates the existence of defects and/or the presence of multiple domains with slightly different lattice parameters. It should be noted that Figure 5.4 describes two unconnected crystal lattices. The STO peaks are merely used as alignment and distance-to-lattice parameter references. The 'rotation' described does not have any significant physical meaning, it is merely a way to map one misoriented crystal lattice onto an oriented one with known lattice parameters.

The sample then underwent an extensive thermal annealing treatment during a measurement process described in a later section (Section 5.4). The sample was slowly heated to 750°C and cooled back down to room temperature and the same reciprocal space mapping measurements of the [103] peaks were performed again. The [103] SRO and STO peaks are shown in Figure 5.5 where Figure 5.5 (c) is a plot showing all the measured peaks. One significant difference between these peaks and the peaks measured before the annealing treatment (Figure 5.4 (a)) is the lack of rotation between the SRO [103]- and SRO [103]+ peaks. This could indicate that the membrane is now flatter due to being more strongly bonded to the substrate. Since there is no rotation the procedure described for Figure 5.4 is not necessary. The lattice parameters found for the SRO membrane after annealing are a_{SRO} = 3.956Å, c_{SRO} = 3.943Å. The c-lattice parameter matches the value found via XRD scans (Figure 5.7 (d)). Thus it is observed that after annealing to 750°C, the membrane increases its in-plane lattice parameter (a_{SRO} = 3.946Å→ a_{SRO} = 3.956Å) while it decreases it's out-of-plane lattice parameter (a_{SRO} = 3.966Å→ a_{SRO} = 3.943Å). One explanation is that O_2 vacancies are known to increase the lattice parameter of SRO[121], hence annealing in air oxygenates the membrane filling the O_2 vacancies produced when growing the heterostructure.

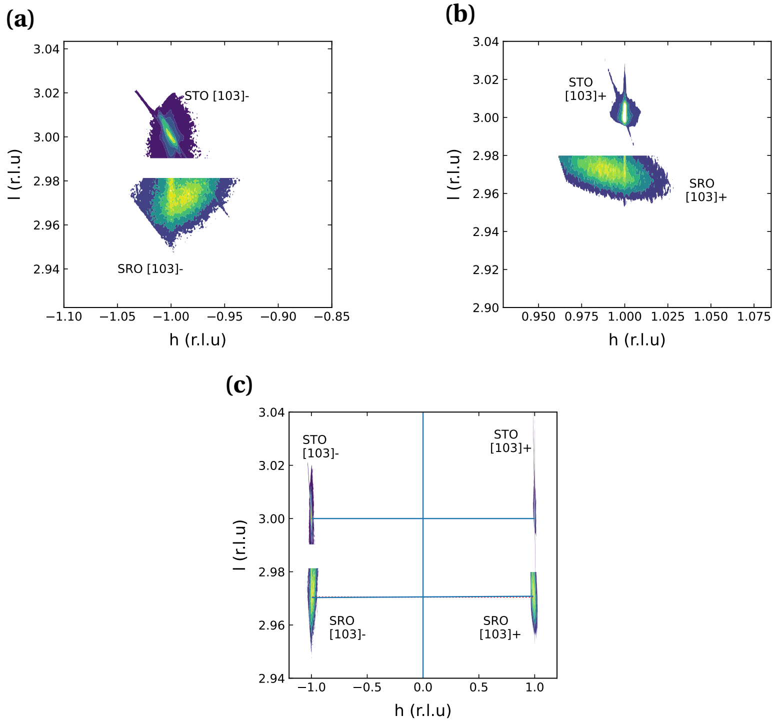

Figure 5.5: Reciprocal Space maps of 80uc SRO membrane stamped on STO(001) after being annealed to 750°C in air and cooled back down to room temperature (a) RSMs of STO[103]- and SRO[103]-. Note the peaks were scanned separately and there was some overlap between the two scans. Hence some data between the two peaks are cut for clarity. The maxima of both peaks are still clearly visible. (b) RSMs of STO[103]+ and SRO[103]+. Note the peaks were scanned separately and there was some overlap between the two scans. Hence some data between the two peaks are cut for clarity. The maxima of both peaks are still clearly visible. (c) RSM plot of all the peaks measured. Note the lack of rotation between the SRO[103]- and SRO[103]+ peak. There is a red dotted line similar to the one shown in Figure 5.4 (c) but it is obscured by the blue line horizontally connecting the maxima points of the two peaks. Hence no rotation method is necessary.

5.3. TRANSMISSION ELECTRON MICROSCOPY

FREESTANDING MEMBRANE SHAPE CONTROL FOR TRANSMISSION ELECTRON MICROSCOPY

When preparing complex oxide heterostructures for transmission electron microscopy(TEM) measurements, a series of fabrication steps has to be performed. This involves etching the heterostructure with a focused-ion beam (FIB) in order to create lamella with well-defined edges. One purpose of this is so that the crystallographic directions of the edges of the lamella can be defined and hence are known. This is vital to accurately determining important observations such as cation displacements and octahedral tilts. One difficulty with freestanding membranes in the past has been the lack of control in creating well-defined edges[122]. When performing the method outlined in Figure 2.3, membranes of random shapes and sizes are produced with edges that have random crystallographic directions. The fabrication procedure in Section 3.3 can provide a way to rectify this. This was demonstrated with freestanding NNO membranes being prepared for TEM measurements. In more detail:

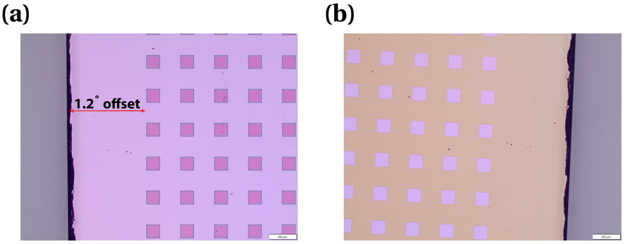

Figure 5.6: (a) Optical image of an NNO heterostructure (described in text) after development. There is an angle of 1.2° between the edges of the membranes (to be exfoliated) and the sample edge. (b) Same as shown in (a) but after the argon milling etching step and resist removal.

An STO/NNO/STO/Ca-SAO/SAO/STO(001) heterostructure (same layer configuration as Figure 3.4) was grown with the same growth parameters previously described in Table 4.2. The thickness of the NNO layer was 100 unit cells. An array of 50μm x 50μm square membranes was patterned on top of the heterostructure via e-beam lithography and positive resist. Care was taken to ensure that the pattern was well aligned with the sample edges, with an angle of 1.2° seen between the membranes and the edges after development (Figure 5.6 (a)). The heterostructure was then etched, exfoliated, and stamped via the procedure described in Section 3.3 with the etched heterostructure after the resist removal step shown in Figure 5.6 (b).

One useful aspect of this procedure is that after recording the initial offset the membranes have with the sample edges (Figure 5.6 (a)), it does not matter what direction the membranes are stamped onto the substrate, nor does one have to keep track of the membrane directions during the fabrication procedure itself. Another key aspect is that the membranes no longer have to be stamped onto a substrate, they can be stamped onto a TEM grid directly allowing TEM measurements to be performed in the z-axis direction. Attempts were made to stamp the membranes created in Figure 5.6 onto nickel TEM grids. Nickel was chosen as TEM can be sensitive to hydrocarbon residues, thus either plasma or annealing is required to remove any hydrocarbon residues from the sample before the TEM measurements can take place. While O_2 plasma can alter the surfaces of complex oxides[123], annealing on the other hand is a possibility. Complex oxides can easily be annealed up to 300°C with minimal changes to the intrinsic crystal structure or degradation. Hence nickel grids were chosen due to their high temperature stability. The nickel grid (agar Scientific 3.05mm diameter, 600 Mesh) had a grid size of 30μm ensuring that the 50μm x 50μm square membranes could be fully supported by the grid. For the stamping procedure itself, the TEM grid was placed on a film of PDMS (Gel Pak 8). This PDMS had a stronger adhesive factor compared to the PDMS stamp holding the NNO membranes. The purpose of this was that the TEM grid had a tendency to become attached to the PDMS stamp and lifted up with the stamp when the stamp was removed after a stamping attempt. But regardless, unfortunately it proved difficult to stamp the freestanding membranes onto the nickel TEM grid. While the TEM grid remained firmly in place on the stickier Gel Pak 8 PDMS film, the NNO membranes would not stick to the TEM grid. Increasing temperatures were used (80-180°C) but alas to no avail. Possible improvements and developments to this method can be the following:

- O_2 plasma the TEM grid prior to stamping. Metals undergone O_2 plasma treatment can have dangling bonds on the surface resulting in greater adhesion properties[124].
- Try TEM grids of other metals. While nickel was useful due to its temperature stability, other grids such as aluminium or titanium could also be viable and have greater adhesion.
- Use PMMA during the exfoliation procedure described in Section 3.3. While PMMA creates much more hydrocarbon residues, they can be removed or converted to carbon residues via annealing. A thick PMMA film containing the membrane could be stamped onto the TEM grid. Then the TEM grid and PMMA film on top could be immersed in acetone and annealed to remove hydrocarbon residues.

5.4. TEMPERATURE-DEPENDENCE OF FREESTANDING STRONTIUM RUTHENATE MEMBRANES - XRD ANALYSIS

The freestanding SRO sample described in Section 5.2 (80u.c SRO stamped onto an STO(001) substrate) also had X-ray diffraction measurements performed over a wide temperature range. XRD scans were run over a temperature range of 25°C → 750°C in steps of 50°C. Settling times of 30 minutes after each 50°C increase was to allow for adequate thermalisation to occur before the XRD scans ran. The results are displayed in Figure 5.7 where a number of phenomenon is observed.

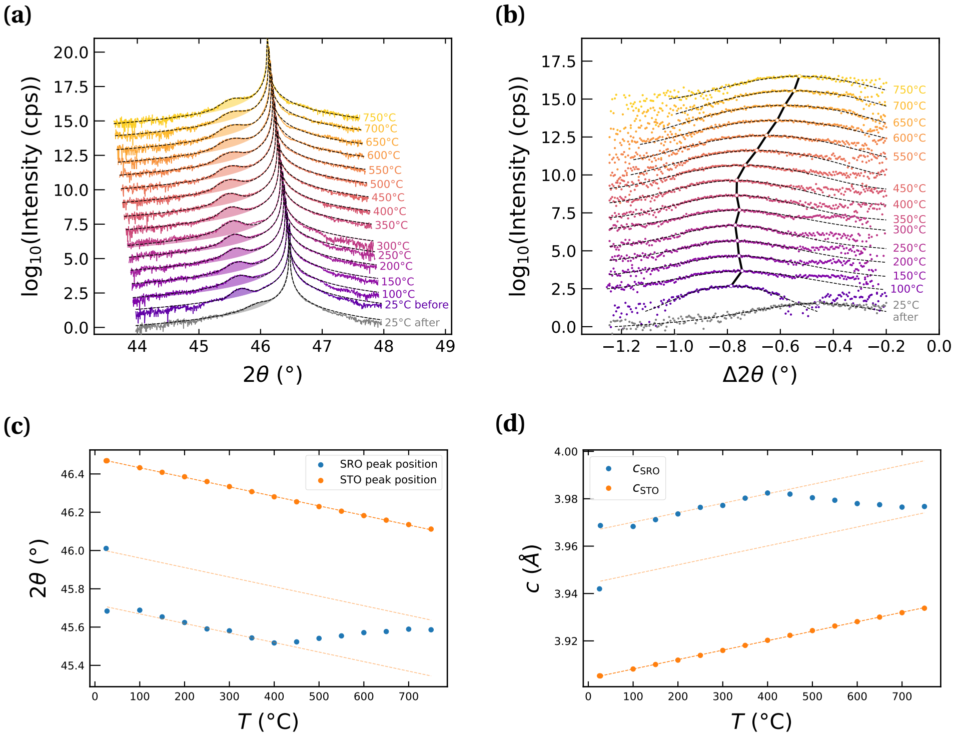

Figure 5.7: (a) XRD scans on a 80uc SRO membrane stamped onto an STO (001) substrate. The XRD scans were performed at a number of temperatures, ranging from room temperature to 750°C in steps of 50°C. An additional XRD scan was performed after the sample had the XRD scan at 750°C and cooled slowly back to room temperature. (b) Zoomed in section of (a) highlighting the 2θ shift of the (002) SRO peak due to temperature. (c) Plot of the shift in 2θ vs temperature. A noticeable change in the 2θ shift of the SRO membrane occurs when $T > 400$°C. Above 400°C the change in 2θ is no longer linearly proportional to temperature, where a linear temperature dependence originates from the thermal expansion of the lattice. (d) A plot of the out-of-plane lattice parameter (c_{SRO}) vs temperature highlighting the change above 400°C also seen in (c). Additionally, c_{SRO} reverts back to a linear dependence as it is cooled from 750° back to room temperature.

Figure 5.7 (a) displays the 2θ vs ω scans across the (002) SRO and (002) STO peaks over a number of temperatures. The SRO membrane appears to maintain its crystallinity even at temperatures above its growth temperature (550°C) highlighting the robustness of the membrane. Changes to the peak positions, and hence the out-of-plane lattice parameters, are observed as the temperature is increased with full the trend plotted in Figure 5.7 (d). The STO c lattice parameter is linearly proportional to the increase in temperature indicating that this change in the c lattice parameter is largely due to thermal expansion of the lattice. Meanwhile SRO shows different behaviour. Its change in c lattice parameter starts off linear but then deviates above a temperature of 400°C. This is unusual as there is no known temperature-dependant phase transition at that temperature, SRO is known to go from orthorhombic to tetragonal above 550°C[26]. Also this change in lattice parameter is maintained as the temperature is cooled from 750°C back to room temperature (Figure 5.7 (d)) ie. the c lattice parameter simply follows a linear thermal reduction as the temperature is cooled. One explanation may lie in the bonding between the membrane and the substrate, as described below:

In combination with these XRD measurements, acoustic phonon measurements were performed on another similar freestanding SRO membrane (10 u.c STO / 80uc SRO / 5uc STO stamped onto an STO(001) substrate), with the results shown in Figure 5.8b. These measurements were performed by fellow group member Mattias Matthiessen (work to be published via both thesis and publication).

(a)

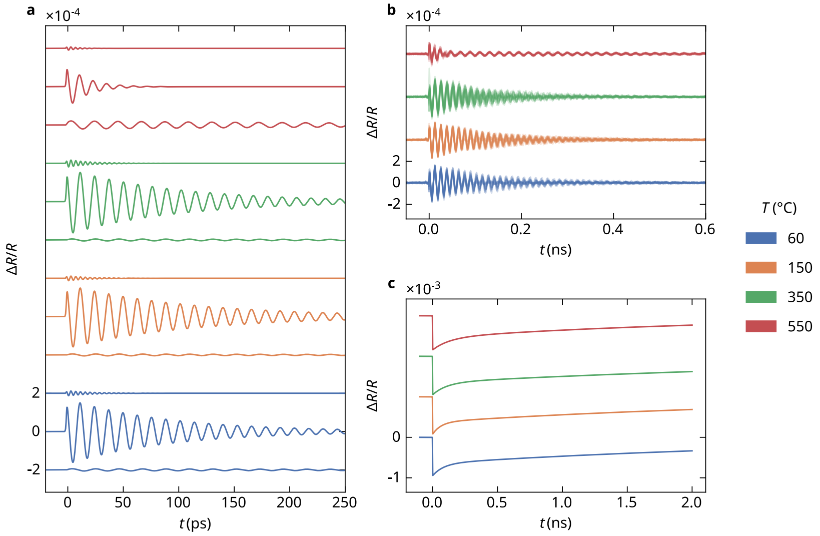

(b) Annealing temperature (T) study of phonon dynamics. Measurements performed and plotted by colleague Mattias Matthiessen. (a) Oscillatory components to the least-squares solution, offset for visibility. The slowest frequency is the Brillouin oscillation, the intermediate frequency is the dilatational mode of the membrane, and the fastest signal is the third harmonic of that membrane mode. (b) Raw signal, with the background subtracted. c. The biexponential background component of the least-squares solution.

Using an asynchronous optical sampling setup a number of SRO membranes on the stamped substrate were subject to a THz pump-probe experiment that measured the membrane's reflectivity. The setup consisted of two synchronized pulses emitting 100MHz pulse trains which were offset by a small amount (offset in the range of kHz). The wavelength of the probe was 780nm (ie. THz range) with an average power of 100μW. The pump had a wavelength of 1560nm with an average power of 100mW. A number of membranes were measured after which the sample was annealed at a certain temperature, cooled back to room temperature, and the membranes were measured again. The temperatures at which the sample was annealed and measured was 60°C, 150°C, 350°C, 550°C and 750°C. Reflectivity oscillations were observed indicating the presence of a confined acoustic phonon, but the amplitude of these oscillations decreased dramatically above 550°C. This decrease in amplitude implies that the measured phonon is no longer confined to the membrane and is now able to travel into the substrate due to a change (ie. stronger) bonding between the membrane and the substrate. These results in combination with the temperature-dependent XRD results indicate that: When the SRO membrane was stamped, it was attached to the STO substrate via Van der Waals forces. But when the sample was heated above 400°C stronger covalent(or ionic) bonding between the membrane and the substrate begins to form. This stronger bonding is then maintained as the sample is cooled back down to room temperature.

5.5. CONCLUSIONS

Freestanding SRO and NNO membranes were utilised in experiments ranging from TEM, acoustics to temperature-dependent XRD. A method for analysing reciprocal space maps of freestanding membranes was outlined allowing one to calculate the in-plane lattice parameters of the freestanding membranes. An investigation into the nature of the bonding between the freestanding membranes and the substrate was performed via temperature-dependent XRD and acoustics measurements.

6

CONCLUSION

Chapter 1 provides an overview of the materials, measurement techniques, and theoretical concepts required to delve into the work outlined in this thesis. In Chapter 2 the fabrication, measurement, and investigation of freestanding SRO membranes is discussed. High-quality, crystalline, metallic SRO membranes were fabricated showing structural properties similar to bulk. Electrical transport confirmed the metallic nature of the SRO membranes and the ferromagnetic transition below its Curie point. SQUID and magnetotransport measurements highlighted how the strain release due to exfoliation can influence SRO's uniaxial magnetocrystalline anisotropy and its Fermi velocity in the direction of the Weyl cone tilt vector. Chapter 3 describes a robust fabrication process that enables the creation of crack-free arrays of freestanding complex oxide membranes of any desired shape. The use of a modified sacrificial layer is discussed (Ca-SAO) which, used in tandem with the sacrificial layer SAO, provides a means to solve the problem of lattice mismatch. Chapter 4 explores the structural and electronic properties of freestanding NNO membranes, comparing them to their epitaxial counterparts. The unique electronic and structural properties of NNO are shown to be preserved after exfoliation and furthermore the MIT is observed to be sharper and more well-defined when measured in its freestanding membrane form. Chapter 5 describes techniques that helps facilitate the measurement of freestanding complex oxide membranes by TEM. Additionally, a method to perform reciprocal space mapping of freestanding complex oxide membranes is discussed. Lastly a temperature-dependant XRD measurement of SRO membranes, in tandem with an investigation of the membranes' acoustic phonon properties, provides insight into the nature of the bonding between a freestanding complex oxide membrane and the substrate it is stamped onto.

6.0.1. FUTURE PERSPECTIVES

The key to the success of freestanding complex oxide membranes lies in their versatility. They open up measurement techniques and scenarios that are difficult or otherwise inaccessible in bulk form. For example Hong et.al[2] managed to induce very high degrees of uniaxial strain in freestanding LSMO membranes. Given the sensitivity of NNO to strain, investigating how the MIT of NNO membranes evolves with uniaxial strain could perhaps provide further insight into its origin, as well as push the boundaries of its robustness.

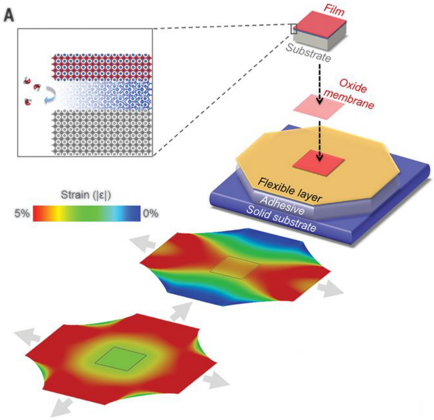

Figure 6.1: Figure taken from [2]. Describes the method by which they induce uniaxial strain in complex oxide membranes. The membrane is stamped onto a thin polyimide film, which itself lies on a thin layer of polycaprolactone. Polycaprolactone has a low melting point (~ 70°C) thus after the membrane is stamped, the polycaprolactone is heated. When the polycaprolactone has melted, micromanipulators stretch the polyimide and the membrane also (presuming the membrane is strongly bonded to the polyimide).

Apart from strain, membranes also open up the ability to control the angles between complex oxide interfaces. If one can carefully control the angle at which a membrane is stamped onto a substrate a Moiré pattern can form[125]. For example a Moiré pattern between two $BaTiO_3$ membranes was recently demonstrated[3] where they observed modulations in the ferroelectric polarization due to the induced shear strains, something which would be difficult to perform epitaxially.

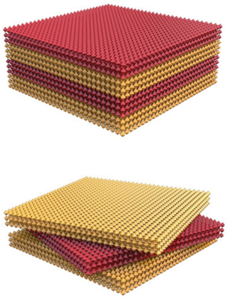

Figure 6.2: Figure taken from [125]. Outlines the twisting of freestanding membranes in combination with stamping.

BIBLIOGRAPHY

[1] F. Niklaus et al. "Adhesive wafer bonding". In: *Journal of Applied Physics* 99.3 (Feb. 2006).

[2] Seung Sae Hong et al. "Extreme tensile strain states in La0.7Ca0.3MnO3 membranes". en. In: *Science* 368.6486 (Apr. 2020), pp. 71–76.

[3] G. Sánchez-Santolino et al. "A 2D ferroelectric vortex pattern in twisted BaTiO3 freestanding layers". In: *Nature* 626.7999 (Feb. 2024), pp. 529–534.

[4] D. Davidovikj et al. "Ultrathin complex oxide nanomechanical resonators". In: *Communications Physics* 3.1 (Sept. 2020).

[5] Xia Chen and Wenbo Mi. "Mechanically tunable magnetic and electronic transport properties of flexible magnetic films and their heterostructures for spintronics". en. In: *J. Mater. Chem. C Mater. Opt. Electron. Devices* 9.30 (2021), pp. 9400–9430.

[6] V Ya Prinz et al. "A new technique for fabricating three-dimensional micro- and nanostructures of various shapes". In: *Nanotechnology* 12.4 (Nov. 2001), pp. 399–402.

[7] B. Andrei Bernevig, Claudia Felser, and Haim Beidenkopf. "Progress and prospects in magnetic topological materials". In: *Nature* 603.7899 (Mar. 2022), pp. 41–51.

[8] Di Xiao, Ming-Che Chang, and Qian Niu. "Berry phase effects on electronic properties". In: *Reviews of Modern Physics* 82.3 (July 2010), pp. 1959–2007.

[9] N. P. Armitage, E. J. Mele, and Ashvin Vishwanath. "Weyl and Dirac semimetals in three-dimensional solids". In: *Reviews of Modern Physics* 90.1 (Jan. 2018).

[10] J. J. Sakurai and Jim Napolitano. *Modern Quantum Mechanics*. Cambridge University Press, Sept. 2020.

[11] V. Fock. "Uber die Beziehung zwischen den Integralen der quantenmechanischen Bewegungsgleichungen und der Schrodingerschen Wellengleichung". In: *Zeitschrift for Physik* 49.5–6 (May 1928), pp. 323–338.

[12] Charles A Brau. *Modern Problems in Classical Electrodynamics*. en. New York, NY: Oxford University Press, Oct. 2003.

[13] Robert Karplus and J. M. Luttinger. "Hall Effect in Ferromagnetics". In: *Physical Review* 95.5 (Sept. 1954), pp. 1154–1160.

[14] P A Cox et al. "The metal-to-semiconductor transition in ternary ruthenium (IV) oxides: a study by electron spectroscopy". In: *Journal of Physics C: Solid State Physics* 16.32 (Nov. 1983), pp. 6221–6239.

[15] G. Catalan, R. M. Bowman, and J. M. Gregg. "Metal-insulator transitions in NdNiO3". In: *Physical Review B* 62.12 (Sept. 2000), pp. 7892–7900.

[16] N F Mott. “The Basis of the Electron Theory of Metals, with Special Reference to the Transition Metals”. In: *Proceedings of the Physical Society. Section A* 62.7 (July 1949), pp. 416–422.

[17] Ranjan Kumar Patel et al. “Hole doping in a negative charge transfer insulator”. In: *Communications Physics* 5.1 (Aug. 2022).

[18] N. F. MOTT. “Metal-Insulator Transition”. In: *Reviews of Modern Physics* 40.4 (Oct. 1968), pp. 677–683.

[19] Valentina Bisogni et al. “Ground-state oxygen holes and the metal–insulator transition in the negative charge-transfer rare-earth nickelates”. In: *Nature Communications* 7.1 (Oct. 2016).

[20] Jongho Ji et al. “A review on recent advances in fabricating freestanding single-crystalline complex-oxide membranes and its applications”. In: *Physica Scripta* 98.5 (Apr. 2023), p. 052002.

[21] Petr Ptáček. “Introduction”. In: *Strontium Aluminate - Cement Fundamentals, Manufacturing, Hydration, Setting Behaviour and Applications*. InTech, July 2014.

[22] Petr Ptáček. “Hydration and Setting Behaviour of Strontium Aluminate Cements”. In: *Strontium Aluminate - Cement Fundamentals, Manufacturing, Hydration, Setting Behaviour and Applications*. InTech, July 2014.

[23] A. K. Prodjosantoso, Brendan J. Kennedy, and Brett A. Hunter. “Synthesis and Structural Studies of Strontium-Substituted Tricalcium Aluminate Ca3-xSrxAl2O6”. In: *Australian Journal of Chemistry* 53.3 (2000), p. 195.

[24] C B Eom et al. “Single-Crystal Epitaxial Thin Films of the Isotropic Metallic Oxides Sr1-xCaxRuO3 (0 le x le 1)”. en. In: *Science* 258.5089 (Dec. 1992), pp. 1766–1769.

[25] G. Herranz et al. “SrRuO3/SrTiO3/SrRuO3 heterostructures for magnetic tunnel junctions”. In: *Journal of Applied Physics* 93.10 (May 2003), pp. 8035–8037.

[26] Gertjan Koster et al. “Structure, physical properties, and applications of SrRuO3 thin films”. In: *Reviews of Modern Physics* 84.1 (Mar. 2012), pp. 253–298.

[27] Y. Z. Yoo et al. “Diverse effects of two-dimensional and step flow growth mode induced microstructures on the magnetic anisotropies of SrRuO3 thin films”. In: *Applied Physics Letters* 89.12 (Sept. 2006).

[28] S. Kolesnik et al. “Effect of crystalline quality and substitution on magnetic anisotropy of SrRuO3 thin films”. In: *Journal of Applied Physics* 99.8 (Apr. 2006).

[29] Zhong Fang et al. “The Anomalous Hall Effect and Magnetic Monopoles in Momentum Space”. In: *Science* 302.5642 (Oct. 2003), pp. 92–95.

[30] H.B. Nielsen and M. Ninomiya. “Absence of neutrinos on a lattice (i) Proof by homotopy theory”. In: *Nuclear Physics B* 185.1 (July 1981), pp. 20–40.

[31] H.B. Nielsen and M. Ninomiya. “Absence of neutrinos on a lattice (ii) Intuitive topological proof”. In: *Nuclear Physics B* 193.1 (Dec. 1981), pp. 173–194.

[32] Di Tian et al. “Manipulating Berry curvature of SrRuO3 thin films via epitaxial strain”. In: *Proceedings of the National Academy of Sciences* 118.18 (2021), e2101946118.

[33] J. Smit. “The spontaneous hall effect in ferromagnetics II”. In: *Physica* 24.1-5 (Jan. 1958), pp. 39–51.

[34] L. Berger. “Side-Jump Mechanism for the Hall Effect of Ferromagnets”. In: *Phys. Rev. B* 2 (11 Dec. 1970), pp. 4559–4566.

[35] R. Mathieu et al. “Scaling of the Anomalous Hall Effect in SrRuO3”. In: *Phys. Rev. Lett.* 93 (1 June 2004), p. 016602.

[36] Noam Haham et al. “Scaling of the anomalous Hall effect in SrRuO3”. In: *Phys. Rev. B* 84 (17 Nov. 2011), p. 174439.

[37] Noam Haham, James W. Reiner, and Lior Klein. “Scaling of the paramagnetic anomalous Hall effect in SrRuO3”. In: *Phys. Rev. B* 86 (14 Oct. 2012), p. 144414.

[38] Yevgeny Kats et al. “Testing the Berry phase model for extraordinary Hall effect in SrRuO3”. In: *Phys. Rev. B* 70 (18 Nov. 2004), p. 180407.

[39] C. W. Jones et al. “The structure of $SrRuO$3 by time-of-flight neutron powder diffraction”. In: *Acta Crystallographica Section C* 45.3 (Mar. 1989), pp. 365–367.

[40] Kartik Samanta et al. “Tailoring the anomalous Hall effect of SrRuO3 thin films by strain: A first principles study”. In: *Journal of Applied Physics* 129.9 (Mar. 2021).

[41] Céline Lichtensteiger. “InteractiveXRDFit: a new tool to simulate and fit X-ray diffractograms of oxide thin films and heterostructures”. In: *Journal of Applied Crystallography* 51.6 (Oct. 2018), pp. 1745–1751.

[42] Romain Gaillac, Pluton Pullumbi, and François-Xavier Coudert. “ELATE: an open-source online application for analysis and visualization of elastic tensors”. In: *Journal of Physics: Condensed Matter* 28.27 (May 2016), p. 275201.

[43] Shinsuke Yamanaka et al. “Thermophysical properties of SrHfO3 and SrRuO3”. In: *Journal of Solid State Chemistry* 177.10 (Oct. 2004), pp. 3484–3489.

[44] Peipei Su et al. “Super-flexibility in Freestanding Single-Crystal SrRuO3 Conductive Oxide Membranes”. In: *ACS Applied Electronic Materials* 4.6 (June 2022), pp. 2987–2992.

[45] P. B. Allen et al. “Transport properties, thermodynamic properties, and electronic structure of SrRuO3”. In: *Physical Review B* 53.8 (Feb. 1996), pp. 4393–4398.

[46] Q. Gan et al. “Direct measurement of strain effects on magnetic and electrical properties of epitaxial SrRuO3 thin films”. In: *Applied Physics Letters* 72.8 (Feb. 1998), pp. 978–980.

[47] F. Le Marrec et al. “Magnetic behavior of epitaxial SrRuO3 thin films under pressure up to 23 GPa”. In: *Applied Physics Letters* 80.13 (Mar. 2002), pp. 2338–2340.

[48] R. Dirsyte et al. “Impact of epitaxial strain on the ferromagnetic transition temperature of SrRuO3 thin films”. In: *Thin Solid Films* 519.19 (July 2011), pp. 6264–6268.

[49] J.J. Neumeier, A.L. Cornelius, and J.S. Schilling. “Influence of pressure on the ferromagnetic transition temperature of SrRuO3”. In: *Physica B: Condensed Matter* 198.4 (May 1994), pp. 324–328.

[50] H. Boschker et al. “Ferromagnetism and Conductivity in Atomically Thin SrRuO3”. In: *Physical Review X* 9.1 (Feb. 2019).

[51] Huimin Jeong et al. “Thickness-dependent orbital hybridization in ultrathin SrRuO3 epitaxial films”. In: *Applied Physics Letters* 115.9 (Aug. 2019), p. 092906.

[52] D. J. Groenendijk et al. “Berry phase engineering at oxide interfaces”. In: *Physical Review Research* 2.2 (June 2020).

[53] Kota Terai, Tsuyoshi Ohnishi, Mikk Lippmaa, et al. “Magnetic properties of strain-controlled SrRuO3 thin films”. In: *Japanese journal of applied physics* 43.2A (2004), p. L227.

[54] A. T. Zayak et al. “Structural, electronic, and magnetic properties of SrRuO3 under epitaxial strain”. In: *Physical Review B* 74.9 (Sept. 2006).

[55] Martin Zahradník et al. “Magnetic domain wall motion in SrRuO3 thin films”. In: *Materials amp; Design* 187 (Feb. 2020), p. 108390.

[56] In: *Philosophical Transactions of the Royal Society of London. Series A, Mathematical and Physical Sciences* 240.826 (May 1948), pp. 599–642.

[57] Yevgeny Kats et al. “Large anisotropy in the paramagnetic susceptibility of SrRuO3”. In: *Physical Review B* 71.10 (Mar. 2005).

[58] L. Klein et al. “Extraordinary Hall effect in SrRuO3”. In: *Physica B: Condensed Matter* 281-282 (June 2000), pp. 608–609.

[59] Peng Li et al. “Evidence for topological type-II Weyl semimetal WTe2”. In: *Nature Communications* 8.1 (Dec. 2017).

[60] Su-Yang Xu et al. “Discovery of Lorentz-violating type II Weyl fermions in LaAlGe”. In: *Science Advances* 3.6 (June 2017).

[61] N P Ong and Sihang Liang. “Experimental signatures of the chiral anomaly in Dirac–Weyl semimetals”. en. In: *Nat. Rev. Phys.* 3.6 (May 2021), pp. 394–404.

[62] Kamal Das and Amit Agarwal. “Berry curvature induced thermopower in type-I and type-II Weyl semimetals”. en. In: *Phys. Rev. B.* 100.8 (Aug. 2019).

[63] Adolfo G Grushin et al. “Inhomogeneous Weyl and Dirac semimetals: Transport in axial magnetic fields and Fermi arc surface states from pseudo-landau levels”. In: *Phys. Rev. X.* 6.4 (Dec. 2016).

[64] Kamal Das and Amit Agarwal. “Linear magnetochiral transport in tilted type-I and type-II Weyl semimetals”. In: *Physical Review B* 99.8 (Feb. 2019).

[65] Yu. A. Boikov and V. A. Danilov. “Anisotropic magnetoresistance of partially relaxed SrRuO3 films”. In: *Physics of the Solid State* 53.6 (June 2011), pp. 1298–1301.

[66] R. Gunnarsson. “Anisotropic spin-orbit interaction revealed by in-plane magnetoresistance in single-oriented SrRuO3 thin films”. In: *Physical Review B* 85.23 (June 2012).

[67] Noam Haham et al. “Low-temperature anisotropic magnetoresistance and planar Hall effect in SrRuO3”. In: *Physical Review B* 87.14 (Apr. 2013).

[68] G Herranz et al. “Anisotropic magnetoresistance in SrRuO3 ferromagnetic oxide”. In: *Journal of Magnetism and Magnetic Materials* 272–276 (May 2004), pp. 517–518.

[69] “The electrical conductivity of transition metals”. In: *Proceedings of the Royal Society of London. Series A - Mathematical and Physical Sciences* 153.880 (Feb. 1936), pp. 699–717.

[70] “The resistance and thermoelectric properties of the transition metals”. In: *Proceedings of the Royal Society of London. Series A - Mathematical and Physical Sciences* 156.888 (Aug. 1936), pp. 368–382.

[71] A. Fert and I. A. Campbell. “Two-Current Conduction in Nickel”. In: *Physical Review Letters* 21.16 (Oct. 1968), pp. 1190–1192.

[72] J Smit. “Magnetoresistance of ferromagnetic metals and alloys at low temperatures”. In: *Physica* 17.6 (June 1951), pp. 612–627.

[73] A. S. Goossens, M. A. T. Leiviskä, and T. Banerjee. “Anisotropy and Current Control of Magnetization in SrRuO3/SrTiO3 Heterostructures for Spin-Memristors”. In: *Frontiers in Nanotechnology* 3 (May 2021).

[74] Fumiya Takata et al. “Negative anisotropic magnetoresistance resulting from minority spin transport in NixFe4xN (x=1 and 3) epitaxial films”. In: *Journal of Applied Physics* 121.2 (Jan. 2017).

[75] T. Ogasawara et al. “General Features of Photoinduced Spin Dynamics in Ferromagnetic and Ferrimagnetic Compounds”. In: *Physical Review Letters* 94.8 (Mar. 2005).

[76] B.L. Johnson and R.E. Camley. “The Effect of Spin Dependent Scattering from Impurities on Giant Magnetoresistance and Thermal Conductivity in Fe/Cr Multilayers”. In: *MRS Proceedings* 231 (1991).

[77] A. Vailionis. “The effects of strain on crystal structure and properties during epitaxial growth of oxides”. In: *Epitaxial Growth of Complex Metal Oxides*. Elsevier, 2015, pp. 175–207.

[78] P. Mondal and J. W. Jeffery. “The crystal structure of tricalcium aluminate, Ca3Al2O6”. In: *Acta Crystallographica Section B Structural Crystallography and Crystal Chemistry* 31.3 (Mar. 1975), pp. 689–697.

[79] Petr Ptáček, ed. *Strontium Aluminate - Cement Fundamentals, Manufacturing, Hydration, Setting Behaviour and Applications*. InTech, July 2014.

[80] Shuji Hasegawa. *Reflection High-Energy Electron Diffraction*. Oct. 2012.

[81] Augustinus J.H.M. Rijnders and David H.A. Blank. “Growth Kinetics During Pulsed Laser Deposition”. Undefined. In: *Pulsed Laser Deposition of Thin Films*. Ed. by R. Eason. United States: Wiley, 2006, pp. 177–190.

[82] “Lake Shore 7500/9500 Series Hall System User’s Manual: Appendix A - Hall Effect Measurements”. In: ().

[83] David C Look. “Electrical characterization of GaAs materials and devices”. In: (1989).

[84] Jan G. Gluschke et al. “Impact of invasive metal probes on Hall measurements in semiconductor nanostructures”. In: *Nanoscale* 12.39 (2020), pp. 20317–20325.

[85] D. J. Groenendijk et al. “Epitaxial growth and thermodynamic stability of SrIrO3/SrTiO3 heterostructures”. In: *Applied Physics Letters* 109.4 (July 2016).

[86] V.Ya Prinz et al. “Free-standing and overgrown InGaAs/GaAs nanotubes, nanohelices and their arrays”. In: *Physica E: Low-dimensional Systems and Nanostructures* 6.1–4 (Feb. 2000), pp. 828–831.

[87] A. B. Vorob’ev et al. “Giant asymmetry of the longitudinal magnetoresistance in high-mobility two-dimensional electron gas on a cylindrical surface”. In: *Physical Review B* 75.20 (May 2007).

[88] Marius Grundmann. “Nanoscroll formation from strained layer heterostructures”. In: *Applied Physics Letters* 83.12 (Sept. 2003), pp. 2444–2446.

[89] P. Cendula et al. “Bending and wrinkling as competing relaxation pathways for strained free-hanging films”. In: *Physical Review B* 79.8 (Feb. 2009).

[90] A B Vorob ev and V Ya Prinz. “Directional rolling of strained heterofilms”. In: *Semiconductor Science and Technology* 17.6 (May 2002), pp. 614–616.

[91] S Catalano et al. “Rare-earth nickelatesiR/iNiOsub3/sub: thin films and heterostructures”. In: *Reports on Progress in Physics* 81.4 (Feb. 2018), p. 046501.

[92] J. L. García-Muñoz, J. Rodríguez-Carvajal, and P. Lacorre. “Neutron-diffraction study of the magnetic ordering in the insulating regime of the perovskites RNiO3(R=Pr and Nd)”. In: *Physical Review B* 50.2 (July 1994), pp. 978–992.

[93] P. Lacorre et al. “Synthesis, crystal structure, and properties of metallic PrNiO3: Comparison with metallic NdNiO3 and semiconducting SmNiO3”. In: *Journal of Solid State Chemistry* 91.2 (Apr. 1991), pp. 225–237.

[94] J A Alonso et al. “Room-temperature monoclinic distortion due to charge disproportionation inRNiO3perovskites with small rare-earth cations(R=Ho,Y, Er, Tm, Yb, and Lu): A neutron diffraction study”. In: *Phys. Rev. B Condens. Matter* 61.3 (Jan. 2000), pp. 1756–1763.

[95] Hyowon Park, Andrew J. Millis, and Chris A. Marianetti. “Site-Selective Mott Transition in Rare-Earth-Element Nickelates”. In: *Physical Review Letters* 109.15 (Oct. 2012).

[96] Yi Lu et al. “Origins of bond and spin order in rare-earth nickelate bulk and heterostructures”. In: *Physical Review B* 95.19 (May 2017).

[97] J. Ruppen et al. “Impact of antiferromagnetism on the optical properties of rare-earth nickelates”. In: *Physical Review B* 96.4 (July 2017).

[98] J. Zaanen, G. A. Sawatzky, and J. W. Allen. “Band gaps and electronic structure of transition-metal compounds”. In: *Physical Review Letters* 55.4 (July 1985), pp. 418–421.

[99] S. R. Barman, A. Chainani, and D. D. Sarma. “Covalency-driven unusual metal-insulator transition in nickelates”. In: *Physical Review B* 49.12 (Mar. 1994), pp. 8475–8478.

[100] X Obradors et al. “Pressure dependence of the metal-insulator transition in the charge-transfer oxides RNiO3 (R=Pr,Nd,Nd0.7La0.3)”. en. In: *Phys. Rev. B Condens. Matter* 47.18 (May 1993), pp. 12353–12356.

[101] Michele Kotiuga et al. “Carrier localization in perovskite nickelates from oxygen vacancies”. In: *Proceedings of the National Academy of Sciences* 116.44 (Oct. 2019), pp. 21992–21997.

[102] Chao Yang et al. “Ruddlesden–Popper Faults in NdNiO3 Thin Films”. In: *Symmetry* 14.3 (Feb. 2022), p. 464.

[103] Jumi Bak et al. “Formation of Two-Dimensional Homologous Faults and Oxygen Electrocatalytic Activities in a Perovskite Nickelate”. In: *Nano Letters* 17.5 (Apr. 2017), pp. 3126–3132.

[104] Grace A. Pan et al. “Synthesis and electronic properties of $Nd_{n+1}Ni_nO_3n+1$ Ruddlesden-Popper nickelate thin films”. In: *Physical Review Materials* 6.5 (May 2022).

[105] Qikai Guo et al. “Tunable resistivity exponents in the metallic phase of epitaxial nickelates”. In: *Nature Communications* 11.1 (June 2020).

[106] H. Takagi et al. “Systematic evolution of temperature-dependent resistivity in La$_{2-x}Sr_xCuO_4$”. In: *Physical Review Letters* 69.20 (Nov. 1992), pp. 2975–2978.

[107] Qikai Guo and Beatriz Noheda. “From hidden metal-insulator transition to Planckian-like dissipation by tuning the oxygen content in a nickelate”. In: *npj Quantum Materials* 6.1 (Aug. 2021).

[108] J Blasco, M Castro, and J Garcia. “Structural, electronic, magnetic and calorimetric study of the metal-insulator transition in NdNiO3- delta”. In: *Journal of Physics: Condensed Matter* 6.30 (July 1994), pp. 5875–5889.

[109] Abhijit Kar Gupta and Asok K. Sen. “Nonlinear dc response in composites: A percolative study”. In: *Physical Review B* 57.6 (Feb. 1998), pp. 3375–3388.

[110] Raoul Scherwitzl et al. “Electric-field control of the metal-insulator transition in ultrathin NdNiO films”. en. In: *Adv. Mater.* 22.48 (Dec. 2010), pp. 5517–5520.

[111] Adam J. Hauser et al. “Temperature-dependence of the Hall coefficient of NdNiO3 thin films”. In: *Applied Physics Letters* 103.18 (Oct. 2013), p. 182105.

[112] Shashank Kumar Ojha et al. “Anomalous electron transport in epitaxial NdNiO3 films”. In: *Physical Review B* 99.23 (June 2019).

[113] R. S. Dhaka et al. “Tuning the metal-insulator transition in NdNiO3 heterostructures via Fermi surface instability and spin fluctuations”. In: *Physical Review B* 92.3 (July 2015).

[114] Scherwitzl, Raoul. “Metal-insulator transitions in nickelate heterostructures”. en. PhD thesis. 2012.

[115] Kavita Soni et al. “Switching of majority charge carriers by Zn doping in NdNiO3 thin films”. In: *Journal of Physics: Condensed Matter* 33.1 (Oct. 2020), p. 015602.

[116] Qi Song et al. “Antiferromagnetic metal phase in an electron-doped rare-earth nickelate”. In: *Nature Physics* 19.4 (Jan. 2023), pp. 522–528.

[117] Natalia Palina et al. “Investigation of the metal–insulator transition in NdNiO3 films by site-selective X-ray absorption spectroscopy”. In: *Nanoscale* 9.18 (2017), pp. 6094–6102.

[118] *Hall effect - Wikipedia — en.wikipedia.org*. `https://en.wikipedia.org/wiki/Hall_effect`.

[119] Jinfeng Zhang et al. “Super-tetragonal Sr4Al2O7 as a sacrificial layer for high-integrity freestanding oxide membranes”. In: *Science* 383.6681 (Jan. 2024), pp. 388–394.

[120] Toru Mitsunaga. “X-ray thin-film measurement techniques”. In: *Rigaku J* 25 (2009), pp. 7–12.

[121] Wenlai Lu et al. “Control of oxygen octahedral rotations and physical properties in SrRuO3 films”. In: *Physical Review B* 88.21 (Dec. 2013).

[122] David Pesquera et al. “Freestanding complex-oxide membranes”. In: *Journal of Physics: Condensed Matter* 34.38 (July 2022), p. 383001.

[123] Ji-Yeop Kim et al. “Reducing the oxygen vacancy concentration in SrTiO3- thin films via an optimized O2 plasma treatment for enhancing device properties”. In: *Applied Surface Science* 639 (Dec. 2023), p. 158271.

[124] Soo Young Kim et al. “Effect of N2, Ar, and O2 plasma treatments on surface properties of metals”. In: *Journal of Applied Physics* 103.7 (Apr. 2008).

[125] Ying Li et al. “Stacking and Twisting of Freestanding Complex Oxide Thin Films”. In: *Advanced Materials* 34.38 (Aug. 2022).

CURRICULUM VITÆ

Patrick BLAH

12-01-1994	Born in Teddington, United Kingdom.

EDUCATION

2006 - 2012	Secondary School St.Gerards Co.Wicklow
2012 - 2016	Undergraduate in Physics Trinity College Dublin, Co.Dublin, Ireland *Thesis: Synthesis and investigation of low dimensional carbon nanotube composite thermo-piezoelectric generators* *Supervisor*: prof. dr. D.Carroll
2017 - 2019	MSc. in Applied Physics University of Groningen, Groningen, The Netherlands *Thesis: Investigating Charge-to-Spin Conversion in TMD / Graphene Heterostructures* *Supervisor*: prof. dr. B.J.van Wees
2019 - 2024	PhD in Applied Physics Delft University of Technology, Delft, The Netherlands *Thesis: Freestanding complex-oxide membranes* *Supervisor*: prof. dr. A.D.Caviglia